

EXPLOSIVE SUBAQUEOUS ERUPTIONS: THE INFLUENCE OF VOLCANIC JETS
ON ERUPTION DYNAMICS AND TEPHRA DISPERSAL
IN UNDERWATER ERUPTIONS

by

RYAN CAIN CAHALAN

A DISSERTATION

Presented to the Department of Earth Sciences
and the Graduate School of the University of Oregon
in partial fulfillment of the requirements
for the degree of
Doctor of Philosophy

December 2020

DISSERTATION APPROVAL PAGE

Student: Ryan Cain Cahalan

Title: Explosive Subaqueous Eruptions: The Influence of Volcanic Jets on Eruption Dynamics and Tephra Dispersal in Underwater Eruptions

This dissertation has been accepted and approved in partial fulfillment of the requirements for the Doctor of Philosophy degree in the Department of Earth Sciences by:

Dr. Josef Dufek	Chairperson
Dr. Thomas Giachetti	Core Member
Dr. Paul Wallace	Core Member
Dr. Kelly Sutherland	Institutional Representative

and

Kate Mondloch	Interim Vice Provost and Dean of the Graduate School
---------------	--

Original approval signatures are on file with the University of Oregon Graduate School.

Degree awarded December 2020

© 2020 Ryan Cain Cahalan

DISSERTATION ABSTRACT

Ryan Cain Cahalan

Doctor of Philosophy

Department of Earth Sciences

December 2020

Title: Explosive Subaqueous Eruptions: The Influence of Volcanic Jets on Eruption Dynamics and Tephra Dispersal in Underwater Eruptions

Subaqueous eruptions are often overlooked in hazard considerations though they represent significant hazards to shipping, coastlines, and in some cases, aircraft. In explosive subaqueous eruptions, volcanic jets transport fragmented tephra and exsolved gases from the conduit into the water column. Upon eruption the volcanic jet mixes with seawater and rapidly cools. This mixing and associated heat transfer ultimately determines whether steam present in the jet will completely condense or rise to breach the sea surface and become a subaerial hazard. We develop a multiphase model with sub-grid calculations for *in situ* steam condensation to explore the relationship between eruption conditions (e.g. water depth, mass flux, eruption temperature) and the produced steam jet height and breach potential. We find that mass flux is the predominant control of jet height, more so than aspects of vent geometry.

After investigation of the controls of jet dynamics, we determine how jet dynamics affect mass transport and partitioning in the water column. Ultimately, this is the principle concern in studying eruptions, to determine when, where, why, and how tephra is deposited. We utilize the multiphase subaqueous eruption model to take the fundamental step in this investigation, to identify transport mechanisms that lead to

different mass partitioning outcomes. The results of this investigation show trends in mass partitioning associated with varying eruption parameters (eruption temperature and vent velocity) and particle parameters (size, density, concentration). We compare mass partitioning results for eruptions with and without gas jets to define features specific to explosive eruptions. Finally, we aggregate the model results and observations into eruption column transport regimes. This work represents the first look at many of these dynamic processes.

CURRICULUM VITAE

NAME OF AUTHOR: Ryan Cain Cahalan

GRADUATE AND UNDERGRADUATE SCHOOLS ATTENDED:

University of Oregon, Eugene
Georgia Institute of Technology, Atlanta, Georgia
University of Texas, Austin, Texas

DEGREES AWARDED:

Doctor of Philosophy, Earth Sciences, 2020, University of Oregon
Bachelor of Science, Geology, 2012, University of Texas

AREAS OF SPECIAL INTEREST:

Volcanology and Submarine Volcanology
Computational Modeling

PROFESSIONAL EXPERIENCE:

Research Assistant, Jackson School of Geosciences, University of Texas, Austin,
2010-2013

Teaching Assistant, Earth and Atmospheric Sciences, Georgia Institute of
Technology, Atlanta, 2014

Teaching Assistant, Department of Earth Sciences, University of Oregon, Eugene,
2018-2019

MESH research cruise to Havre Seamount, Kermadec Arc, NZ Co-PI: Dr. Bruce
Houghton, U. Hawaii; Dr. Rebecca Carey, UTAS, 2015

GRANTS, AWARDS, AND HONORS:

Graduate Research Fellowship, “*Experimentation and numerical modeling of
explosive subaqueous eruption dynamics*”, National Science Foundation, 2015

Graduate Student of the Month, School of Earth and Atmospheric Sciences,
Georgia Tech, 2014

Outstanding Student Paper Award, “*Coupled diffusion of lithium and yttrium (+HREE) in garnet*”, American Geophysical Union, 2012

Undergraduate Research Fellowship, “*Determination of lithium diffusion rates in garnet and coupled diffusion of lithium and yttrium in garnet*”, University of Texas at Austin, 2011

PUBLICATIONS:

Cahalan, R. C. & Dufek, J. (in Review) *Condensable gas jets in submarine eruptions: A multiphase model for hydrous phase change in explosive eruptions underwater*. Journal of Geophysical Research.

M. Manga, K. E. Fauria, C. Lin, S. J. Mitchell, M. Jones, C. Conway, W. Degruyter, B. Hosseini, R. Carey, R. Cahalan, B.F. Houghton, J.D.L. White, M. Jutzeler, S. A. Soule, and K. Tani (2018) *The pumice raft-forming 2012 Havre submarine eruption was effusive*. Earth and Planetary Science Letters. v. 489, p. 49-58. <https://doi.org/10.1016/j.epsl.2018.02.025>

R. Carey, S.A. Soule, M. Manga, J.D.L. White, J. McPhie, R. Wysoczanski, M. Jutzeler, K. Tani, D. Yoerger, D. Fornari, F. Caratori-Tontini, B. Houghton, S. Mitchell, F. Ikegami, C. Conway, A. Murch, K. Fauria, M. Jones, R. Cahalan, and W. McKenzie (2018). *The largest deep-ocean silicic volcanic eruption of the past century*. Science Advances v. 4 no. 1e1701121. doi: 10.1126/sciadv.1701121

R.C. Cahalan, E.D. Kelly, and W.D. Carlson (2014). *Rates of Li diffusion in garnet: Coupled transport of Li and Y+REEs*. American Mineralogist v. 99 no. 8-9 p.1676-1682. doi: 10.2138/am.2014.4676

ACKNOWLEDGMENTS

I would like to express my deepest gratitude to the various individuals whom have supported me throughout my graduate school experience. First, I would like to thank my advisor, Dr. Josef Dufek, for his mentorship and guidance, and most of all, for his unending optimism that has reinvigorated my drive at times where I felt entirely spent. I thank my dissertation committee members, Dr. Kelly Sutherland, Dr. Paul Wallace, and Dr. Thomas Giachetti, for their counsel that has helped steer my research, their encouraging words, and their time in reading and editing this document. I would also like to thank Dr. Rebecca Carey and the MESH research crew who invited me to participate in the research cruise to the Havre Seamount, which has been one of the most formative experiences in my graduate studies. My sincerest thanks to Dave and Fred for their continuing friendship, for the drafts they have read, and the late nights and chats that kept grad school fun and interesting.

Additionally, I would like to thank my family, Sean, Hunter, Mom, and Dad, for the endless support and love. To my parents, who gave me my curious nature and the freedom to pursue it. And to my brothers, who have encouraged me and been a deep well of creative inspiration and strength. To my dear friends Jani, Cameron, Matt, Luju, Jacob, and Eric, who have provided great debate, conversation, laughter, and inspiration that spans multiple decades and will hopefully continue for many more. Thank you to you all.

Lastly, to my beautiful and supportive wife, who has uprooted her life twice now and sacrificed much to allow me to pursue my career. Without you, there is little chance that I finish this degree and continue on. You are everything. I love you. Thank you.

I wish to express appreciation to The University of Texas, Georgia Institute of Technology, and The University of Oregon for financial support and opportunities which have allowed me to grow and freely conduct my research. Hook'em Horns! I would also like to thank the National Science Foundation Graduate Research Fellowship Program, which has funded me for a large portion of my graduate schooling and has provided me, and many others, with the academic freedom to explore interesting and new ideas.

TABLE OF CONTENTS

Chapter	Page
I. INTRODUCTION	1
Introduction to Subaqueous Eruptions.....	1
The Anatomy of an Explosive Subaqueous Eruption.....	4
Fragmentation	5
Eruption Jet	8
Hydrothermal Plume.....	12
Tephra Dispersal	13
Overview of Subaqueous Eruption Models	13
Multiphase Models.....	15
Objectives	16
II. EXPLOSIVE SUBMARINE ERUPTIONS: THE ROLE OF CONDENSABLE GAS JETS IN UNDERWATER VOLCANISM.....	19
Introduction.....	19
Observations and Evidence of Submarine Eruption Jets	20
Steam Condensation in Eruptions.....	22
Methods.....	24
The Subaqueous Eruption Model.....	24
Scaling.....	25
Conservation Equations	27
Hydrous Phases.....	29
Model Details.....	30

Chapter	Page
Validation Exercises.....	31
Plume Model.....	32
Direct Contact Condensation, DCC.....	33
Comparison to Observations at NW Rota 1.....	36
Results.....	39
Jet and Steam Heights	41
Ocean Surface Vertical Displacement.....	45
Sea Surface Temperature Anomaly.....	46
Particle Effects on Jet and Steam Heights.....	46
Discussion.....	50
Conclusion	56
III. PARTITIONING OF VOLCANIC TEPHRA DURING SUBAQUEOUS EXPLOSIVE ERUPTIONS.....	58
Introduction.....	58
Methods.....	67
Model: Gas Jet vs No Gas.....	67
Model: Particles and Eruption Parameters.....	69
Mass Partitioning Calculations	69
Breaching Mass Calculations.....	70
Results.....	71
Vent Velocity	74
Particle Concentration.....	75

Chapter	Page
Eruption Temperature	77
Particle Diameter	79
Solid Density.....	80
Comparing Partitioning in Explosive Jet Eruptions and Heat-Flux Equivalent Plumes	81
Discussion.....	82
Vent Velocity	83
Particle Concentration.....	83
Eruption Temperature	84
Particle Diameter	84
Solid Density.....	85
Dynamic Regimes Control Mass Partitioning	85
<i>Collapse: Fountaining</i>	86
<i>Collapse: Mid-Column</i>	87
<i>Partial Collapse: Unroll-Sheet</i>	88
<i>Partial Collapse: Rise and Settle</i>	88
<i>No Collapse: Surface Plume and Breach</i>	89
Regime Diagram	89
Conclusions.....	91
IV. CONCLUSIONS AND FUTURE DIRECTION.....	93
REFERENCES CITED.....	98

LIST OF FIGURES

Figure	Page
1. Schematic Diagram of a Subaqueous Explosive Eruption from White, Schipper, and Kano (2015).....	10
2. Example Eruption Simulations	30
3. Single Phase Model Validation.....	33
4. DCC Regime Map.....	35
5. DCC Morphological Jet Regimes	37
6. Comparison of Measured and Simulated Gas Jet at NW Rota 1.	39
7. Contour Plots of Mean and Maximum Steam Terminus and Steam Jets (1).....	42
8. Contour Plots of Mean and Maximum Steam Terminus and Steam Jets (2).....	43
9. Ocean Surface Displacement and Sea Surface Temperature Anomaly (SSTA)....	47
10. Particle Effects on Jet and Steam Height.....	48
11. Comparison of Jet and Steam Heights for Different Vent Diameters	49
12. Schematic Illustration of Submarine Explosive Eruptions	51
13. Regime Diagrams.....	52
14. Relationship Between Eruption Conditions and Steam Breach Percentage	54
15. Eruption Dynamics in Explosive Subaqueous Eruptions	63
16. Example Simulation with Partitioning Zones	67
17. Effects of Vent Velocity on Mass Partitioning.....	74
18. Effects of Particle Concentration on Mass Partitioning.....	76
19. Effects of Eruption Temperature on Mass Partitioning	78
20. Effects of Particle Diameter on Mass Partitioning	80

Figure	Page
21. Effects of Solid Density on Mass Partitioning.....	81
22. Eruption Column Transport Regimes	86
23. Regime Diagram	90

LIST OF TABLES

Table	Page
1. Symbols	26
2. Simulation Property Values	28
3. Simulation Parameter Ranges	38
4. Particle Parameter Sets	69
5. Simulation Parameters and Mass Partitioning Results	72

CHAPTER I

INTRODUCTION

Introduction to Subaqueous Eruptions

The majority of terrestrial volcanism occurs in the submarine environment at oceanic hot spots, subduction-related volcanic arcs, and mid-ocean ridges (Carey et al., 2018; Cas & Giordano, 2014; Head & Wilson, 2003; McBirney, 1963; White et al., 2003; White et al., 2015a; White, et al., 2015b; Wohletz et al., 2009). Though, due to difficulty of accessibility, submarine volcanism has received significantly less from the scientific community attention than the subaerial counterpart. The motivations for the study of submarine volcanology are similar to that of the subaerial counterpart (i.e. human and resource related hazards, natural resource production, scientific endeavors), though the principle properties that govern eruption dynamics are fundamentally different (Cas & Simmons, 2018). Submarine volcanoes can erupt to form lava flows and domes, eruption columns and pyroclastic jets, which can collapse to form water-supported (and maybe even gas-supported) density currents (Carey et al., 2018; Cas & Wright, 1991; Cas et al., 1990; Manga et al., 2018; White, 2000). Energetic or sufficiently shallow eruptions can breach the water surface and form subaerial volcanic plumes that pose threats to aviation (Cas & Simmons, 2018; Fiske et al., 1998; Koyaguchi & Woods, 1996; Thorarinnsson, 1965, 1968; Vaughan & Webley, 2010). Breaches can also transport expanding gases that generate violent basal surges and can endanger nearby shorelines or maritime vessels (Mastin & Witter, 2000; Mastin, 1995). Submarine volcanoes can generate tsunamis, both by explosive eruption and submarine landslides resulting from edifice failure (Dondin et al., 2012; Pérez-Torrado et al., 2006; Silver et al., 2009). Collapsing jets can

generate fast-travelling pyroclastic gravity currents that could damage underwater infrastructure (White, 2000). In addition to these hazards, submarine eruptions can have varied impacts on local and regional ecology, by local kill zones associated with violent eruption or acidification of seawater, or by nutrient seeding for chemosynthesis or other nutrient-limited processes (iron-fertilization) (Guieu et al., 2018; Hamme et al., 2010; Mélançon et al., 2014; Pham & Ito, 2018; Santana-Casiano et al., 2013). On a regional to global scale, submarine eruptions can generate extensive pumice rafts that can house and transport micro and macrofauna literally across the world. The floating homes can alter a species biological dispersion and have unknown effects on biodiversity where the raft pumice ultimately settles (Bryan et al., 2004, 2012; Jutzeler et al., 2020; Jutzeler et al., 2014a). While some of these impacts are not unique, others only occur in the submarine realm and require a greater understanding of subaqueous volcanism in order to predict or even anticipate their consequences. The present study focuses on the outcomes of explosive eruptions underwater.

Progress in the field of submarine explosive volcanism requires integrative study of eruption observations and measurements, modern seafloor and uplifted deposits, laboratory experiments, and numerical models. Each of these branches of study possesses limitations which can be leavened by the others. First, direct observations and measurements of underwater eruptions, though relatively few in number, have provided an abundance of insight into explosive eruption processes (Batiza et al., 1984; Cashman & Fiske, 1991; Chadwick et al., 2008; Deardorff et al., 2011a; Embley et al., 2014; Embley et al., 2014; Embley & Rubin, 2018; Resing et al., 2011; Schipper et al., 2010).

Studies of deposits in the rock record are invaluable and provide the majority of the context for the fundamental theories and physical models of submarine volcanology (Allen & McPhie, 2000; Allen et al., 2010; Allen & Freundt, 2006; Allen & McPhie, 2009; Busby, 2005; Cas & Giordano, 2014; Cas et al., 1990; Fiske et al., 2001; Fiske & Matsuda, 1964; Fiske, 1963; Jutzeler, McPhie, et al., 2014; Kokelaar & Durant, 1983; McPhie et al., 1990; Pontbriand et al., 2012; Stewart & McPhie, 2004; and many others). While extensive, yet noncomprehensive, work has been done on uplifted submarine volcanic deposits, a vast majority of existing seafloor deposits go unexplored. Field studies, though, are limited by their availability and accessibility, as well as the incompleteness of the story available. Many components of *in situ* dynamic processes are absent from the deposits, either never present or overprinted by later or destructive processes. Something as substantial as erupted volume can be misestimated by orders of magnitude due to far-field transport and deposition (Carey et al., 2018; Jutzeler et al., 2014). Reworking by animals (bioturbation) or reworking by wave or current activity can completely alter stratigraphy to an unrecognizable state (Allen & Freundt, 2006). Therefore, the goal of a comprehensive understanding of submarine eruptions cannot come from deposits alone. Analog experiments can add to our interpretive abilities by providing insight into controlled, micro- to lab-scale processes (Barreyre et al., 2011; Fauria et al., 2017; Fauria & Manga, 2018; Friedman et al., 2006; Moitra et al., 2020; Schipper et al., 2013; Sonder et al., 2011; Verolino et al., 2018; Wohletz et al., 2009; Zimanowski & Buttner, 2003). Studies like these excel in isolating components of processes to understand how they contribute to a larger integrative process (e.g. experiments of particle settling to understand deposit formation). Experiments also

provide excellent benchmarks for validation of numerical investigations. Though, experiments can be expensive, at times dangerous, and are limited by the necessary scale of certain processes. For example, it is impossible to capture eruption lengthscales and difficult to conduct experiments at the high pressures present in 500 m of water depth. While this may not be critical for some investigations, those considering Reynolds number or pressure related processes are limited. Numerical models provide opportunities to study processes at multiple scales, only limited by computational and numerical technology and resources. Models enable us to evaluate the extents of processes that cannot be studied via other means and can inform us on what to expect from an event that may happen or that has yet to be studied. A related example, explosive eruption jets are known to exist underwater, but their form, extent, and influence on an eruption is poorly understood. Studies of deposits have provided the fundamental understanding and hypotheses on the connection between eruption processes and products, and have been further advanced by experiments that have provided insight into fluid-melt processes (Kano et al., 1996; Verolino et al., 2018). But the form of the jet, its unsteady, property-dependent nature, and the role of different components within the jet dynamics, has largely been left to be determined by numerical investigation.

The Anatomy of an Explosive Subaqueous Eruption

In a fashion similar to subaerial eruptions, submarine eruptions involve magma that rises through country rock driven by a pressure gradient. This magma can lose or retain its gas (Manga et al., 2018), predominantly steam (gaseous H₂O or CO₂), as it erupts through the seafloor either via effusive flowing lavas, viscous domes and spines,

or explosive eruptions that produce highly turbulent, particle-laden gas jets that can collapse and feed fast moving, ground-hugging density currents (Carey et al., 2018; Fink & Anderson, 2000; Fornari, 1986; Kelley et al., 2002; Schmidt & Schminche, 2000; White et al., 2015). Contrarily, these phenomena are heavily modified by the increased ambient pressure, heat capacity, and viscosity and decreased expansivity of the underwater environment (Cas & Simmons, 2018). In the following section, I will examine components of subaqueous pyroclastic eruptions with a focus on the aspects of the underwater environment that fundamentally change how eruptions progress.

Fragmentation

Subaqueous explosive volcanism has multiple mechanisms for generation. In this study, I generally focus on explosive eruptions that are generated from pyroclastic disruption of a bubbly magma via overpressuring and shearing (Papale, 1999, 2001; Zhang, 1999). In this style of explosive eruption, the melt is fragmented into pyroclasts from fine ash (<0.063 mm) to block (>64 mm) size that are carried by an upwardly expanding and accelerating gas jet. This type of explosive eruption, driven by conduit level pyroclastic fragmentation, is limited by the viscosity of the melt (composition, crystallinity, and temperature) and the volume of gas available. After the initiation of eruption, which can be any number of mechanisms, an established pressure gradient drives the upward migration of magma into and out of the conduit. As this parcel of magma rises and depressurizes, the solubility of H₂O and CO₂ decreases creating a potential that drives the exsolution of volatiles from the melt and into a free fluid phase (Cas & Simmons, 2018; Liu et al., 2005; Wallace et al., 2015). The exsolution of these

supercritical fluids and gases reduces the density of the parcel of melt and leads it to accelerate further, which drives depressurization and reduces the gas and parcel density further. This feedback cycle leads to an extremely rapid acceleration of bubbly melt through the conduit. As the gas exsolves from the magma, the dehydrated magma increases in viscosity. The combination of rapid acceleration and a sufficiently high viscosity will lead to a critical shearing threshold past which the bubbly melt yields and violently disrupts into a gassy fragment mixture (Papale, 1999; Zhang, 1999). The gas accelerates until it reaches the choked flow threshold, at which point further acceleration is limited by conduit/vent geometry (Dobran, 1992; Mangan et al., 2004; Mastin, 2002).

The weight of the overlying water column has important effects on the processes above. The increased pressure at the vent (~ 1 MPa per 100 m of water), relative to a subaerial vent (~ 0.1 MPa), increases the total solubility of gas in the conduit (Cas & Simmons, 2018; Wallace et al., 2015). So, the residual dissolved volatiles in a melt at an underwater vent are going to be higher concentrations than a vent erupting into air. This reduction in exsolved fluids can limit the ability of the melt to cross the fragmentation threshold for three reasons. First, exsolution is delayed so that it occurs higher in the conduit than in the subaerial case, meaning the melt has less “time” to fragment before exiting the vent. Second, there is less total volume of fluid available to participate in the exsolution/acceleration/expansion feedback loop to reach the threshold. Third, the increased pressure and increased dissolved water both decrease the melt viscosity, which makes the shear threshold more difficult to reach (Cas & Simmons, 2018). These effects

are the reasoning behind the definition of a fragmentation water depth limit, below which fragmentation is no longer possible regardless of volatile content.

Another mechanism for generating subaqueous explosive eruptions is by the interaction of melt and water, called Fuel Coolant Interaction (FCI) (Dürig et al., 2020; Schipper et al., 2013; Wohletz, 2003; Zimanowski & Buttner, 2003). The water in FCIs can be confined below the surface, as in an aquifer or the groundwater, or free at the surface, like a lake or ocean. Upon the development of a propagating crack network in the melt or rock, either from vapor collapse or other means, the freshly exposed surfaces (increase in surface area) accelerate heat transfer and further FCI into a positive feedback loop. This rapid heat transfer into water can generate large and extremely violent steam explosions and is also known for generating abundant fine particles resulting from the repeated fracturing of the “fuel” or melt. The methods outlined in this study do not explicitly consider the dynamics of FCI type explosions as of yet, though the post-FCI processes of gas expansion, cooling, condensation, and collapse occur in very much the same way. In essence, the FCI could be considered the source of the steam explosion that feeds into our model.

While limitations to fragmentation prevent explosive (non-FCI) eruptions in the deep ocean, we know that explosive eruptions happen in shallow water (<200 m) and evidence for explosive eruptions in water depths as great as 900 m has been presented (Casas et al., 2018; Coombs et al., 2019; Rotella et al., 2015; Vaughan & Webley, 2010; White et al., 2015). Therefore, I move forward with the present study, understanding that

limits to explosive eruptivity exist, but that these bounds are to date not firmly established. Thus, in the present study I test eruption parameters and water depths inside and outside of those considered possible on earth to understand the limits of eruption jet as a volcanic phenom.

Eruption Jet

Fluid jets are phenomena encountered at various scales in nature when a fluid is projected through an opening into a medium. In volcano eruptions, turbulent jets are responsible for carrying magmatic material through an erupting vent and into the atmosphere or water column (Chojnicki et al., 2015; Kieffer & Sturtevant, 1984; Koyaguchi & Woods, 1996; Valentine & Wohletz, 1989; Verolino et al., 2018; Woods, 1988; Woods, 1995). These can range from jets of magma in magma fountains to supersonic, dusty gas jets in Plinian columns. Another example, albeit at a much smaller scale, is the tiny water jet released from a cephalopod that is responsible for its mobility in the ocean. In engineering, jets are utilized in a wide range of applications, both industrial and aesthetic, where fluid is forced through designed nozzles to achieve sub-, trans-, and super-sonic streams.

For this study we focus on jets of gas, both particle-laden and not, that erupt from a vent into the ambient fluid. In a subaerial volcano eruption, the erupting jet is injected into a fluid with density lower than the jet itself, called air. As the jet rises, shear at the walls of the jet drives inward mixing and entrainment of air. For the jet itself, this effect of mixing reduces the internal kinetic energy. Though, entrainment of air into the jet is

critical for the erupted material to continue rising. As the entrained air heats and expands, the bulk density of the plume decreases. In this process, the act of heating and expanding of air converts thermal energy stored in the jet materials into work via expansion and increases kinetic energy (Valentine, 1998). If the bulk density of the eruption column drops below that of the surrounding atmosphere, a volcanic plume will form and continue to rise buoyantly after the inertia from jet is dissipated.

This is somewhat different in water. As the accelerating gas is ejected from the vent, it can be initially buoyant or non-buoyant depending on the particle load it carries (Cas & Simmons, 2018). If the mixture is buoyant, the jet will be driven by both momentum and buoyancy. Mixing and entrainment of water cools the gas jet, heats the entrained water, and reduces the jet momentum via viscous dissipation (Chojnicki et al., 2015; Koyaguchi & Woods, 1996; List, 1982). If the amount of entrained water is less than a few weight percent, the water will boil, utilizing the conversion of thermal energy into work as the water expands into steam, and further accelerate the expanding jet (Koyaguchi & Woods, 1996). It is important to consider the relative amount of energy it takes to heat a mass of air to expand versus that needed to heat and then boil the equivalent mass of entrained water. In the atmosphere, unconfined air can freely expand as it receives thermal energy, whereas in a subaqueous eruption, the entrained water will expand only slightly as it heats until it reaches the boiling point. Energy is then consumed as latent energy in the phase change reaction. Therefore, above a few weight percent of entrained water, entrainment is not energetically beneficial and entrained water and interfacial water-jet interaction at the jet edges lead to the eventual complete

condensation of steam in the jet (Koyaguchi & Woods, 1996). If the initial mixture is not buoyant, it is extremely unlikely for the jet to become buoyant via entrainment as, like the buoyant case, cooling will drive condensation and further densify the mixture. Entrainment is critical to establishing buoyancy in the subaerial jet, but in submarine eruptions, entrainment of water retards buoyancy and slows the rise of the eruption column.

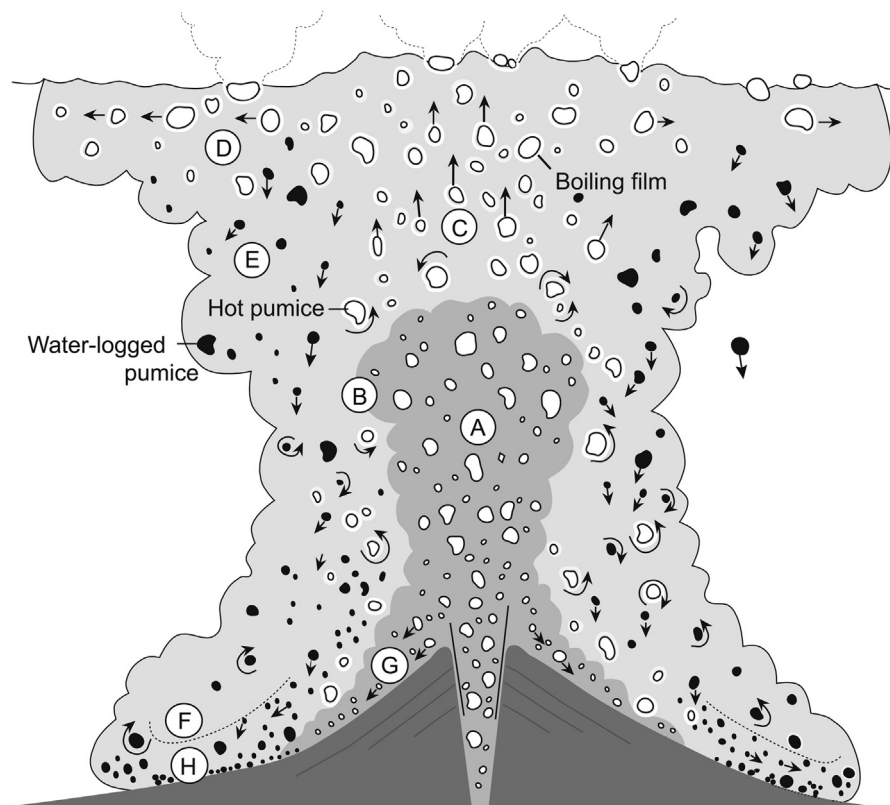


Figure 1. Schematic diagram of a subaqueous explosive eruption from White, Schipper, and Kano (2015). White clasts are gas-saturated, dark clasts are water-saturated. Region A represents the gas dominated jet. B is the jet-water mixing interface. C is the rising heated-water buoyant plume. D is the radially spreading surface plume. E is the collapsing region of the eruption column where water-logged clasts drive a downward current. F is the low concentration of a collapsing density current. G is the near-vent jet-fed gas-water supported density current. H is the pumice deposit.

The erupting volcanic jet ultimately meets one of two fates. The jet may penetrate with enough inertia to breach the water-air interface, or it will completely condense and either generate a plume, fully collapse, or some combination of the two. As the jet rises and loses energy, it will continuously detrain particles along the jet edges into the water column. Condensation of steam at the jet water interface can concentrate these particles along the jet edges. The particles may sink depending on their density and can drive downward coursing streams outside of the jet edges that feed density currents. These density currents can flow similarly to turbidity currents in sedimentology and travel fast and potentially far from the base of the volcano (White, 2000).

With enough energy, an explosive eruption can breach the air-water interface. Breaching events can be differentiated by a few different key characteristics. First is the frequency of breach. Does the breach only occur in minor, discrete pulses of gas penetrating the surface (e.g. 2011-2012 El Hierro, Carracedo et al., 2012)? Or is the breach steady, with near-constant and consistent arrival of steam at the surface (e.g. climactic Surtsey eruption, Thorarinsson, 1965, 1968)? The next important characteristic is the presence of a subaerial plume. Did the eruption yield a subaerial plume (2016-2017 Bogoslof, Coombs et al., 2019) or simply bursts of water-tephra mixture displaced through the surface (early Kavachi 2000 eruption, Baker et al., 2002)? Does the plume carry solid particles or is it mostly vapor? These different breaching behaviors can be directly linked to jet behavior at depth and can provide the opportunity to analyze near-vent eruption dynamics without directly observing the eruption at depth. While possible, this correlation has yet to be determined.

Hydrothermal Plume

At the point where the eruption column transitions from being inertia to buoyancy dominated (i.e. once the jet runs out of steam) the transport of volcanic materials (tephra and residual gas bubbles) will take place within a buoyant heated water plume. The hydrothermal plume can rise as long as its density is below that of the surrounding water, determined by the temperature and salinity of the water and the density and load of particles and bubbles (Turner, 1966). In a similar fashion to the jet, the plume may continue to entrain colder ambient water which will reduce its inertia, cool internal waters, and densify the plume. Additionally, as the plume cools and densifies, it may become unable to transport the particle load (Carey et al., 1988; Sparks et al., 1993). At this point the plume either sheds sufficient particle mass to maintain buoyancy or it will collapse downward to the point where it is neutrally buoyant. The particles will be continuously shed via plume wall shearing and clustering and continue to feed the density currents discussed in the section above. Particle coupling within the plume controls how it they will behave in relation to the flow behavior.

A plume that remains buoyant to the surface can possess enough momentum to vertically displace the sea surface interface, especially if it still bears gas. As the plume arrives within tens of meters of the surface, gases still entrained in the plume or trapped within particles will rapidly expand, accelerating the plume toward the surface. The plume will push upward, collapse back down, and begin to spread radially, driven by its

momentum (Garvine, 1984). As long as the newly developed outward momentum is sufficient, the plume can continue to spread.

Tephra Dispersal

Once volcanic tephra is partitioned between the sea surface, the seafloor, and different zones of the water column by one of the processes outlined in the section above (i.e. density currents, spreading sea surface plumes, subaerial plumes) local water currents may direct particle dispersal. The influence of currents on tephra dispersal depends on two major factors. First, ocean currents vary substantially in magnitude and direction with depth (Joseph, 2014). Particles that reach specific heights may be preferentially carried at that level if the current conditions are preferable for transport. Second, this process is heavily dependent on properties of the individual particles, especially density, size, and shape (Burgisser & Bergantz, 2002). Some particles may be too dense to be carried by a slow-moving current while others are easily lofted and transported for kilometers. Ocean current dispersal is therefore largely specific to the regional current profile and bathymetry, as well as the specific particle populations and their transport history. To predict particle dispersal and the associated impacts in the ocean, we need to quantify mass partitioning in the water column associated with different eruption sources and their transport various processes.

Overview of Submarine Eruption Models

Two numerical models of subaqueous explosive volcanic eruptions have provided some of the most important and foundational insights in this field. The first is the work of

Koyaguchi and Woods (1996) which carefully extends the moist eruption column model developed in Woods (1993) to the subaqueous eruption realm. In this one-dimensional model hydrous phase change in the eruption column is accounted for first thermodynamically, then kinetically. This is done by assuming a variable amount of water entrainment that is well mixed in the column, then thermodynamically heated and converted to steam, or the internal steam condenses. This contribution of steam and/or water is then accounted for in the eruption column model as a source of mass, volume, and thermal and kinetic energy. The second of these models was presented in Head and Wilson (2003) in which the authors utilize simple, yet robust numerical methods to ascertain some of the fundamental relationships in subaqueous eruptions. Relevant to the current study, Head and Wilson estimate the height of an explosive submarine jet by instituting a strong set of assumptions about mixing along the jet periphery. This enables the definition of a set geometric relationship between the vent width and the jet height. Both of these models rely on significant assumptions about mixing between the jet and surrounding water that ultimately decides the eruption column behavior. Additionally, these studies treat eruption columns as steady phenomena, which may work well in subaerial settings, but may not adequately capture the oscillatory nature of subaqueous jets. Further quantitative assessment of the role of fluid dynamics with regards to interaction between the eruption column and surrounding water is needed.

In addition to these explosive eruption models there are an abundance of oceanographic models that have been used to or are capable of modeling hydrothermal plumes and approach the phenomenon from an oceanographic perspective (Adcroft et al.,

2011; Chen et al., 2006; Luettich et al., 1992, and many others). These models are typically much coarser in resolution, significantly larger (10x-1000x), and focused on broader-scaled processes in oceanography. While these models are well suited for oceanographic studies, they do not capture the necessary particle-fluid and particle-particle interactions that are critical for assessment of volcanic eruption modeling. This type of treatment requires a modeling method that independently calculates the transport and interaction of various interpenetrating phases.

Multiphase Models

Multiphase models are those that treat the transport of different gas, liquid, and solid phases by their own set of continuum equations for momentum, mass, and energy conservation. The individual phases are able to occupy the same grid cells and are coupled to one another via gas/liquid-particle and particle-particle drag relationships. Through these relationships multiphase models are able to capture the nonlinear dynamics of turbulence, effects of solids concentration, and particle-particle interactions inside geologic flows (Burgisser & Bergantz, 2002; Dufek & Bergantz, 2007; Martin & Meiburg, 1994). Individual components of physics are agglomerated onto these first principle physical relations to better approximate specific fluid dynamic problems, such as phase change or other thermodynamic theory, kinetic theory, sub-grid turbulence models, etc. Particle-particle interaction is modeled utilizing approaches from theoretical molecular collisional dynamics (Dufek & Bergantz, 2007; Lun et al., 1984) augmented with a frictional component from kinetic and collisional stresses at high particle concentrations (Dufek & Bergantz, 2007; Savage, 1998; Syamlal et al., 1993). These

additional physical components allow for the analysis of multi-species fluid interactions, particle clustering and size-density sorting, internal shear and boundary shear stresses, and chemical reaction rates inside the flow.

These types of models are generally favored for the wide range of physical applications and the potential for detailed analysis of the interplay between micro-, meso- and macro-scale processes. When time and computational resources allow, multiphase continuum models can be used to solve highly complex and non-linear problems. The disadvantage to these multiphase models is they are often computationally intensive and run times can range from hours to weeks, and therefore are not currently suited for syn-eruption hazard analysis and prediction.

Objectives

Our current limited capability to observe and measure the dynamic processes that underpin subaqueous eruptions exposes the necessity for new subaqueous eruption models. The multi-continuum approach discussed above augmented robust hydrous phase physics and hybrid carrier fluid approach discussed in Chapter 2 can provide insight into subaqueous jet dynamics and particle dispersal.

The first objective of this study, introduced in Chapter 2, is to assess the role of subaqueous condensable gas jets on underwater eruptions and to ascertain the limitations of those jets. Water-steam interactions inside explosive eruption jets likely dictate the

dynamics and outcome of an eruption, yet unsteady jet dynamics incorporating hydrous phase change has yet to be evaluated.

Hypothesis: Initial eruption conditions have a strong control on condensable gas jet dynamics and the vertical extent of the jet in subaqueous volcanic eruptions.

Questions: What are the primary controls of volcanic jet heights in subaqueous eruptions? At what depth is steam breach and/or volcanic jet breach possible? Does the presence of solid particles significantly affect jet height and jet stability? Are there measurable quantities we can use to assess jet dynamics for no-breach eruptions?

Objectives: To further understand subaqueous explosive eruptions and the processes that they comprise, to identify eruption conditions that favor surface breaching eruptions, and to ascertain the water depth limits of eruption breaching.

The second objective, introduced in Chapter 3, is to evaluate mass partitioning in the ocean water column associated with explosive subaqueous volcanic eruptions. Current velocity is highly water-depth specific and can vary in both magnitude and direction substantially in the same ocean current profile. Since we are generally concerned with where volcanic material is transported in association with hazards and resources, it is important to understand what controls the initial distribution of mass in the water column before it can be dispersed by ocean currents.

Hypothesis: The presence and character of a volcanic jet in a subaqueous eruption primarily controls the partitioning of mass between the atmosphere, the ocean surface, the seafloor, and various levels in the water column.

Questions: Does having an explosive jet significantly alter the mass partitioning of different solid particle populations compared to an eruption without a gas jet? If so, can this difference be used to assist interpretation of existing deposits or surface observations/measurements where eruptions are not directly witnessed?

Objectives: To quantify mass partitioning in subaqueous eruptions associated with volcanic gas jets and no jet eruptions with varying particle properties. To use the mass partitioning information to define deposit patterns or attributes unique to specific eruption conditions to aid in analysis of eruption deposits.

The final chapter of this document (Chapter 4) is the summary of the findings of Chapters 2 and 3 as well as conclusive remarks on application, expansion, and further direction of this work.

CHAPTER II

EXPLOSIVE SUBMARINE ERUPTIONS: THE ROLE OF CONDENSABLE GAS JETS IN UNDERWATER VOLCANISM

[This chapter is intended to be published in the Journal of Geophysical Research: Solid Earth in a reformatted form and contains contributions from only the Doctoral student (RC) and his advisor (JD)]

Introduction

Both subaerial and submarine explosive volcanic eruptions have the capacity to produce high velocity gas jets where fragmented particle-gas mixtures are ejected with significant inertia inherited from conduit processes (e.g. Woods, 1995). In this jet-thrust region, the particle-laden gas rises and loses kinetic energy through drag, gravitational deceleration, and turbulent mixing with the ambient fluid. Subaerial jet-thrust dynamics have been extensively studied through remote observations, experiments, and numerical simulations (Andrews & Gardner, 2009; Bercovici & Michaut, 2010; Carey & Sparks, 1986; Costa et al., 2018; Di Muro et al., 2008; Gilbert & Sparks, 1998; Girault et al., 2014; Lube et al., 2004; Scase, 2009; Sparks, 1986; Suzuki & Koyaguchi, 2010; Trolese et al., 2019; Valentine, 1998; Wilson and Walker, 1987; Wilson, 1976; Woods, 1988; Woods, 1995). This work has expanded our understanding of momentum transfer in these jets and has described the link to conduit conditions, turbulent mixing, air entrainment, jet behavior, and subsequent plume morphology.

Both subaerial and submarine gas jets are driven by similar initial forces, yet the influence of the ambient fluid (air vs. water) yields significant differences in their manifestation (Cas & Simmons, 2018; Head & Wilson, 2003; Koyaguchi & Woods, 1996; White et al., 2015; Wohletz, 2003). Of course a prerequisite for explosive

submarine eruptions is that sufficient gases can exsolve at the inherently greater pressures of the submarine environment to initiate fragmentation. Once the explosive eruption is initiated, subaerial jets are emitted primarily as negatively buoyant gas-particle mixtures that collapse without requisite air entrainment. Conversely, submarine jets are often initially buoyant, and substantial mixing with water promotes cooling, condensation of volcanically derived water vapor, and requires higher velocities to prevent column collapse. However, at low volumes of mixed water (<10-15 wt%, Koyaguchi & Woods, 1996), seawater boiling leads to decreases in bulk jet density and enhances jet stability. The foundational work on submarine jet-thrust dynamics was developed using subaerial eruption models applied to the submarine environment, and leverages necessary assumptions about seawater mixing and entrainment dynamics and the requirement of thermodynamic equilibrium (Head & Wilson, 2003; Koyaguchi & Woods, 1996). Yet the role of phase change and steam dynamics in submarine jets has remained mostly unexplored, as has the role of condensable jet dynamics on tephra emplacement and dispersal in the water column.

Observations and Evidence of Submarine Eruption Jets

The study of submarine jet-thrust dynamics has been intensely hampered by a lack of in situ observations and measurements of eruption processes. A few sparse, but invaluable, observations have provided the opportunities to study these dynamics directly. Shallow-water surface-breaching and near breach eruptions at volcanoes like Surtsey, Bogoslof, Hunga Tonga-Hunga Ha'apai, South Sarigan, Teishi Knoll, and others have shown that eruptions in water less than 200 m deep can produce surface breaching

eruptions and may exhibit oscillatory pulsation at the vent driven by magma-water and steam-water interaction (Colombier et al., 2018; Coombs et al., 2019; Embley et al., 2014; Green et al., 2013; Koyaguchi & Woods, 1996; Lyons et al., 2019; Thorarinsson, 1965, 1968; Vaughan & Webley, 2010; Yamamoto et al., 1991). The study of shallow submarine eruptions also demonstrates that hydrous phase change and melt-water interaction is likely a first order control of eruption column height and tephra dispersal, and largely dictates what is measured by hydroacoustic and infrasound equipment.

Significantly fewer observations exist of eruptions in deeper water environments. NW Rota 1 (517 m), West Mata (1208 m), and Loihi Seamount (975 m) have been observed exhibiting explosive eruptions ranging from basaltic to andesitic melt compositions (Chadwick et al., 2008; Iezzi et al., 2020; Resing et al., 2011; Schipper et al., 2010). These eruptions were largely effusive with discrete explosions or short explosive phases. At the relatively low gas eruption rates exhibited in these cases, explosive behavior is limited, and the role of erupted steam is only transiently significant as discrete blasts quickly cool and collapse within meters over the vent. Above this, heated water plumes with secondary non-condensable gas phases (CO₂ and H₂S) control the buoyant rise of the lofted volcanic material (Chadwick et al., 2008; Deardorff et al., 2011b). While this type of eruption is likely more common than the submarine Plinian-equivalent, these deep explosive eruptions grant us a valuable, albeit narrow view of the likely range of explosive jet behaviors underwater.

Evidence can also be gathered from eruptions where no direct observations were made. This evidence can take the form of sea surface temperature (SST) anomalies, pumice rafts, water surface displacement, and water discoloration, as seen at the eruptions Havre 2012, the recent Tonga eruption 2019, El Hierro 2011-2012, and Serreta 1998-2001 (Carey et al., 2018; Carracedo et al., 2012; Casas et al., 2018; Jutzeler et al., 2014, 2020; Kueppers et al., 2012; Martí et al., 2013). These surface measurements may provide important information about the eruption below (e.g. vent flux, eruption temperature, particle concentration) but we must first ascertain the relationships between eruption conditions and the surface manifestations to make these measurables into valuable tools.

Steam Condensation in Eruptions

As erupted steam cools below the saturation temperature, defined as the point at which the fluid pressure is equal to ambient pressure, steam condenses to liquid water. At standard temperature and pressure (STP at 25 °C, 101325 Pa) the gas-to-liquid transition of water is accompanied by a 1000x reduction in volume. Therefore, when rapid condensation occurs along the jet-water interface, it yields steep, localized pressure gradients that are promptly relaxed. The oscillation amplitude and frequency of these interfacial pressure waves primarily control hydrodynamic instabilities, mixing, and entrainment at the jet interface (Chun et al., 1996; Khan et al., 2014; Zhao & Hibiki, 2018). Small scale gas jets in engineering applications have provided some guidance on these dynamics (refs). At low mass flux and/or high water temperature, pressure oscillation amplitude is high, oscillation frequency is low resulting in wavering and

collapsing, unstable jets. High mass flux with low water temperature produces small oscillation amplitude and high frequency, resulting in “quiet” stable jets (Chun et al., 1996; Khan et al., 2014; Zhao & Hibiki, 2018). We expect similar phenomena to control jet behavior in explosive eruptions, though we anticipate added instability from temporal variations in source conditions (e.g. pulsing behavior, particle clustering).

This study assesses the role of condensable steam in submarine explosive eruptions by quantifying the relationship between gas mass flux, eruption temperature, and the vertical extent of steam in the eruption column. To do this we present a multi-continuum model for the gas, water and particle phases that utilizes an established finite volume method augmented to suit submarine eruption conditions. We provide validation for the model by reproducing a set of hydrothermal plume heights, direct contact condensation (DCC) experimental jet morphologies, and measurements from footage of the NW Rota 1 eruption. Model results are then presented for simulations across a range of parameters applicable to explosive submarine volcanic systems. We focus on jet and steam terminus height as the most significant metrics for comparison. These heights represent morphological changes related to pressure oscillations and jet stability and are simple to compare across many simulations and parameter sets. We also evaluate the relationship between eruption jets, SSTA, and sea surface displacement. These two measurements can be directly related to eruptions that are otherwise unobserved and may provide insight into what is occurring at the source. Lastly, we introduce particle-laden jets to decipher the influence of solid phases on jet morphology and highlight the importance of further work in this direction.

Methods

A multiphase finite-volume model is constructed to determine the limits of gas jet stability and jet surface-breaching potential in submarine eruptions. The submarine gas jet model centers around the addition of two components to an existing multiphase approach. Firstly, we have incorporated a fluid phase tracking approach that accounts for immiscible carrier phases, steam and liquid water. Secondly, we have added the capability of time-dependent hydrous phase change. These two components working in concert requires the addition of updated equations of state and a pressure-dependent saturation temperature calculation.

The Subaqueous Eruption Model

Submarine eruptions generate complex mixtures of gas, particles, and liquid where each phase can move relative to the other phases and particles can be embedded in both gas and water flows. Fully resolving all aspects of the physics and scales in this problem is not currently computationally tractable. Instead, here we focus on the multiphase aspect of this problem, with special attention to the thermodynamics/phase change aspects of the condensable gas. Multiphase finite-volume methods generally utilize a single carrier phase comprising one or multiple species (i.e. H₂O and CO₂ gas) that transport other interpenetrating continua phases through drag relationships. In order to have two separate carrier fluids that can both transport particle phases, we have modified a 2-D multi-continuum (Eulerian-Eulerian) approach adapted from the MFI model (Multiphase Flow with Interphase eXchange, Syamlal et al., 1993) where the carrier fluids are treated as individual components of a single Eulerian phase with

constitutive equations and properties dictated by the thermodynamic state in the local grid cell. While this accurately accounts for the latent/sensible heat balance and mass exchange between the steam and water phases, the approach does not predict subgrid interfaces and surface tension effects at the smallest scales of flow.

Scaling

To consider the impact of surface tension on these problems, we utilize the Weber (W_e), Reynolds (R_e), and Ohnesorge (O_h) dimensionless numbers to evaluate the relative importance of physical forces in our system. The Weber number, defined as the ratio of kinetic energy to surface energy, is often used to assess the importance of inertia relative to surface tension in fluid jets (Table 1 contains symbol definitions):

$$W_e = \frac{\rho u^2 l}{\sigma} \quad (1)$$

When $W_e > 100$, turbulence rather than surface tension becomes the key determinant of jet behavior. Therefore, it becomes more useful to use the Reynolds number, ratio of inertial to viscous forces, to characterize the dynamics in terms of turbulence:

$$R_e = \frac{\rho u l}{\mu} \quad (2)$$

The Ohnesorge number can be used in conjunction with the Reynolds number to define the dominant mechanism for droplet formation or jet break up, and is defined as:

$$O_h = \frac{\mu}{\sqrt{\rho\sigma l}} \quad (3)$$

As O_h and R_e decreases, surface tension forces become more significant and inertial forces less so. For all conditions pertinent to the present study (Table 2), $We \gg 100$ and $R_e > 3e5$ such that we presently neglect the role of surface tension, even at low values ($O_h < 1e-3$). Gas jet dynamics are inertia dominated and not significantly affected by surface tension, and volcanic jets, experimental and natural, will likely break-up due to a critical Reynolds number phenomena (Namiki & Manga, 2008).

Table 1. Symbols

Value	Symbol
Temperature	T
Heat capacity	c_p
Interphase momentum transfer	I
Pressure	P
Heat flux	q
Gravity constant	g
Mean interphase heat transfer	\bar{H}
Velocity	u
Hydrous fluid drag	F_h
Particle-particle drag	F_p
Density	ρ
Volume fraction	α
Stress Tensor	τ
Kronecker delta	δ_{ij}
Latent heat	L
Reaction Rate	\dot{M}
Characteristic length	l
Viscosity	μ
Surface tension	σ
Diameter	D
<u>Subscripts</u>	
Hydrous fluid phase	h
Solid particle phase	p
Liquid Water	w
Steam	s
Hydrous phase change	H

Conservation Equations

In addition to the gas-liquid phase, individual volcanic particle phases are treated with their own conservation equations and are drag coupled to other fluid phases, similar to other multiphase modeling approaches of granular volcanic currents (Benage et al., 2014; Breard et al., 2018; Clarke et al., 2002; Darteville et al., 2004; Dufek et al., 2007; Dufek & Bergantz, 2007; Dufek et al., 2009; Dufek & Bergantz, 2007; Neri et al., 2003; Valentine & Wohletz, 1989). The general form of the conservation equations for the multiphase model can be written as follows (Table 1 contains symbol definitions):

$$\frac{\partial}{\partial t}(\alpha_n \rho_n) + \frac{\partial}{\partial x_i}(\alpha_n \rho_n u_{n,i}) = 0 \quad (4)$$

$$\frac{\partial}{\partial t}(\alpha_p \rho_p) + \frac{\partial}{\partial x_i}(\alpha_p \rho_p u_{p,i}) = 0 \quad (5)$$

$$\frac{\partial}{\partial t}(\alpha_n \rho_n c_{P,h} T_h) + u_{n,i} \frac{\partial}{\partial x_i}(\alpha_n \rho_n c_{P,h} T_h) = \frac{\partial q_h}{\partial x_i} - \overline{H_{np}} + \frac{L_H * \dot{M}_H}{l^3} \quad (6)$$

$$\frac{\partial}{\partial t}(\alpha_p \rho_p c_{P,p} T_p) + u_{p,i} \frac{\partial}{\partial x_i}(\alpha_p \rho_p c_{P,p} T_p) = \frac{\partial q_p}{\partial x_i} + \overline{H_{np}} \quad (7)$$

$$\begin{aligned} \frac{\partial}{\partial t}(\alpha_n \rho_n u_{n,i}) + \frac{\partial}{\partial x_i}(\alpha_n \rho_n u_{n,i} u_{n,j}) \\ = \frac{\partial P_n}{\partial x_i} \delta_{ij} + \frac{\partial \tau_{n,ij}}{\partial x_j} + I_i + \alpha_n \rho_n g_i \delta_{i2} \end{aligned} \quad (8)$$

$$\begin{aligned} \frac{\partial}{\partial t}(\alpha_p \rho_p u_{p,i}) + \frac{\partial}{\partial x_i}(\alpha_p \rho_p u_{p,i} u_{p,j}) \\ = \frac{\partial P_p}{\partial x_i} \delta_{ij} + \frac{\partial \tau_{p,ij}}{\partial x_j} - I_i + \alpha_p \rho_p g_i \delta_{i2} \end{aligned} \quad (9)$$

The additional term on the right-hand-side (rhs) of the hydrous fluid energy equation (eqn. 6) accounts for latent heat associated with phase change. The sign of the reaction rate can be either positive or negative depending on the direction of the hydrous phase reaction. All other physical changes due to condensation are within a single phase and thus momentum and mass are conserved throughout the reaction.

Table 2. Simulation Property Values

Property Name	Lab Scale	Volcanic Scale
Steam Density (kg/m ³)	1	10
Water Density (kg/m ³)	1000	1000
Water-steam ST (0.1-0.7)	0.7	0.7
Steam Viscosity (Pa s)	1.00E-05	1.00E-05
Water Viscosity (Pa s)	1.00E-03	1.00E-03
Vent Velocity (m/s)	100	100
Particle Diameter (m)	1.00E-04	1.00E-04
Vent Diameter (m)	0.02	10
Column Height (m)	1	500
Reynolds Number, Re Gas	2.0E+05	1.0E+09
Reynolds Number, Re Water	2.0E+06	1.0E+09
Weber Number, We	2.9E+02	1.4E+06
Ohnesorge Number, Oh	8.5E-03	1.2E-04

Hydrous Phases

Hydrous phase change is computed as a subgrid model by evaluating the local thermal conditions relative to saturation and employing a reaction rate to approximate that sensible/latent heat balance at equilibrium:

$$\dot{M}_H = \frac{m_g c_{p,h} (T_{sat} - T_h)}{L_H dt} \quad (10)$$

Condensation will initiate if the local temperature of a steam-bearing cell drops below the saturation temperature. At any timestep, if phase change occurs in a cell but does not go to completion, the local steam temperature is buffered by the reaction. If the condensation rate leads to a reacted mass in excess of the steam budget in a given cell, then the reaction goes to completion and excess heat loss is contributed to sensible heat. The saturation temperature of water, 100 °C at STP, is highly pressure dependent; to account for this, an empirical relationship between pressure and saturation temperature is implemented within the model (Osborne & Meyers, 1934). An example for reference, steam at the hydrostatic pressure equivalent of 1 km of water (~ 9.91 MPa) has a saturation temperature at 310.3 °C.

An individual equation of state (EOS) is used for liquid and vapor water; we treat steam as an ideal gas and liquid water with an EOS developed for seawater that accounts for pressure, temperature, and salinity (Nayar et al., 2016; Sharqawy et al., 2010). We find the ideal gas treatment of steam to be sufficient by comparing potential inaccuracies

(maximum $\pm 0.1 \text{ kg/m}^3$) to the density contrast with liquid water ($\sim 100\text{-}1000\times$). This contrast drives dynamic potentials and is sufficiently large to warrant the disregard of any ideal gas inaccuracies. Isobaric specific heat capacities are calculated for each hydrous phase based on empirical data from steam tables (“Steam tables,” 1934).

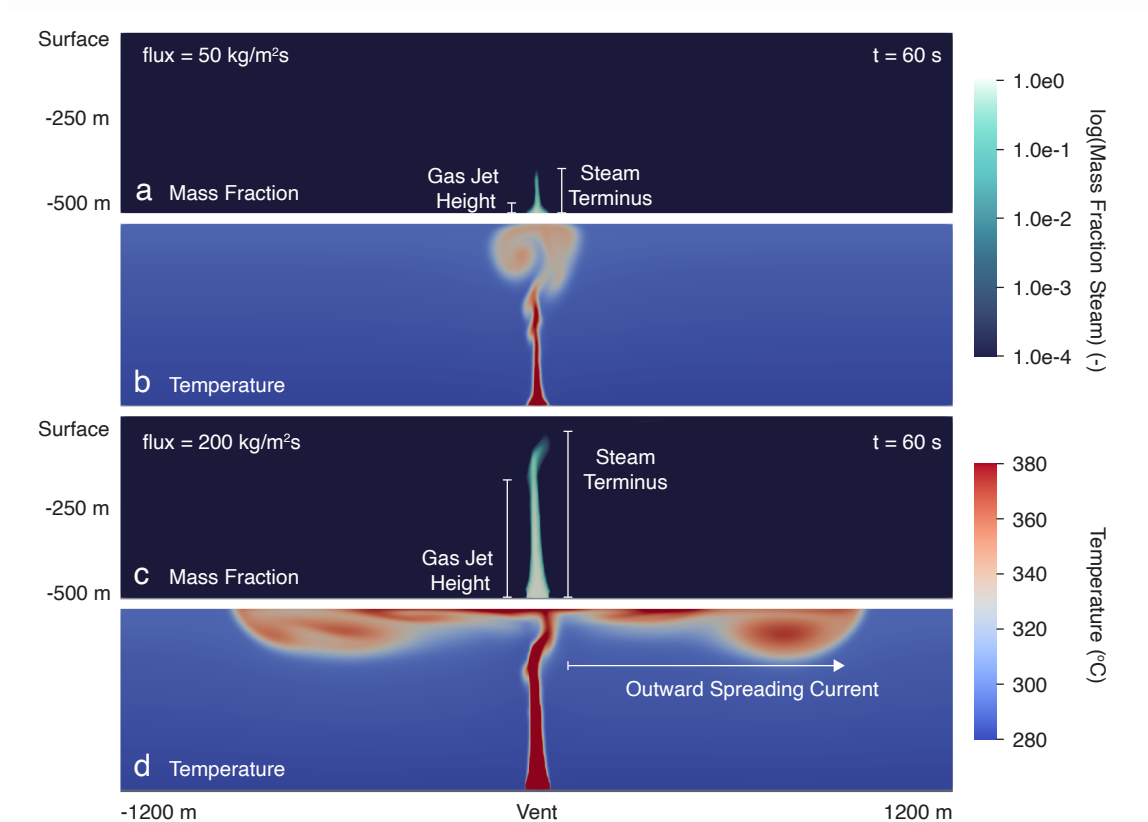


Figure 2. Example eruption simulations at different steam mass fluxes, at $50 \text{ kg/m}^2\text{s}$ (a,b) and $200 \text{ kg/m}^2\text{s}$ (c,d) showing log steam mass fraction distribution (a,c) and fluid temperature (b,d) at 60 s after initiation. Both have eruption temperatures of $1000 \text{ }^\circ\text{C}$ in 500 m water depth and a 60 m vent diameter. Gas jet heights and steam terminus heights (shown) are tracked throughout each simulation for comparison.

Model Details

The subaqueous eruption model is run in a 200 m to $1000 \text{ m} \times 6000 \text{ m}$ domain at uniform $5 \text{ m} \times 5 \text{ m}$ grid resolution and a 60 m vent diameter (with the exception of the

validation exercises). Figure 2 is an example visualization of two simulations at 500 m water depth and 1000 °C eruption temperature, showing steam mass fraction in log scale and fluid temperature for eruptive fluxes of 50 and 200 kg/m²s.

All simulations are initially vertically-stratified in salinity, temperature, and density corresponding to a spatially averaged region in the Kermadec arc, South Pacific (Sun et al., 2010). This location was selected due to the prevalence of underwater explosive eruptions in the Kermadec arc and is otherwise arbitrary. The sides of the domain have cyclic boundary conditions. The domain bottom has a no-slip condition, with the exception of the vent which is a mass inflow condition.

The top of the domain contains two 1000 m wide pressure outflow boundaries adjacent to each wall and set to 101325 Pa, and a free slip condition located at the central 4000 m. We utilize this upper boundary condition for multiple reasons. First, the free slip boundary allows spreading at the surface (for example from gravity currents) mimicking the water surface free-surface where an outflow condition would not. Second, the outflow conditions at the edges prevent high-pressure singularities (numerical effects) from a fixed volume domain.

Validation Exercises

A lack of direct observations and measurements prevent direct validation of the model against to-scale natural subaqueous, condensable, dusty, gas jets. In order to

maximize the validity of the simulation, components of the model have been robustly and quantitatively compared to data sets where available.

Plume Model

The most fundamental test of the model evaluates the single-phase dynamics and equation of state via comparison to a hydrothermal plume. This simulation includes all of the fundamental physics of the model outlined above, without the complexity associated with the immiscible phase and phase change. Most importantly, data sets of both measured natural systems and numerical simulations of hydrothermal plume transport exist for comparison. Carazzo et al. (2008) compare a new model developed for estimating plume transport to the TAG hydrothermal field (named from the Trans-Atlantic Geotraverse project that originally discovered the system) data set and model of Rudnicki & Elderfield (1992). Carazzo et al. estimated lower neutral buoyancy heights than the earlier model, citing a more sophisticated treatment of entrainment as the cause for differing results. The model presented in this study is compared to the results of these two models, along with the TAG data set, with the same conditions modeled in the TAG studies. Figure 3 includes an example plume simulation from this study, as well as a plot modified from figure 14 of Carazzo et al. (2008) that compares the measured and anticipated plume heights at TAG to the model presented in this study. Our model follows a similar trend falling closely to the curve estimated by Rudnicki & Elderfield (1992). Examples of these model runs are presented in supplementary material. While the aim of the present study is not to reproduce earlier hydrothermal studies, this result does illustrate that the seawater EOS, single-phase conservation equations, and initial/boundary conditions produces results consistent with the earlier studies.

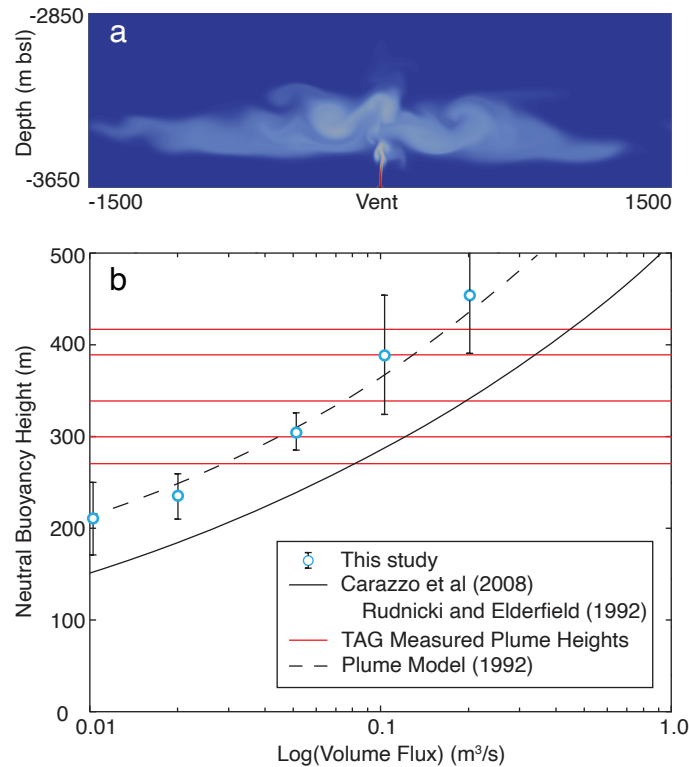


Figure 3. Single phase model validation exercise showing hydrothermal plume simulation of a TAG hydrothermal field heated water plume. (a) Simulation of TAG hydrothermal plume from which neutral buoyancy heights are picked using the distribution of a passive tracer in water column. Warm colors show high tracer values. (b) Present study data plotted over a modified version of Figure 14 from Carrazzo et al. (2008). Red solid lines show measured plume heights of unknown volume flux from the TAG field measure by Rudnicki and Elderfield (1992). Blue circles (this study) represent average neutral buoyancy heights for simulations of corresponding volume flux with bars showing standard deviation of picked heights. Solid and dashed black curves show model results from Carrazzo et al. (2008) and Rudnicki and Elderfield (1992), respectively.

Direct Contact Condensation, DCC

There is an absence of volcanological data with which to compare the modeled condensation dynamics. The most appropriate comparison available is to experimental data in the engineering field of direct contact condensation (DCC) (Aya & Nariai, 1991; Chun et al., 1996; Hong et al., 2012; Mazed et al., 2018; Meng et al., 2019; Xu et al., 2018; Zhao & Hibiki, 2018). Direct contact heat transfer focuses on the condition when

two fluids, typically immiscible, exchange heat directly rather than through a wall or boundary (Zhao & Hibiki, 2018). Examples include the situation where one fluid is introduced into another of contrasting temperature. DCC specifically refers to the case in which one of those fluids is condensable, such as steam, and is injected into a subcooled pool. Generally, DCC experiments are conducted in reinforced tanks decimeters to meters in height and width with gas injections occurring from a 1-20 mm nozzle oriented either parallel or perpendicular to the vertical axis of the tank. The gas injections are typically at near/supersonic velocities. DCC is of interest in various engineering applications including steam injection pumps, nuclear reactor flooding, condensate production, etc. (Zhao & Hibiki, 2018). The key variables are vapor mass flux and the temperature disparity between the injected steam and the subcooled water pool. As the flux of vapor into the pool decreases, the injection undergoes a series of morphological changes that exemplify specific dynamic regimes. Figure 4 is a diagram illustrating the extent of four regimes as well as the inter-regime transition zones (as defined by Chun et al., (1996)). The low-flux endmember, chugging (C), is defined as the regime where the gas-liquid interface exists at or below the nozzle opening, oscillating back and forth, with minimal breaching into the pool. Moving in the direction of increasing flux, the next regime is hemispherical bubble oscillation (HBO). This is characterized by the gas-liquid interface expanding beyond the nozzle into a hemispherical bubble before collapsing back down to vent height. Further increasing flux yields transition into the condensation oscillation regime (CO) where the gas injection is consistently above the nozzle, but the gas-liquid interface oscillates up and down, and periodically releases bubbles that grow voluminous enough to buoyantly rise before collapse. Beyond this is the endmember

regime, stable condensation (SC), where a steady and continuous jet hosts a stabilized gas-liquid interface, growing in height with further increase of vapor flux or pool temperature (Chun et al., 1996). A description and visual representation of each regime is provided (Figure 5).

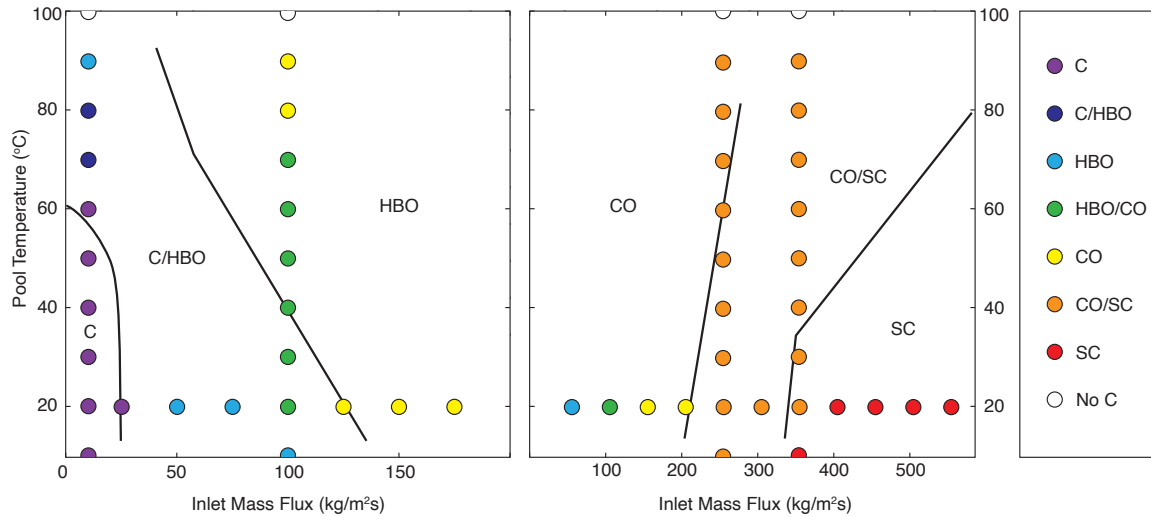


Figure 4. DCC regime map modified from Fig. 3 in Zhao and Hibiki (2018). Black curves separate jet morphology regimes aggregated in Zhao and Hibiki (2018). Regime abbreviations: C = chugging, HBO = hemispherical bubble oscillation, CO = condensation oscillation, SC = stable condensation, NC = no condensation. Transition zones (eg. C/HBO) are defined based on the variability in interfaces across studies and conditions aggregated in the review by Zhao and Hibiki (2018). Data from this study are plotted as filled circles with color corresponding to the regime identified in the simulation.

Zhao & Hibiki (2018) present a collective regime diagram over a wide range of experimental conditions. Figure 4 is a reproduction of this diagram overlain with the data from the present study, highlighting each regime as well as the transitional boundary zones between regimes. Note the broad transition zone between the HBO and CO zones. The transition between these regimes can be subtle, and given the subjective nature of regime identification, it is inherently difficult to decipher the cutoff between one regime

and another. This is also reflected in the data presented from the current model in which the area of transition is broad. Each filled circle represents an individual simulation which was run, processed, and assigned a regime. While this practice is qualitative and subjective by nature, we defined specific guidelines for regime selection and processed all simulations before plotting in order to limit bias. Additionally, all simulations that did not meet all criteria of a regime were assigned to a transitional regime. We find good agreement between the experimental regimes and the model results in both variable steam flux and pool temperature dimensions. Simulation videos are provided in supplementary materials.

In reproducing the relationship between mass flux, pool temperature, and morphological regime, we show that the thermodynamic and kinetic treatment of phase change is adequate at the scales and pressure-temperature ranges of DCC experiments.

Comparison to Observations at NW Rota 1

The DCC and plume validation examples validate individual components of the model; the final validation step is to compare the full model against a submarine volcanic eruption. NW Rota 1 is an active submarine volcano in the Mariana Arc with a summit 517 m below the surface that has had intermittent activity since at least 2005, when the activity was first observed. In the detailed analysis of the April 2006 eruption, Chadwick et al. (2008) characterized the activity to be Strombolian-like, evolving from effusive to explosive. Deardorff et al. (2011) later characterized the eruption into bins of early and late stage eruptive activity.

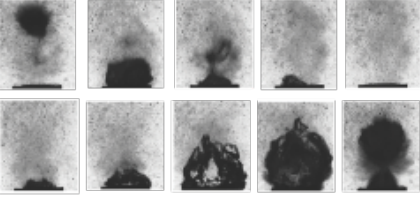
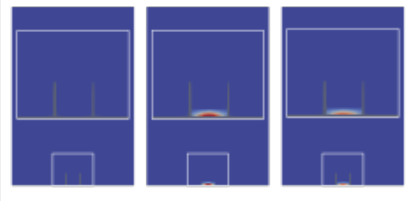
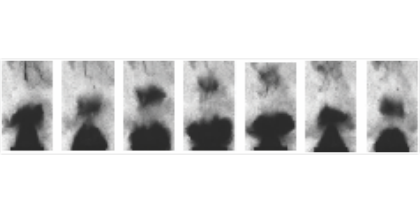
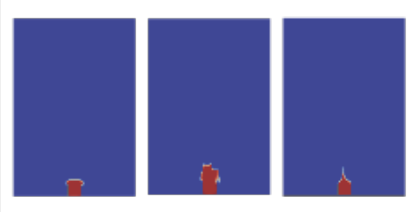
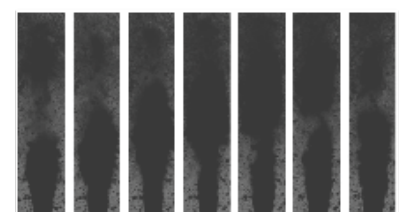
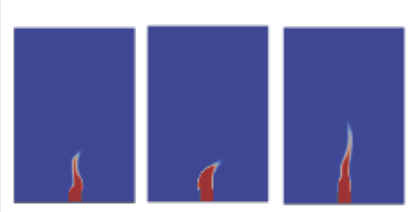
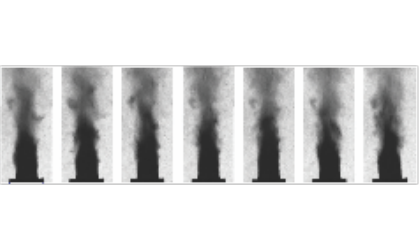
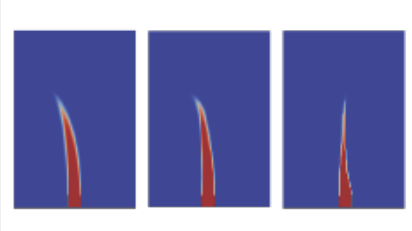
DCC Morphological Regime Comparison	Jet regimes modified from Q. Xu et al. (2018) Figure 3	Jet regimes modeled in this study
<p>Chugging</p> <p>Pulsating behavior at vent or in nozzle. Infrequently clears nozzle opening</p>		
<p>Hemispherical Bubble Oscillation</p> <p>Oscillating behavior immediately above nozzle. Forms vent-wide hemispherical bubble before fully collapsing. Infrequent disconnect.</p>		
<p>Condensation Oscillation</p> <p>Oscillating behavior forming an unsteady jet. Frequently disconnects, waggles, and partially to fully collapses</p>		
<p>Stable Condensation</p> <p>Steady, stable jet behavior. Infrequent disconnection or collapse. Morphology dependent on flux and pressure conditions. Varies between pointed/rounded/flared cones</p>		

Figure 5. DCC morphological jet regimes description, experimental depiction (Fig. 3 from Q. Xu et al. (2018)), and numerical depiction (present study). Simulation dimensions are 0.4 m by 0.6 m, vent diameter is 0.02 m. White outline in chugging simulations are expansions of the near vent region.

The early stage was characterized by discrete blasts within which they were able to estimate velocity profiles and condensation heights. The later stage was a more continuous eruption phase, yet the conditions favored intra-vent condensation, and is therefore less interesting for application of this model. We use the information extracted by Deardorff et al. (2011) from the early eruption phases to validate our simulation (Figures 6a, 6b). Figure 6b shows the relationship between height and time, and velocity and height that Deardorff et al. extracted from the NW Rota 1 recordings. They found that a rapid reduction in velocity from >3 m/s to ~ 0.5 m/s at 0.5-1 m above the vent marked the transition from momentum- to buoyancy-driven rise, and that this marked the completion of steam condensation in the column. We sought to reproduce this phenomenon in our model using the same conditions listed in Deardorff et al. (2011) (listed in Table 3). Our model accurately reproduces a condensation height at between 0.5-1 m with a corresponding reduction in velocity from >3 m/s to between 0.5 and 1 m/s marking the momentum-buoyant transition (Figure 6c).

Table 3: Simulation Parameter Ranges

	Set 1: Plume (8 sims)	Set 2: DCC (50 sims)	Set 3: NW Rota 1 (1 sim)	Set 4: Contour Diagrams (159 sims)	Set 5: Particles (31 sims)
Vent Diameter (m)	100	0.02	0.8	60	60
Domain Dims. (m)	6000 x 3000	0.3 x 0.6	10 x 10	6000 x 200, 500, 1000	6000 x 500
Grid Res. (m)	10 x 10	0.01 x 0.01	0.01 x 0.01	5 x 5	5 x 5
L-scale (-)	10	0.01	0.01	5	5
Mass Flux (kg/m ² s)	1e-3 - 7e-2	10 - 550	40	50 - 3000	300 - 2000
Inlet Temp. (K)	633	283 - 372	980	873 - 1673	873 - 1673
Inlet Salinity (0/00)	34.923	0	34.9	34.9	34.9

While it is impossible at this time to compare the full-scale simulations to large underwater eruptions directly, the piecewise components exhibit strong agreement with available data. Data gathered from future subaqueous eruptions will tremendously inform this and subsequent models.

Results

We present a set of eruption simulations with the aim of determining the connection between eruption conditions and jet behavior in submarine eruptions. To aid in model comparison we establish four threshold heights for the jet in the water column. The first two are the simulation mean and maximum

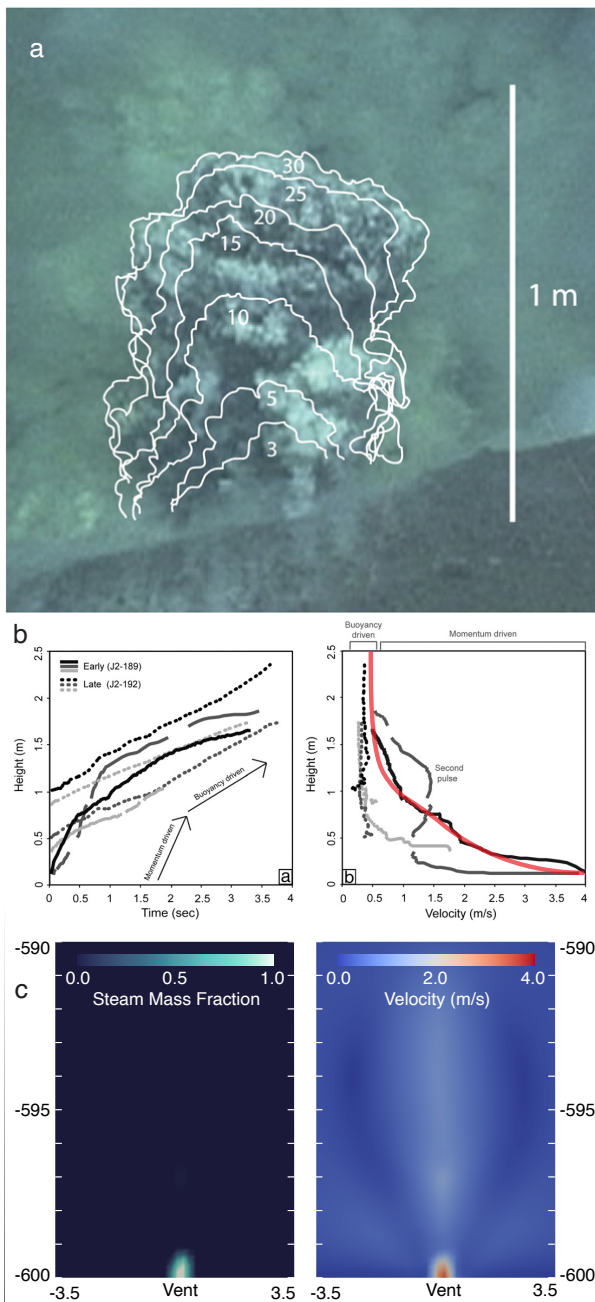


Figure 6. Comparison of measured and simulated gas jet at NW Rota 1. (a) still of gas jet in NW Rota 1 eruption with contours representing eruption front at time (s) from start of explosion from Deardorff et al. (2011); (b) Deardorff et al. (2011) utilized relationship of eruption height and velocity to determine the height the eruption jet where steam is completely condensed and velocity decreases sharply. (c) Simulation of this event showing steam mass fraction and velocity magnitude. The steam jet has condensed by ~ 1.1 m above vent where we also see a reduction in velocity from ~ 3 m/s to >1 m/s, similar to the measurements from Deardorff et al. (2011).

values of peak jet height, defined as the highest point from the vent where the gas jet is fully intact and mixing with water is minimal (<1 vol% liquid water). The other two metrics are the simulation mean and maximum values of the steam terminus height. The steam terminus defines the highest point that steam exists in the domain (>1 vol% steam). We report both the mean and maximum values as these transient simulations have unsteady and oscillatory behavior. When a steam breach occurs the steam terminus is shown as the sea surface, otherwise it will denote the highest point condensation occurs at a specific timestep. We focus the presented data around the parameters we have determined to be the most critical to jet behavior: mass flux, eruption temperature, water depth, and to a lesser degree vent geometry. Table 3 displays the simulation parameter value ranges for all data in the study. We present the simulations in two sets. The first were run for 100 s of simulated time to balance the need for many runs and the efficiency of flux-temperature-height map production. Additionally, 100 s is adequate time for the simulation to establish a steady or oscillatory jet after any initial pulsing activity has waned. Upon completion of the first set and the accompanying flux-temperature-height maps, we targeted parameter sets that would represent specific points in flux-temperature space. This second set of simulations are longer (600 s) and included broader data output for analysis, including sea surface temperature anomaly (SSTA) analysis, particle loading effects, and sea surface deflection heights. The time of 600 s is chosen to allow for the eruption to proceed long enough to reach the surface, horizontally spread or mix, up to the point where side boundary effects become an issue at which point that portion of the simulation is disregarded.

Jet and Steam Heights

By plotting the jet and steam terminus heights for the first simulation set, we are able to establish a series of flux-temperature-height maps (Figures 7 and 8) that show the vertical extent of submarine gas jets for eruptions at 200 m, 500 m, and 1000 m water depths. These can be read by considering each point as an eruption with a mass flux and eruption temperature corresponding to the X-Y coordinates. The contour values represent the max and mean height of the gas jet and steam terminus above the erupting vent, whereas the colors of the contours represent depth below the water surface which may help in comparison between water depths. All parameter value sets to the right of (greater than) the contour are conditions that will result in jet/steam heights that meet or exceed that contour value. We consider the maximum as it represents the limits of each as a hazard in the eruption, while the mean represents a more time-averaged view of the eruption period as a whole. To illustrate an example of when these two would differ, if an eruption produced only one pulse where the jet was able to breach the surface from 500 m depth while the remainder of the simulation time the jet was stable at 100 m over the vent, this might have a max jet height of 500 m though a mean height nearer to 100 m. Otherwise, if the jet was less stable and the height oscillated between the surface and 100 m regularly, then the max would remain at 500 m, though the mean will be around 300 m. In this way, the relationship between these two metrics can provide insight into the jet dynamics and stability. Upon evaluating the flux-temperature-height maps (Figures 7,8) it is apparent and unsurprising that increases in mass flux and eruption temperature result in increases in jet and steam terminus heights, mass flux being the more significant factor.

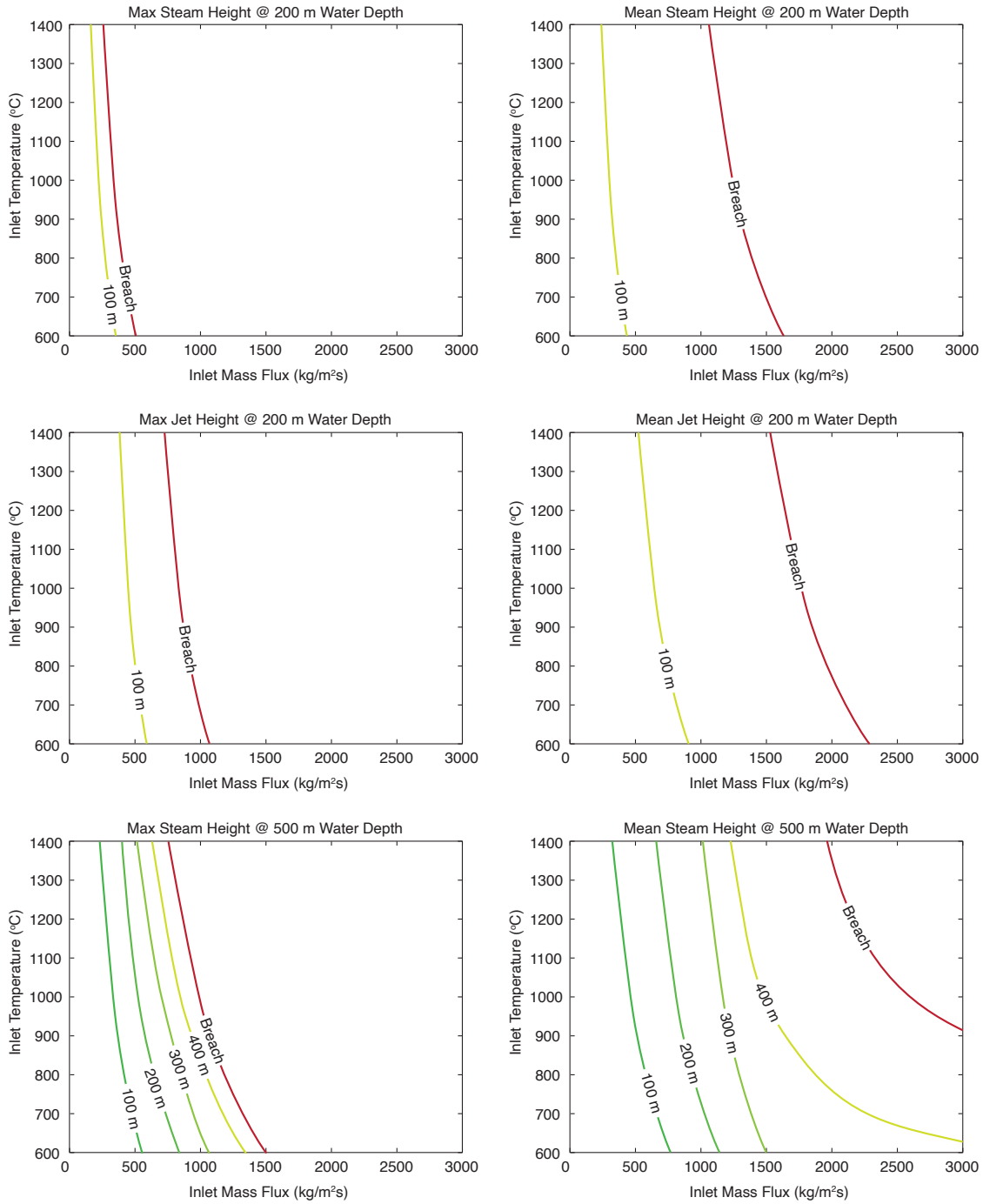


Figure 7. Contour plots of mean and maximum heights for steam terminus and steam jets across all simulated inlet temperature-mass flux space at water depths of 200 m, 500 m, and 1000 m. Contour values represent the height above the vent, while contour colors represent water depth. The surface breach contour is denoted in red. Space to the left of a contour represents eruption conditions which would produce a mean/max jet/steam terminus of at least that contour height.

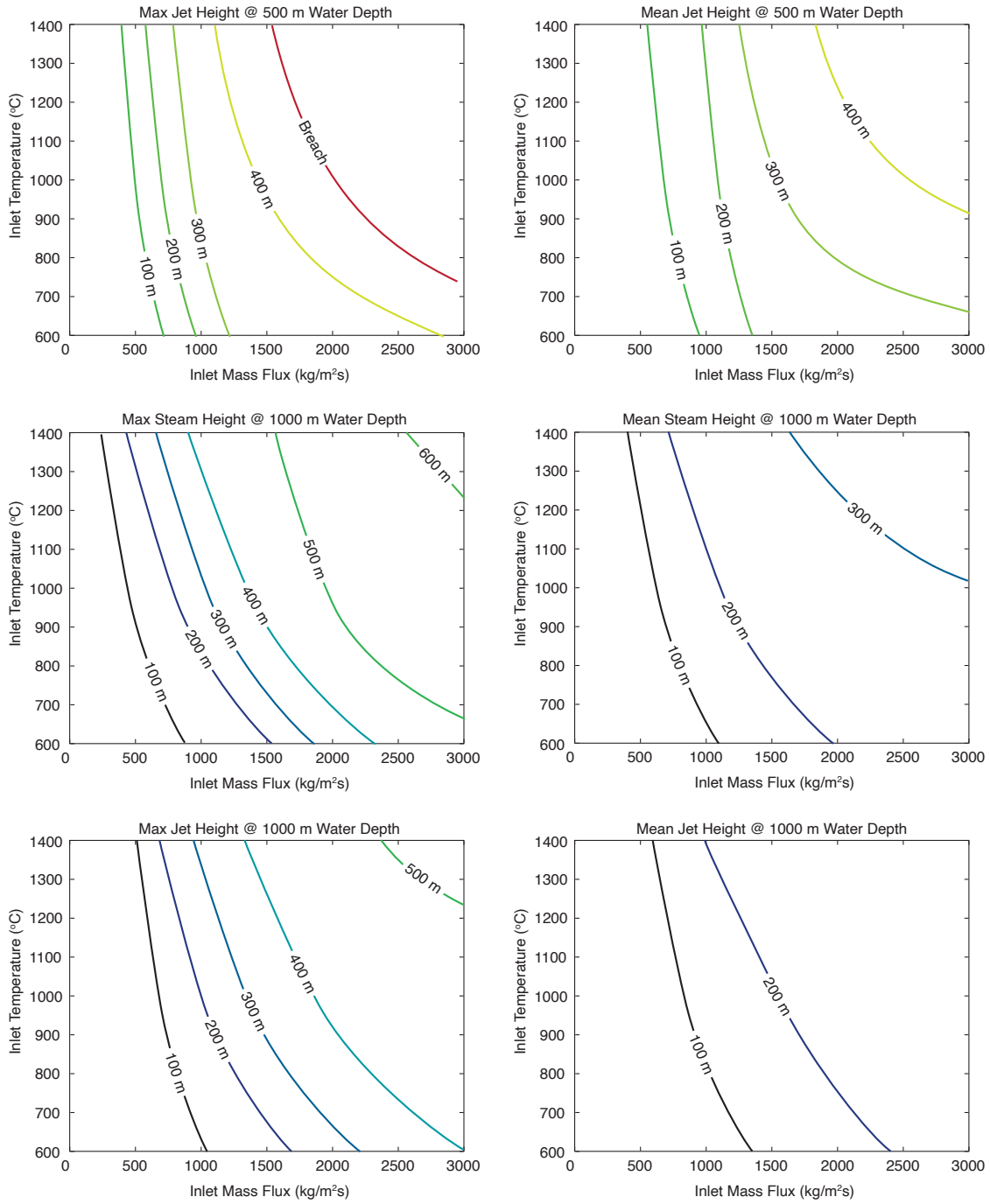


Figure 8. Contour Plots of Mean and Maximum Steam Terminus and Steam Jets

The more shallowly sloping contours of the deep-water simulations indicate an increasing dependence on eruption temperature with depth. Jet/steam heights appear to be more sensitive to changes in eruption temperature at cooler temperatures that approach the saturation point. This is clear in the lack of curvature in the contours of the shallow eruption case.

Jet/steam breach is shown by the red contour line and the region to the right of this represents conditions which favor eruption breaching the water surface. Breaching is likely the most extreme hazard of submarine eruptions, especially for those near/above the erupting vent. We show that for parameter combinations tested in the study, none produced jet or steam breaches from 1000 m water depth. At 500 m depth, we see common max steam breaches, max jet and mean steam breaches in only the hottest and highest flux cases, and no cases of mean jet breach. At 200 m water depth, most cases yield max steam and jet breaches, and many cases yield mean steam and jet breaches.

Contour spacing is significantly broader for mean values than for maximum values of both jet and steam terminus heights for all diagram pairs. Therefore, the mean values have a greater sensitivity to changes in the parameter than do the maximum values. This shows changes in the stability of the jet as you move through parameter space. While the maximum height may change slightly, the shift from single upward pulses to jet oscillations to stabilized jets will heavily affect the mean height calculated.

The flux-temperature-height maps (Figures 7,8) allow us to delineate the regions of different dynamic activity and enables us to choose a subset of simulations to run for longer and analyze in greater detail. We have chosen to run simulations at 1273 K, at each water depth (200 m, 500 m, 1000 m), and a range of mass fluxes. With the results of these simulations, we proceeded to evaluate two additional aspects of the simulations: sea surface temperature anomaly (SSTA) and water surface displacement heights.

Ocean Surface Vertical Displacement

As a proxy for ocean surface displacement, we made the simplification that for each grid cell along a 100 m line 30 m below the surface, at peak displacement all kinetic energy would be converted to potential energy. By ignoring other factors such as viscous dissipation and mass loss from horizontal flow, one can calculate a simple displacement height above the background ocean surface (these should be considered maxima, and we emphasize that these are all computed in a 2D geometry which will also enhance the height of these features). These values are then spatially averaged across the 100 m line, temporally averaged across the simulation, and displayed in Figure 9. At lower flux, displacements are highest for the 200 m water depth, though above 1500 kg/m²s the 500 m water depth simulations yield consistently larger displacements. This is due to the increased amount of steam present at the 30 m depth line, which reduces the total mass at that point, thereby reducing the kinetic energy available to be converted to displacement height.

Sea Surface Temperature Anomaly (SSTA)

SSTA was calculated at each timestep by averaging the fluid temperature across a centrally positioned 500 m long line at 10 m below the sea surface, then subtracting from this the time zero temperature across this line. When plotted with respect to time, each simulation showed two striking features. First, all simulations produced positive anomalies after enough time, though a few produced a short-lived dip in negative thermal anomaly displaced, initially deep and cool water. Second, anomalies are not steady and often mimic the jet dynamics, sometimes oscillating between warm and cooler temperatures producing radially migrating rings. When plotted as temporally averaged values (Figure 9) we see that SSTA varies significantly with water depth and mass flux and ranges from <1 degree to boiling temperatures when breaches occur. We also note that while signals from 200 m and 500 m water depth were consistently close, those from 1000 m were consistently muted.

Particle Effects on Jet and Steam Height

The final set of simulations were made to evaluate the effects solid particles have on jet development. All simulations to this point have been conducted without any solid phase. Due to the fact that most explosive eruptions contain some solid particle fraction, it is important to understand how they contribute to jet stability and heat transfer.

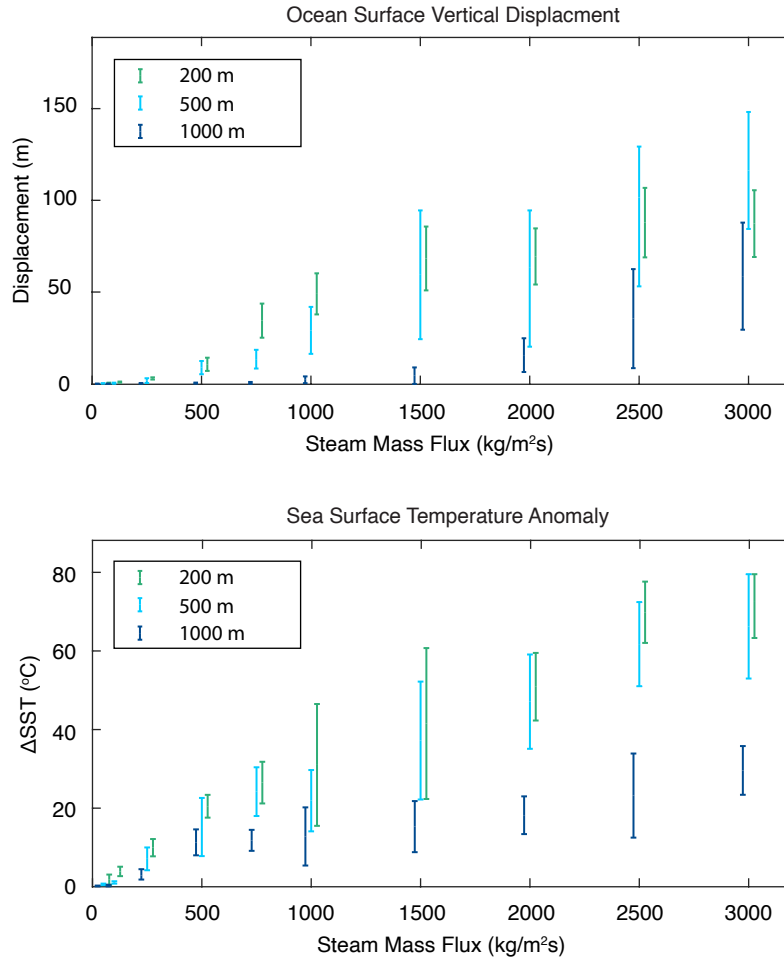


Figure 9. Time averaged ocean surface displacement and sea surface temperature anomaly (SSTA) shown for range of vent flux at 200 m, 500 m, and 1000 m water depths. Bars represent standard deviation of values with the average at center. Note: 200 m and 1000 m data are offset slightly from center to aid visibility.

We systematically varied parameters to determine the effect of different particle sizes and eruption conditions on jet and steam heights. We have evaluated the effects of particle size, density, and volume fraction, as well as eruption temperature and mass flux, at a water depth of 500 m. Figure 10 shows the results of these simulations and includes simulations with no particles for comparison. The addition of particles clearly has a stabilizing effect on eruption columns across all concentrations explored, including 1e-4, 1e-3, and 1e-2 solid volume fractions. We can see that increasing particle concentration

and eruption temperature consistently increase both jet and steam heights. For comparison of vent mass flux, we have included the equivalent no-particle simulation results. At lower flux (below 500 kg/m²s) all height metrics increase, though the max steam height is the most substantially effected. Above 500 kg/m²s, the addition of particles has an opposite effect, reducing both mean steam and mean jet heights, while increasing max jet and maintaining max steam.

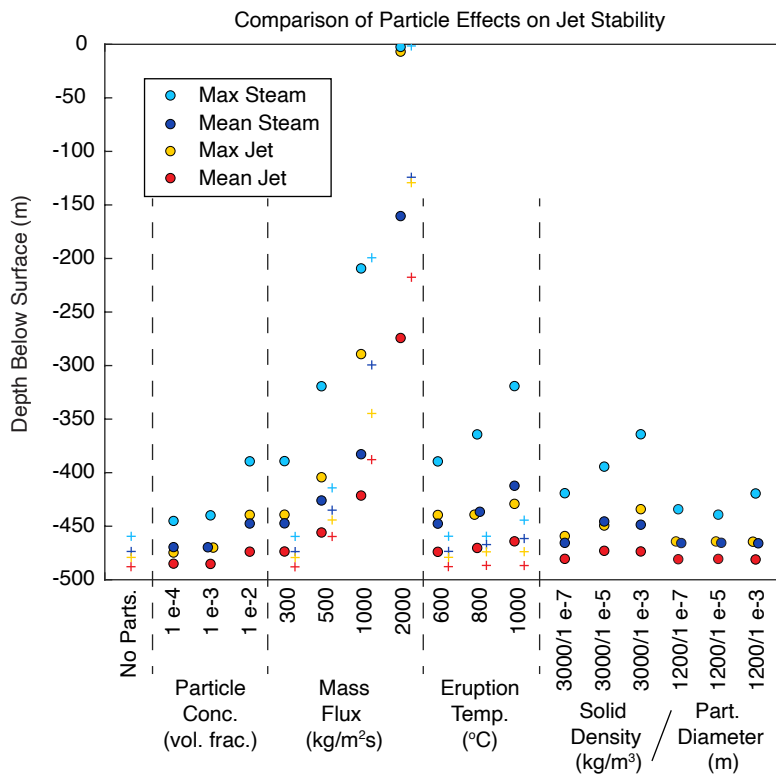


Figure 10. Comparison of particle effects on jet and steam height. Simulations were conducted at 500 m water depth, 600 °C eruption temperature, 1e-2 particle volume fraction, 300 kg/m²s mass flux, 1e-2 m particle diameter, and 3000 kg/m³ solid density. An individual parameter was systematically modified to determine the effects of each on the jet and steam heights. Note the furthest left simulation has no solid particles. Offset colored plus markers (+) indicate similar eruption conditions without particles.

We evaluate two particle densities (1200 and 3000 kg/m³) with three different particle diameters (1e-7 m, 1e-5 m, and 1e-3 m) and find substantial increases in jet and steam heights with the higher density cases. We also note a general increase with increasing particle diameter. These findings are thought to result from the increase in thermal inertia with larger and denser particles. Physical processes not accounted for in the continuum method prevent us from evaluating effects from larger particle diameters (> 1e-2 m). A simple test was conducted to evaluate whether changing vent diameter while maintaining vent discharge (mass flux times vent area) would have a substantial effect on jet height. It was found that vent diameter has, if any, a small, inconsistent impact on jet and steam height, varying by up to 4% (Figure 11).

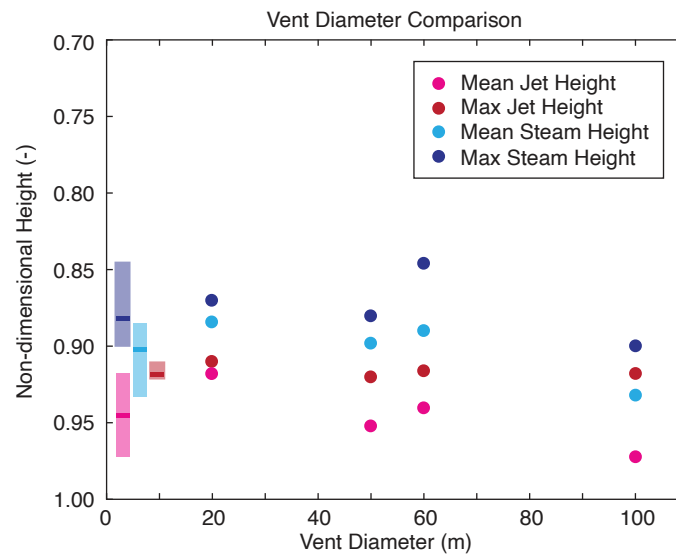


Figure 11. Comparison of jet and steam heights for different vent diameters. Filled circles represent data from a single simulation, all at 1000 °C, 500 m water depth, and a consistent discharge rate of 1.23e6 kg/s, varying only vent diameter and mass flux. The vertical bars represent the total range of values across the simulations with the mean shown by the darkened bar.

Discussion

The submarine eruption jet simulations allow us to gain new insight into condensable jets in submarine eruptions. From the simulations alone we can qualitatively analyze certain components of jet behavior. First, we can begin to get a stronger idea of jet morphology. From the DCC literature and the simulation results, we can say that jets in submarine eruptions appear to be dominantly conical with variations in height, width, roundness, and stability. We see that jet height is largely dictated by mass flux and eruption temperature, while jet width is also impacted by vent width. In the foundational work on deep water pyroclastic eruptions, Head and Wilson (2003) utilize the jet mixing relationship first proposed by Prandtl (1949) that characterizes mixing of fluid jet into a fluid of similar density. They assume a fixed geometry where complete mixing of a volcanic jet occurs below a height equal to six vent diameters. Contrary to this proposition we find that vent width is only a contributing factor to the produced jet height and jet heights can, and often do, exceed this estimation. The post vent flaring of a jet is largely dependent on the state of compressibility in the conduit and above the vent. Though we don't spatially resolve this, we gather from DCC experiments that jets may be straight conical if subsonic or ellipsoidal if sonic/supersonic (Chun et al., 1996). The conical shape we see in our simulations is defined by condensation processes at the jet/water interface, where increases in interfacial area are smoothed out by increased condensation leading to surface area minimization. In addition to aspects of jet morphology, we can also gain insight into the extent of the mixing zone around the jet. The pure gas jet simulations show mixing zones that are consistently thinner than the vent

itself, and generally do not expand with increased simulation time. This occurs largely due to the fact that the heated water is rapidly transported upward due to two processes. First the heated water develops buoyancy that causes it to accelerate upward. Second, significant vertical momentum is transferred from the jet to the surrounding water in the mixing zone. These two processes act to propel mixed water towards the surface and keep the mixed zone rather thin (i.e. less than the vent radius, as depicted in Figure 12).

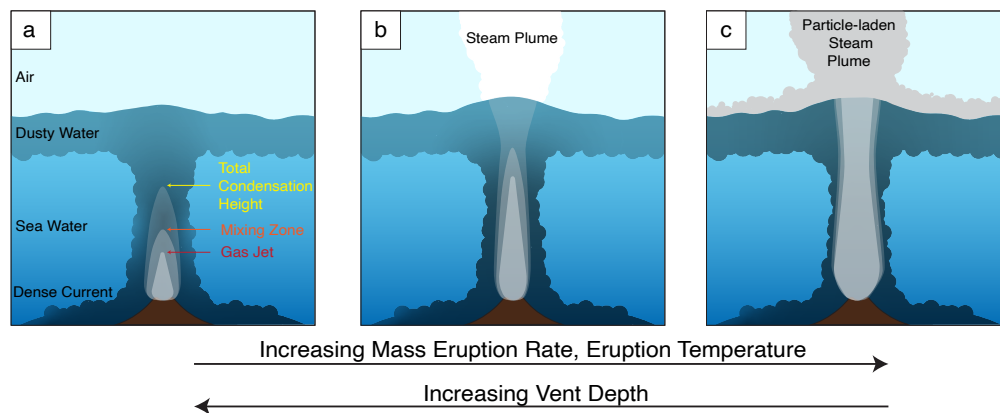


Figure 12. Schematic illustration of submarine explosive eruptions with varying eruption conditions. Panel (a) highlights the gas jet and steam terminus heights utilized in analysis. (a) eruption conditions lead to full condensation of erupted steam below the water surface. No erupted steam would be present at surface, though syn-eruptive surface displacements and SSTAs are possible. (b) Intermediate case where steam breaches the sea surface yet the erupting jet does not. This case can inject an abundance of steam into the atmosphere, though significant tephra in the atmosphere is unlikely. (c) The full jet breach is the most hazardous of the three cases, where significant steam and tephra breach the surface and a sub-Plinian plume is possible.

We can also conceptualize simulation results in relation to breaching. There is clearly a difference between a minor breach (steam breach) and a major breach (jet breach). With a steam breach, as we have defined it, we expect a minor amount of steam likely carrying little to no particle loading as the steam bubbles have likely disrupted and the particles, with the possible exception of the smallest particle fraction, will have

decoupled from the carrier gas. A jet breach, however, may be energetic and transport a substantial amount of tephra to the atmosphere, potentially forming what would resemble a subaerial volcanic plume. Additionally, there is need to differentiate between steady breach, where the mean peak height represents breaching, and one that has discrete breaching pulses or oscillatory breaches, where the max height but not the mean height best represents the eruption. The former may only be detectable shortly after breach, while the other represents a near continuous stream of gas to the surface (Figure 12). From the flux-temperature-height maps it is clear that breaching is possible in explosive eruptions originating from 200 m or less, and highly unlikely from greater than 1000 m water depth. At an intermediate depth of 500 m, both steam and jet breaches are possible depending on eruption conditions. The analysis presented here is separate from a consideration of gas volumes that could be exsolved based on pressure constraints from

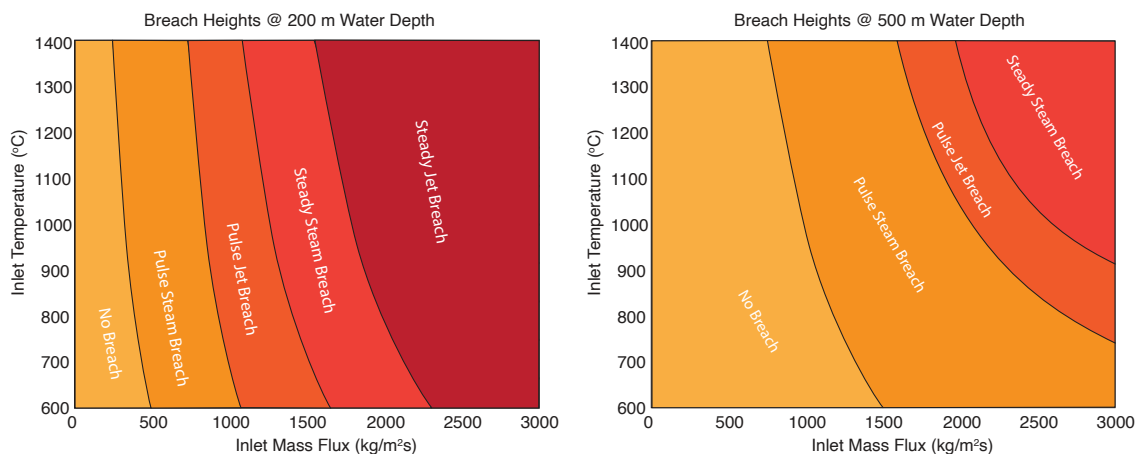


Figure 13. Regime diagrams show which mass flux and eruption temperature combinations would favor each breach regime at 200 m and 500 m water depth. As an example, any eruption with steam mass flux of 1500 kg/m²s at 500 m depth or shallower could produce at least a pulse steam breach. One would expect at least minor to significant steam breaching with little to no solids.

these water depths. Wilson and Head (2008) and Cas and Simmons (2018) have noted transitions in eruptive regime determined theoretically based on water depth, melt water content, solubility, fragmentation, and by comparing these calculations with submarine volcanic deposits. These studies highlight a similar spectrum of regimes that are predominantly controlled by available gas, moving from effusive lava flow/dome eruptions to fire fountaining to explosive eruptions with or without collapsing columns, as available exsolved gas increases. In the presentation of our data, we ignore this dependence and assume that sufficient gas is available for efficient fragmentation and explosive eruption. While this may make some of the endmember results less significant, it does not remove the base value of a complete and independent portrayal of the range of potential steam jet eruptions in volcanic systems.

We can condense the breaching information from the flux-temperature-height maps into a breach regime map (Figure 13) for this intermediate depth that focuses on the transition from one breach type to another which might show changes in eruption conditions. Figure 14 shows the percentage of erupted steam that breaches the surface across the simulation parameter space. It is apparent at higher fluxes that over 80% of erupted steam can breach the surface from 200 m depth, while it is not likely to breach over 20% of steam from 500 m.

Analysis of the SSTA and sea surface displacement gives us an opportunity to compare to real world measurements when they are taken. We show that SSTA is significant and always positive, even for lower eruption fluxes, and that it is likely to

have an oscillatory radial zoning mimicking the behavior of the eruption jet, though these zones are likely sub-resolution of satellite measurements. Therefore, spatially averaged

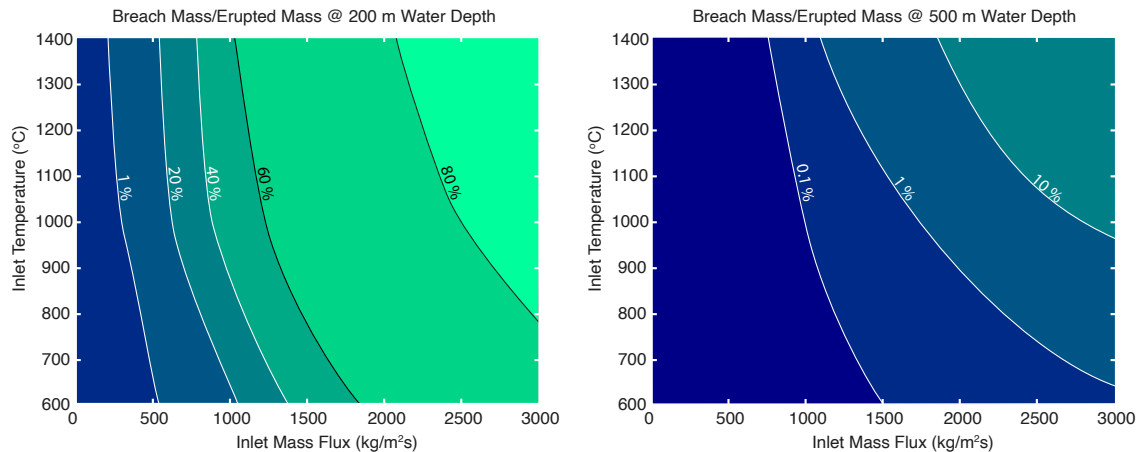


Figure 14. Contour plots illustrating the relationship between eruption conditions and steam breach percentage. Contours depict the percentage of total steam erupted that breaches the ocean surface at 200 m and 500 m water depths.

temperatures do not approximate maximum temperatures that may have a significant impact on local biology. We also show that sea surface displacement is perhaps a chief hazard for these types of eruptions, especially at shallow and intermediate eruptions, though fairly insignificant for deeper eruptions. While both of these findings are noteworthy, further investigation is necessary before we can begin to quantify the connection between eruption conditions, surface measurements, and their associated hazards, such as tsunamis and water column-spanning fish kills.

The influence of solid particles on jet dynamics is one of the more intriguing determinations of the study, and one that warrants a closer look. Our data show that the presence of particles has varying effects on jet dynamics and may initiate jet collapse

above a certain loading threshold, as witnessed in the transition from jet stabilizing to jet destabilizing behavior at 500 kg/m² mass flux (Figure 10). Before this loading threshold, the effects from solid particles can be attributed to added thermal mass, which buffers cooling and delays condensation, and added inertia, which propels steam higher in the domain. Both of these are evidenced by the slight changes to mean jet and steam heights concurrently with substantial increases in max jet and steam height in Figure 10. When the particles cluster before rapidly rise, the high particle concentrations in the cluster buffer heat loss and can transport steam to higher reaches in the water column.

Evaluation of the Particle Stokes Number provides us with the opportunity to explore particle coupling in multiphase flow transport. In the submarine volcanic gas jet, coupling becomes complex when you must account for rapid changes across a sharp density interface. We define particle Stokes number as:

$$St = \frac{D_p(\rho_p - \rho_h)|u_p - u_h|}{18\mu_h} \quad (11)$$

For example, consider an eruption with particles of 1200 kg/m³ density and 1mm diameter at 1% particle concentration at the vent, with an eruption temperature of 800 °C, initially erupted at 30 m/s and a water depth of 500 m. At 10 m above the vent, inside the gas jet the Stokes numbers is 557. This represents particles that are strongly decoupled from the flow. Just 30 m above this, beyond the extent of the gas jet, the particle Stokes number is measured at 0.3, showing that particles are coupled to the flow at this point. This transition from poorly coupled to coupled to the flow results from the rapid

escalation of viscosity across the gas-water interface. Conceptually this means particles that are disengaging from the flow in the gas jet, can be re-lofted once passed into the water. This could have an important consequence for interpreting particle distribution in the water column, where larger-denser particles may be observed at higher portions of the water column than could be transported within gas jet. Consequently, when contemplating the jet collapse phenomenon and particle dispersal, one must consider particle coupling in both the gas jet and the surrounding heated water.

We would also note that particle phases are likely having sub-resolution effects that are not being evaluated in this model due to the nature of the interface. One of these could be the effect of particle loading at the jet-water interface potentially limiting thermal heat transfer rates and thermally insulating the jet momentarily. Additional work is necessary to evaluate how jet conditions affect particle transport and dispersion in the water column, and how this affects the thermal evolution of the surrounding water column.

Conclusion

Submarine explosive gas jets are one of the missing links to understanding submarine eruptions. This study shows that jet height and stability is foremost controlled by mass flux, followed by eruption temperature, and vent width, though water depth is critically important as well. Solid phases can have an impact though it is not critical until they overburden the jet to cause a collapse via decoupling. Steam and jet breaches are two of the critical hazards associated with these eruptions. This study establishes bounds

on these at three water depths, 200 m, 500 m, and 1000 m. It is clear that surface breaches are highly possible at 200 m, likely not possible at depths as great as 1000 m, and possible at 500 m, though highly dependent on eruption conditions. We show that there are clear relationships between eruption conditions, water depth, and the likelihood of a surface breach. We conclude that future work needs to be conducted to further establish a quantitative and reliable mechanism for linking eruption breach, SSTA, and surface observations to eruption conditions at the vent. Additionally, extension of this work to study tephra dispersal and atmospheric plume development resulting from subaqueous eruption jets would help elucidate the connection between submarine eruption deposits and the eruption conditions that formed them.

CHAPTER III

PARTITIONING OF VOLCANIC TEPHRA DURING SUBAQUEOUS EXPLOSIVE ERUPTIONS

Introduction

One of the principle objectives of volcanology is to determine how erupted material is transported and to anticipate where it will be deposited, with the ambition of determining hazards in future eruptions. Submarine eruptions exhibit phenomena which make prediction and interpretation of tephra emplacement difficult compared to the subaerial counterpart. Cas and Simmons (2018) and McBirney (1963) detail many of the processes and relationships that preclude treatment of subaqueous eruptions in a similar manner to subaerial ones. For example, when considering the complexity of buoyancy evolution during an eruption, rapid changes in density can critically alter the dispersal of volcanic materials. Magmatic gases erupted into a subaqueous environment have a much greater density contrast relative to ambient seawater than comparable gases erupted in subaerial environment. Particularly water vapor, which can cool and rapidly condense, can generate large density fluctuations in the driving eruptive fluid. Also the dispersed, fragmented volcanic materials have a potentially much more complex density history in the submarine environment. Pumice clasts of any size can be erupted into water at a buoyant density ($<1000 \text{ kg/m}^3$), and as they cool they rapidly densify by condensing interior gases and ingesting seawater (Allen et al., 2008; Carey et al., 2018; Manga et al., 2018; Manville et al., 1998; Whitham & Sparks, 1986). The release of a large volume of gas by efficient fragmentation of a bubbly melt can inject a dusty-gas jet into the water column which may buoyantly rise to the surface (Kano et al., 1996), or rapidly mix with

seawater, cool and condensing the internal steam, and collapse to feed pyroclastic density currents from the detrained particle mixture (Cas & Simmons, 2018; Cas & Wright, 1991; Fiske & Matsuda, 1964; Kano et al., 1996). Each of these processes contribute to the emplacement of tephra at specific depths in the water column, and ultimately dictate the dispersal mechanism and deposits of the eruption. Most tephra dispersal mechanisms, with the case-dependent exception of density currents, are influenced by ocean current velocity (Fiske et al., 2001; Jutzeler et al., 2014; Manga et al., 2018). In the ocean, current velocity can, and often does, change in magnitude and direction at different water depths (Joseph, 2014). Because of this, the same volume of volcanic ash emplaced at two different water depths may not only differ in deposit extent or thickness but may completely diverge due to the predominant “down-wind” direction. A lack of observations has largely prevented the direct correlation of eruption dynamics with tephra dispersal mechanisms in submarine eruptions deeper than 10s of meters (Cas & Simmons, 2018). A link between eruption conditions, (i.e. water depth, mass eruption rate, eruption temperature) and mass partitioning in the water column is needed to better interpret the deposits from subaqueous eruptions, past and present, and assess the hazards of future eruptions.

Volcanic tephra dispersal in the submarine environment can have wide-ranging effects on the regional environment. From a human hazard perspective, surface-breaching eruption columns can produce subaerial eruption plumes, basal surges, and large breaches of tephra, gas, and water mixtures, which can pose a threat to nearby populations, ships, and aircrafts (Cas & Simmons, 2018; Fiske et al., 1998); subaqueous density currents can

damage seafloor infrastructure (e.g. pipelines and cables) (White, 2000); pumice rafts can impact shipping lines and maritime transportation (Bryan et al., 2012; Jutzeler et al., 2020); and suspended fine ash “clouds” can be transported 10s to 100s of kilometers in water and cripple with aquaculture endeavors (Zimmerman et al., 2008). Submarine eruptions can have significant biological impacts in the forms of fish kills (Santana-Casiano et al., 2013), nutrient fertilization for chemosynthesis or algal blooming (Kelley et al., 2002), and long-range dispersal of micro- and macrofauna species on pumice rafts (Bryan et al., 2004, 2012; Velasquez et al., 2018). Each of these human and biological impacts is primarily controlled by the mass partitioning of erupted material in the water column and atmosphere.

Deposits from deep (>200 m) submarine explosive eruptions have often been hypothesized as incompletely preserved, owing to potential transport and far-field deposition of material via ocean currents and winnowing of fines during transport (Carey et al., 2018). Anomalously low concentrations of ash-sized particles are common in subaqueous deposits. This has been hypothesized to be a result of two possibilities: (1) ash is transported away from source either syn- or post-eruption and is redeposited as thin, undetectable layers mixed within marine sediment (Walker et al., 2008); (2) ash is simply not generated, due to the reduced efficiency of fragmentation resulting from effects of hydrostatic pressure (Manga et al., 2018). The present study evaluates the transport of dispersed-ash phases in subaqueous eruptions to determine the correlation between eruption jet conditions and subaqueous tephra transport mechanisms. In doing

so, we provide insight on the first of the two missing submarine ash hypotheses and provide estimates to the question, where *does* the ash go?

Tephra transport in subaqueous eruptions occurs primarily within gravity flows driven by the buoyancy state of a particle-laden fluid. In explosive eruptions, a steam jet bearing solidifying melt fragments is ejected into the water column (Figure 15). Much like the subaerial case, the flow is initially driven by inertia and hence is referred to as a jet. If the bulk density of the jet is greater than the surrounding water, the jet will rise until inertia from gas expansion in the conduit is dissipated and the jet collapses. If the bulk density of the jet drops below that of water, the flow will accelerate upwards, becoming a buoyant plume, and mix with seawater at its edges. The steam dominating the volatile budget in the plume will begin to cool and condense at the jet-water interface, while simultaneously, the entrained seawater may vaporize. If enough condensation occurs, the plume will densify and collapse. This particle loading threshold can be estimated by comparing the bulk densities of the fluid with the density of ambient water:

$$\rho_{blk} > \rho_a \quad (12)$$

$$\varepsilon_p > \frac{\rho_a - \rho_s \varepsilon_s - \rho_w \varepsilon_w}{\rho_p} \quad (13)$$

$$\varepsilon_p > \frac{1030 - 10\varepsilon_s - 980\varepsilon_w}{2200} \quad (14)$$

Here ρ_{blk} is bulk density, ρ_a is ambient density (i.e. seawater), ρ_w is local water density, ρ_p is solid particle density, ρ_s is steam density, ε_s is steam volume fraction, ε_w is liquid water volume fraction, and ε_p is particle volume fraction. Particle loading buoyancy reversal thresholds for coupled homogenously distributed flows are ~46% for air and ~4% for heated water (using ~ 98° C, 1 atm). Above these particle concentrations, the flow becomes negatively buoyant and collapses. While the threshold for a seawater-particle flow may be accurate, particle-flow decoupling, as well as local instabilities, heterogeneities, and clustering effects in the gas-particle flow, may drive particles to detrain from the flow far below this concentration, which may also generate partial collapse. The de-coupled and collapsing tephra can generate dynamic features including density currents that rapidly flow downslope and sheet clusters that form along the edge of large eddies before draping downward on the seafloor and deposit in a sheet. The particle Stokes number estimates the coupling of a given particle population in a flow by comparing the particle response timescale (τ_p) and the flow timescale (τ_h), defined as:

$$S_T = \frac{\tau_p}{\tau_h} = \frac{D_p^2(\rho_p - \rho_h)|u_p - u_h|}{18\mu_h L} \quad (15)$$

Where D_p is particle diameter, ρ_p and ρ_h are solid and hydrous fluid density (steam-water mixture), respectively. u_p and u_h are solid phase and hydrous mixture velocity, μ_h is hydrous mixture viscosity, and L is a characteristic length scale, here defined as the large eddy diameter. When the Stokes number is $\ll 1$, suspended particles are strongly coupled to the fluid and closely follow streamlines. When S_T is $\gg 1$, particle

motion is weakly coupled to fluid motion. Near $S_T \sim 1$, particles can remain coupled in a fluid though are pushed to the periphery of developing eddies, sometimes escaping. The case of subaqueous explosive eruptions is somewhat unique in terms of particle Stokes number consideration. At the erupting vent, particles erupted in a buoyant gas jet typically have $S_T > 1$ (high particle-gas density contrast, low gas viscosity). Here all but the smallest, lowest density particles will decouple from the fluid and gravity causes the particles to decelerate. As the particles decouple from the gas and pass through the jet-water interface, they enter into a completely different Stokes regime, where the small

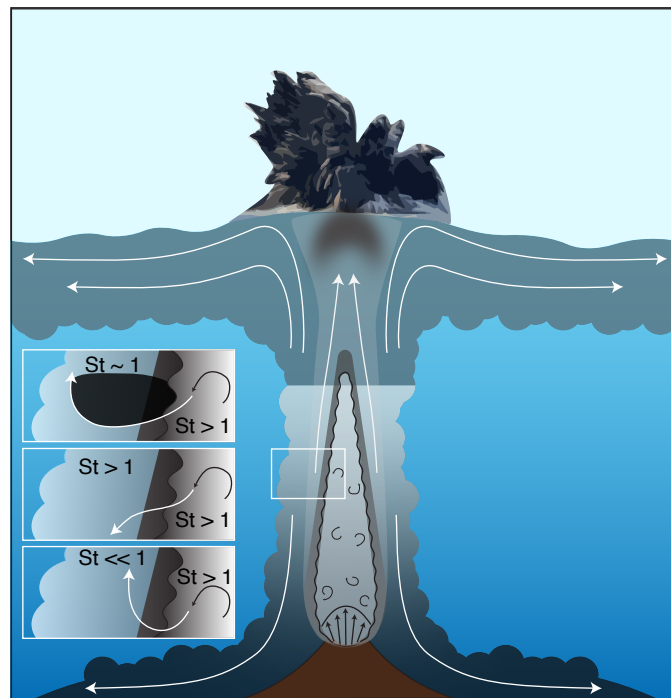


Figure 15. Schematic diagram of eruption dynamics in explosive subaqueous eruptions. Break out boxes show the path of particles with different Stokes numbers from the gas jet to the water column. Black arrows denote internal jet turbulence. White arrows are flow lines highlighting jet-periphery collapse, surface plume rise and radial spreading, and near jet particle concentration and lofting.

density contrast and a viscosity roughly two orders of magnitude greater than steam enables flow coupling with larger and denser particles (S_T decreases by >100x). Figure 15 shows conceptually how this rapid transition may allow particles to “fall” out of a jet to be rapidly lofted by a rising water plume and radially and vertically segregates particles by Stokes number in the eruption column.

Another method to define the stability of a particle population in a flow is to calculate the stability factor which evaluates the role of gravity on particle residence in an eddy (Raju and Meiburg, 1995; Burgisser and Bergantz, 2002). The stability factor is a ratio of Stokes to Froude numbers:

$$F_R = \frac{u_p - u_h}{\sqrt{g'L}} \quad (16)$$

$$g' = g \frac{\rho_p - \rho_h}{\rho_p} \quad (17)$$

$$\Sigma_T = \frac{S_T}{F_R^2} \quad (18)$$

Here g is gravitational acceleration and g' is reduced gravity. We use g' to denote the alteration of buoyancy forces due to changes in particle density. When $\Sigma_T \ll 1$, particles will stay entrained within the eddy without the influence of additional forces. When $\Sigma_T \gg 1$, particles will tend to settle from the eddy by gravitational forces. By evaluating S_T

and Σ_T in concert, we can anticipate the behavior of particles of varying size and density in the presence of different flow states in the system.

As the buoyant jet rises, shearing along the jet-water interface will drive viscous dissipation of energy in the flow and can instigate tephra to decouple from the flow and be entrained in the water. Upon entering the denser and more viscous water, the particles can be re-coupled and lofted upward toward the surface or continue downward to form a collapsing counter current which can ultimately feed density currents. Lofted plumes may rise to the surface, with or without particles. Upon reaching the sea surface, the vertical inertia of the plume displaces the sea surface and then pushes outward into a radially spreading surface plume. Alternatively, a rising buoyant plume that possesses insufficient inertia or buoyancy can stall at sharp density boundaries, such as the thermocline or halocline. This phenomenon can generate one or more radially spreading plumes at intermediate depths.

Internal, turbulence-driven shear in the column can generate low Stokes particle clustering via drag reduction, and can alter the local flow properties to favor detrainment from the flow. Additionally, the fluid volume-reducing nature of condensation can drive clustering of particles, both at the jet-water interface and internally in the jet, further enhancing this effect.

A sufficiently energetic eruption may penetrate through the water column and breach the surface. Chapter 2 outlines regimes of jet breach and details differences

between small volume breaches of steam pockets with or without fine ash and full jet breaches, where a steady or non-steady continuous jet connects between vent and surface. These jets can behave similarly to a subaerial eruption for seconds to minutes before collapsing and needing to re-clear the onrushing water. Certain eruption conditions favor the development of one breach regime over another, and vent mass flux or mass eruption rate tends to be the determining parameter (Chapter 2). Jet breaches are the most extreme example of submarine hazards though the underlying physics has only recently become a priority to define.

We identify two key relationships to define particle dispersal in subaqueous eruptions. First, we describe the difference in transport and mass partitioning patterns between high-energy hydrothermal plumes and those eruptions that begin with fragmentation and a pyroclastic gas jet. Second, quantify trends in particle dispersal and eruption column behavior resulting from changes in particle characteristics, as well as the inertial, thermal, and compositional conditions at the vent. We utilize the 2D multiphase subaqueous eruption model developed in Chapter 2 to investigate particle dispersal in the ocean resulting from explosive and nonexplosive eruptions. We analyze the model results by assessing the partitioning of erupted mass between different zones in the water column. Then we compare these partitioning bins for different parameter sets to determine the relationship between eruption parameters and water column emplacement and ultimately tie these to particle dispersal mechanisms.

Methods

Mass partitioning of erupted volcanic tephra is determined to demonstrate the relationships between eruption conditions and dominant particle dispersal mechanisms in subaqueous eruptions. To achieve this result, we utilize the multiphase continuum approach for subaqueous eruption modeling presented in Chapter 2 to model eruptions with a range of initial and inlet conditions (i.e. vent velocity, eruption temperature, water depth, water density profile) and solid particle parameters (i.e. diameter, density, concentration) with and without a steam jet. Figure 16 is an example of a simulation with characteristic domain dimensions and boundary conditions, as well as the partitioning zones outlined in section 2.4.

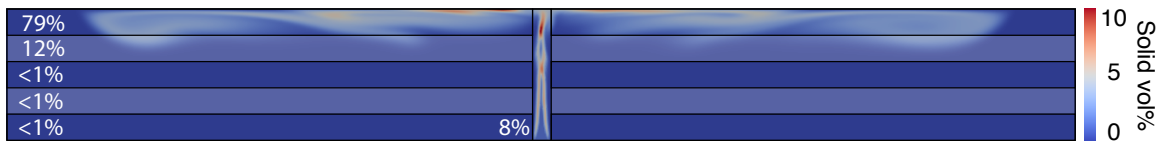


Figure 16. Example simulation with partitioning zones. Note the central column zone encapsulates the eruption column, which is removed from consideration in mass partitioning calculations. In this simulation, the gas-particle jet extends into the mid-column zone. Examples of particle clusters can be observed in the central column in strong red color. These clusters correlate to jet oscillatory behavior and are responsible for the discrete flow units at in the surface zone.

Model: Gas Jet vs No Gas

We conducted a series of models with high velocity gas-particle jets, followed by models with similar conditions but without steam to compare dispersal in gas jets and heated water plumes. Equivalent heat flux conditions were calculated by:

$$J = \rho_w c_{P,w} T_{sat} u_w = \rho_s c_{P,s} T_s u_s \quad (19)$$

$$u_{wp} = \frac{\rho_s c_{P,s} T_s u_{sp}}{\rho_w c_{P,w} T_{sat}} \quad (20)$$

Where J is heat flux, ρ_w is water density, $c_{P,w}$ is heat capacity of water, T_{sat} is saturation temperature of water, u_w is water velocity, ρ_s is steam density, $c_{P,s}$ is heat capacity of steam, T_s is temperature of steam, and u_s is steam velocity. This relationship allows us to maintain heat flux between gas jet and gas-less eruptions, as if the jet would have been completely condensed before erupting. For example, for a gas jet with $\rho_s = 1 \text{ kg/m}^3$, $u_{sp} = 100 \text{ m/s}$, $c_{P,s} = 1073 \text{ J/kgK}$, and $T_s = 800 \text{ }^\circ\text{C}$, would have a gas-less equivalence with $\rho_w = 1000 \text{ kg/m}^3$, $c_{P,w} = 4186 \text{ J/kgK}$, and fluid temperature at the saturation threshold, $T_{sat} = 373 \text{ K}$. The calculated thermal flux-equivalent velocity is $u_{wp} \sim 0.14 \text{ m/s}$. The equivalent eruption velocities calculated utilizing this method are quite small, and therefore a second group of models were run in addition to these to assess cases where an additional inertial component is inherited from the erupting process (i.e. effusive flow or fire fountain, +1 - 10 m/s). We also evaluated cases where particle mass eruption rate was maintained, though, with the low volume fluxes calculated for the gas-less eruptions, the particle concentrations were consistently higher than the loading threshold, somewhat unrealistic, and *immediately* collapsed upon eruption.

Model: Particles and Eruption Parameters

We performed a series of simulations to compare the effects of different eruption parameters on mass partitioning in the water column, including vent velocity and eruption temperature, as well as particle diameter, density, and concentration. As outlined in the introduction, these initial and boundary conditions can prescribe dispersal dynamics due to their contribution to particle flow coupling, as evaluated by Stokes number and stability factors. To test the influence of each parameter listed above, we perform two model runs at each value, each with one of two different particle parameter sets. These particle parameter sets are consistent throughout simulations (values in Table 4), with only the parameter of interest modified.

Table 4. Particle Parameter Sets

Parameter	Set #1	Set #2
ρ_p (kg/m ³)	2200	3000
D_p (m)	1e-4	1e-2
T_i (°C)	800	1000
ε_p (-)	1e-3	1e-2
u_v (m/s)	50	100

Mass Partitioning Calculations

The quantification of mass partitioning involves tracking the distribution of particles in the domain at the end of a designated amount of simulation time. We choose the default simulation duration to be 600 s, as this is sufficient time for the lowest flux models to completely develop before the simulation is terminated. In highly dynamic

simulations where the eruption dynamics begin to be influenced by undesired wall effects after some amount of time, we only assess timesteps before this point. As seen in Figure 16, the domain is horizontally split into 100 m thick zones (five in a 500 m simulation) as well as an additional central vertical zone as wide as the vent (60 m) extending from the vent to the top surface. We integrate the particle mass across each horizontal zone and divide by the total erupted solid mass minus the mass of solid in the central zone to arrive at the percentage of total mass emplaced at each of the five depth bins. We remove the erupted mass in the central zone from the total mass to eliminate the appearance of “transient mass” still entrained in the upward-coursing jet from the calculated emplacement percentages. This avoids over-estimation of mass partitioning in the subsurface zones.

Breaching Mass Calculations

Additional consideration must be taken to account for surface breaching particles in the mass partitioning calculation. Because the central upper boundary condition does not allow solid particles to leave the domain, breaching particle mass must be calculated and removed from the surface zone (upper 100 m). We calculate the total mass of breaching particles (M_{pb}) throughout the simulation:

$$M_{pb} = \int_0^t \int_0^x u_p \rho_p X_p \varepsilon_s z \, dx \, dt \quad (21)$$

Where t is total time, x is the integrated length of an interface, u is the vertical velocity component of the rising particle-gas-water mixture, ρ_p is particle density, X_p is particle

mass fraction in a cell, ε_s is steam volume fraction in a cell, z is the cell depth, dx is grid resolution in x dimension, and dt is the temporal resolution of the simulation. We consider the fraction of particles transported in the steam phase as those that can escape; this is estimated by multiplying the local particle mass by the local volume fraction of steam before integrating, thus ignoring particles carried in liquid water. This mass is removed from the surface zone and presented as the percentage of erupted mass that breaches the surface.

Results

Our simulations predict distinct differences in tephra mass partitioning due to different eruption conditions. Here we present results for 80 multiphase simulations of subaqueous explosive eruptions at 500 m water depth. We present these results below organized into sections by individual parameters. Each section is accompanied by one of Figures 17-21 that display the percentage of total erupted mass emplaced at six different zones in the water column (five 100 m tall sections and an atmospheric breach). In these figures each zone is represented as a bar whose height is representative of the mass percentage in that zone. An important note, since particle breach is important even at low mass percentages, we have increased the relative height of the breach bars by 10x to be more easily discerned. We also present comparisons between explosive jet eruptions and equivalent heat flux simulations for no-gas eruptions. These no gas simulations can be thought of as either an eruption where all gas is condensed in the sub-vent conduit or streaming hydrothermal fluids lofting fragmented particles in a plume. Numerical values for all simulation inputs and results are included in Table 5.

Table 5. Simulation Parameters and Mass Partitioning Results

Run ID	Regime	D_p (m)	ε_p (-)	ρ_p (kg/m ³)	u_v (m/s)	T_i (°C)	MER (kg/s)	Mass Fraction Solids by Water Depth/Zone						
								Top 100m	100- 200m	200- 300 m	300- 400 m	Bottom 100 m	Breach	Central Column
34	C	1E-2	1E-2	3000	10	1000	8.39E+7	0.38	1.59	3.39	2.54	81.15	0.00E+0	10.93
35	PC	1E-2	1E-2	3000	50	1000	4.20E+8	20.08	21.68	10.16	8.17	26.07	0.00E+0	13.84
36	B	1E-2	1E-2	3000	100	1000	8.39E+8	71.56	19.83	0.04	0.00	0.00	3.09E-2	8.52
37	JB	1E-2	1E-2	3000	150	1000	1.26E+9	72.83	20.05	0.12	0.00	0.00	1.08E+0	5.86
38	JB	1E-2	1E-2	3000	200	1000	1.68E+9	72.04	14.57	0.01	0.00	0.00	6.36E+0	6.16
39	JB	1E-2	1E-2	3000	300	1000	2.52E+9	66.77	12.83	0.00	0.00	0.00	1.08E+1	9.59
40	NC	1E-4	1E-3	2200	10	800	6.21E+7	71.24	16.20	0.16	0.00	0.00	0.00E+0	12.34
41	NC	1E-4	1E-3	2200	50	800	3.11E+8	63.01	24.00	2.66	0.00	0.00	0.00E+0	10.29
42	B	1E-4	1E-3	2200	100	800	6.21E+8	76.47	13.58	0.09	0.00	0.00	3.15E-5	8.08
43	B	1E-4	1E-3	2200	150	800	9.32E+8	77.37	16.35	0.12	0.00	0.00	2.81E-2	6.00
44	B	1E-4	1E-3	2200	200	800	1.24E+9	77.32	14.76	0.10	0.00	0.00	9.18E-3	5.81
45	B	1E-4	1E-3	2200	300	800	1.86E+9	73.16	20.57	0.52	0.00	0.00	1.16E-1	4.59
46	JB	1E-2	1E-1	3000	100	1000	7.63E+8	30.60	20.01	0.17	0.06	0.04	3.35E+1	15.52
47	B	1E-2	1E-2	3000	100	1000	8.39E+8	70.59	21.56	0.05	0.00	0.00	3.29E-1	7.75
48	B	1E-2	1E-3	3000	100	1000	8.47E+8	74.92	16.57	0.00	0.00	0.00	1.82E-4	8.48
49	NC	1E-2	1E-4	3000	100	1000	8.48E+8	71.18	14.55	0.01	0.00	0.00	0.00E+0	14.01
50	B	1E-4	1E-1	2200	50	800	2.80E+8	62.24	9.92	0.01	0.00	0.00	1.64E+1	10.92
51	PC	1E-4	1E-2	2200	50	800	3.08E+8	36.20	27.50	16.28	7.22	4.49	0.00E+0	8.29
52	NC	1E-4	1E-3	2200	50	800	3.11E+8	63.00	24.00	2.66	0.00	0.00	0.00E+0	10.28
53	NC	1E-4	1E-4	2200	50	800	3.11E+8	64.89	23.75	0.92	0.00	0.00	0.00E+0	10.14
54	PC	1E-2	1E-2	3000	100	600	8.39E+8	12.60	16.56	13.30	8.04	42.59	0.00E+0	6.90
55	B/PC	1E-2	1E-2	3000	100	800	8.39E+8	53.97	29.52	5.50	2.67	0.34	4.67E-4	7.98
56	B	1E-2	1E-2	3000	100	1000	8.39E+8	71.56	19.84	0.04	0.00	0.00	3.07E-2	8.52
57	B	1E-2	1E-2	3000	100	1200	8.39E+8	74.76	18.24	0.04	0.00	0.00	3.58E-1	6.53
58	B	1E-2	1E-2	3000	100	1400	8.39E+8	78.92	12.99	0.01	0.00	0.00	8.50E-1	7.20
59	NC	1E-4	1E-3	2200	50	600	3.11E+8	59.37	25.90	5.00	0.02	0.00	0.00E+0	9.65

Table 5. Simulation Parameters and Mass Partitioning Results

Run ID	Regime	D_p (m)	ε_p (-)	ε_p (kg/m ³)	u_p (m/s)	T_i (°C)	MER (kg/s)	Mass Fraction Solids by Water Depth/Zone						
								Top 100m	100-200m	200-300m	300-400m	Bottom 100m	Breach	Central Column
60	NC	1E-4	1E-3	2200	50	800	3.11E+8	63.00	24.00	2.66	0.00	0.00	0.00E+0	10.29
61	NC	1E-4	1E-3	2200	50	1000	3.11E+8	69.22	20.71	2.02	0.00	0.00	0.00E+0	6.12
62	NC	1E-4	1E-3	2200	50	1200	3.11E+8	69.94	21.07	1.70	0.00	0.00	0.00E+0	6.98
63	NC	1E-4	1E-3	2200	50	1400	3.11E+8	76.37	16.27	0.12	0.00	0.00	0.00E+0	6.66
64	B	1E-2	1E-2	3000	100	1000	8.39E+8	71.56	19.84	0.04	0.00	0.00	3.07E-2	8.52
65	B	1E-3	1E-2	3000	100	1000	8.39E+8	79.83	12.53	0.03	0.00	0.00	4.45E-1	6.79
66	B	1E-4	1E-2	3000	100	1000	8.39E+8	80.75	11.62	0.01	0.00	0.00	2.30E-1	7.27
67	B	1E-5	1E-2	3000	100	1000	8.39E+8	84.43	6.72	0.00	0.00	0.00	7.58E-1	7.95
68	B	1E-6	1E-2	3000	100	1000	8.39E+8	84.44	7.21	0.00	0.00	0.00	5.53E-1	7.78
69	NC	1E-2	1E-3	2200	50	800	3.11E+8	45.23	39.42	6.97	0.01	0.00	0.00E+0	8.31
70	NC	1E-3	1E-3	2200	50	800	3.11E+8	71.53	20.38	0.50	0.00	0.00	0.00E+0	7.49
71	NC	1E-4	1E-3	2200	50	800	3.11E+8	63.00	24.00	2.60	0.00	0.00	0.00E+0	10.29
72	NC	1E-5	1E-3	2200	50	800	3.11E+8	62.02	24.90	4.31	0.00	0.00	0.00E+0	8.28
73	NC	1E-6	1E-3	2200	50	800	3.11E+8	61.07	25.62	4.05	0.00	0.00	0.00E+0	8.92
74	NC	1E-2	1E-2	600	100	1000	1.68E+8	77.11	13.77	0.16	0.00	0.00	0.00E+0	8.70
75	B	1E-2	1E-2	1040	100	1000	2.91E+8	78.90	9.98	0.00	0.00	0.00	1.18E-3	11.10
76	B	1E-2	1E-2	1200	100	1000	3.36E+8	73.99	17.43	0.51	0.00	0.00	8.27E-7	8.05
77	B	1E-2	1E-2	2200	100	1000	6.16E+8	71.21	20.87	0.10	0.00	0.00	2.77E-2	7.78
78	B	1E-2	1E-2	3000	100	1000	8.39E+8	71.24	18.32	0.03	0.00	0.00	3.30E-2	10.37
79	NC	1E-4	1E-3	600	50	800	8.47E+7	65.65	23.11	2.59	0.00	0.00	0.00E+0	6.91
80	NC	1E-4	1E-3	1040	50	800	1.47E+8	62.57	26.12	1.98	0.00	0.00	0.00E+0	7.04
81	NC	1E-4	1E-3	1200	50	800	1.69E+8	63.94	22.64	3.66	0.00	0.00	0.00E+0	8.39
82	NC	1E-4	1E-3	2200	50	800	3.11E+8	63.63	22.07	3.81	0.11	0.00	0.00E+0	9.25
83	NC	1E-4	1E-3	3000	50	800	4.23E+8	65.08	24.45	2.55	0.00	0.00	0.00E+0	6.73

Vent velocity

The eruption velocity at the vent is one of two parameters that largely defines the initial inertial state of the eruption column and critically influences mixing and, thereby, condensation rates in the jet. We present two sets of simulations (one for each particle population listed in Table 4) each comprising simulations with vent velocities of 10, 50, 100, 150, and 200 m/s. Figure 17 shows the relationship between vent velocity and mass partitioning for each simulation. Set #1 is relatively insensitive to vent velocity with relatively constant partitioning behavior across simulations. The 50 m/s run shows an increase in downward mixing, extending the erupted mass into the 300-200 m zone. This results from decreased jet stability in the

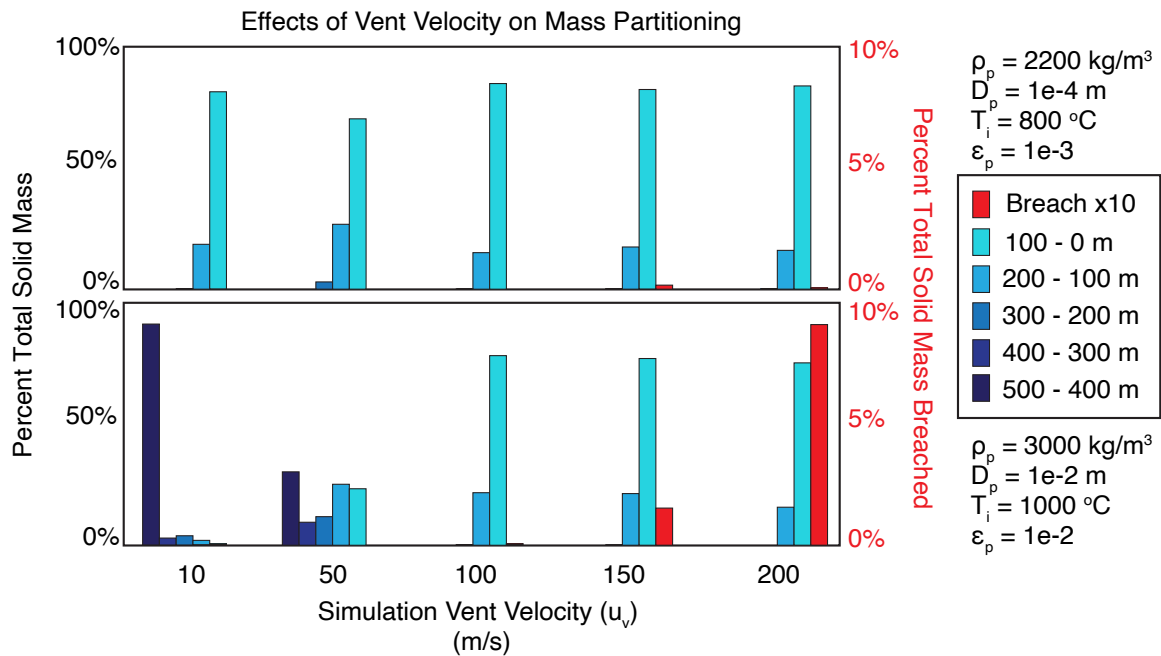


Figure 17. Effects of Vent Velocity on Mass Partitioning. Bar graph depicting the percentage of the total erupted mass (y-axis) that arrives into each zone in the water column (colored bars) for a given vent velocity (x-axis). The upper graph corresponds to particle parameter set #1, listed upper right, and the lower graph to particle parameter set #2, listed lower right. Note: breach mass percentage is show at 10x for clarity.

mid-column region that drives jet oscillations and vortex shedding. This increased mixing yields added mass in the mid-column zones. This does not occur for the lower velocity simply because the inertia is insufficient to propel the jet to the heights needed for instability. Instead the jet condenses just above the vent and the developed water plume gently rises to the surface. Above the 50 m/s case, inertia is high enough that the mid-column instability does not occur before reaching the shallower zones.

In set #2, the denser particles at higher concentrations generate a different suite of outcomes. The 10 m/s and 50 m/s simulations both dissipate sufficient inertia and collapse, though at different heights, and generate distinct mass partitioning signatures. The 10 m/s case rapidly deposits a majority of erupted mass near the vent and lofts small masses of particles via collapse-generated upward currents. Whereas the 50 m/s simulation involves a jet that rises high in the water column before expending its inertial budget and rapidly collapsing down in sheets. These sheets arise as the particles concentrate at the edges of circulating eddies and detrain from the flow. Above 50 m/s, increasing vent velocity generally increases the mass of breach from $\ll 1\%$ at 100 m/s to $\sim 9\%$ at 200 m/s. Besides the increasing breach mass, the mass partitioning in the water column is mostly similar, with a small decreasing trend in the mass present in the 200-100 m zone.

Particle concentration

Particle concentration is the second of the parameters controlling the inertia state of the eruption column, and also contributes to the thermodynamic state as increases in

particles elevate the thermal flux of the eruption. Increasing particle concentration leads to rises in particle-particle collisions, and effects from particle-gas drag and internal shear development. We present two sets of simulations each comprising runs with particle volume fractions of $1e-4$, $1e-3$, $1e-2$, and $1e-1$. Figure 18 shows the relationship between initial particle concentration and mass partitioning for each simulation.

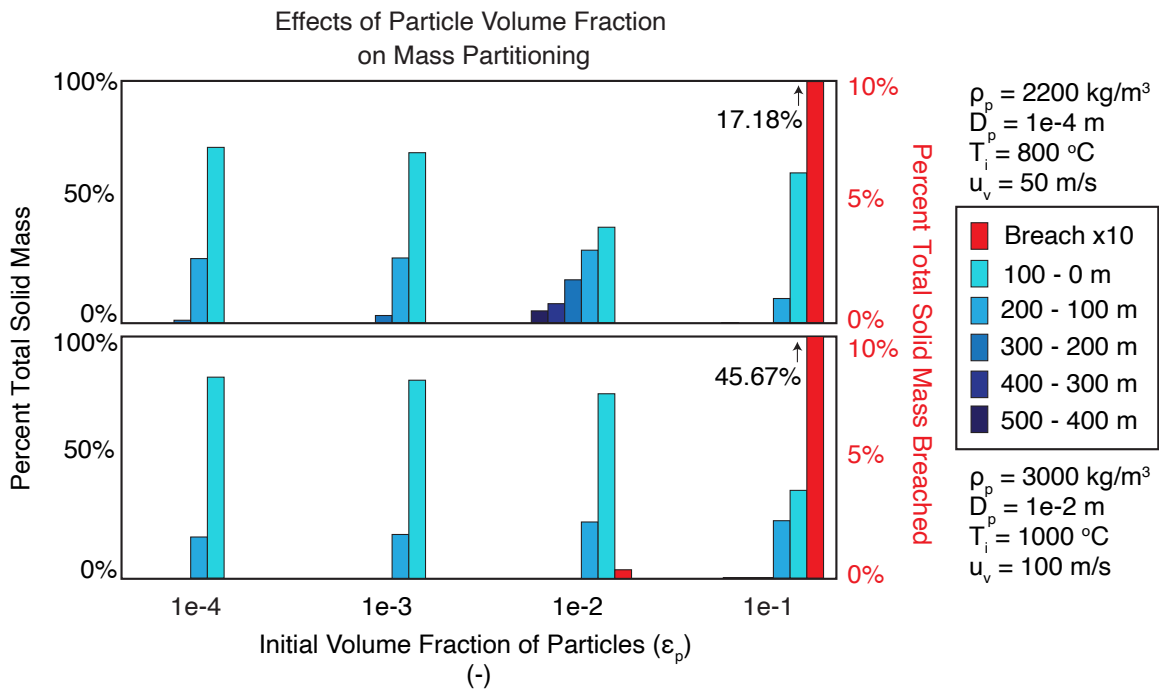


Figure 18. Effects of Particle Concentration on Mass Partitioning. Bar graph depicting the percentage of the total erupted mass (y-axis) that arrives into each zone in the water column (colored bars) for a given initial particle volume fraction (x-axis). The upper graph corresponds to particle parameter set #1, listed upper right, and the lower graph to particle parameter set #2, listed lower right. Note: breach mass percentage is shown at 10x for clarity.

The simulations in set #1 show a deepening trend, from predominant emplacement in the upper water column to high-column collapse and broad mid-column emplacement at $1e-2$ volume fraction. The form of this high-column collapse is different than that of the set #2 50 m/s case in the section above. Here the jet propels the majority

of the mass to the surface which begins to spread outwardly as a radial plume, but quickly loses momentum and slowly settles in horizontal units through the water column. These horizontal units originate from oscillations at the top of the jet that deliver isolated currents to the right and left, back and forth. This phenomenon does not appear similar to that which produces the collapsing sheets noted above. Set #2 displays a similar deepening trend, though continuous without the collapse feature seen in set #1 at $1e-2$ volume fraction, followed by a massive jet breach at the highest particle concentration.

Eruption Temperature

The eruption temperature parameter primarily controls the initial thermodynamic state of the eruption. Eruption columns that initiate at lower temperatures are more likely to condense rapidly, which reduces jet height and the time for mixing and heating of seawater for water plume development. We present two sets of simulations each comprising runs with eruption temperatures of 600, 800, 1000, 1200, and 1400 °C. Figure 19 shows the relationship between initial eruption temperature and mass partitioning for each simulation.

Both simulation sets #1 and #2 possess heightening trends where increases in eruption temperature shift particle emplacement toward the surface. This shift reflects two adjacent happenings. First, increases in temperature influence escalations in jet height, as shown in the results of Chapter 2. This increase in eruption jet height favors particle emplacement higher in the water column. This phenomenon is evidenced by the shift toward increased breaching mass at higher eruption temperatures in Set #2. Second, higher temperatures in the jet result in more heat transferred into seawater, which

decreases the bulk density of the column and generates stronger upwelling and more effective upward particle transport. Additionally, hotter and more buoyant radial plumes are likely less prone to incur downward mixing, increasing the retention of mass in the surface zone during outward spreading. These two features result in the general upward trend of Set #1. The 600 °C case exhibits mass partitioning that is dominated by a concentration at the seafloor due to the jet collapsing in the 300-200 m range.

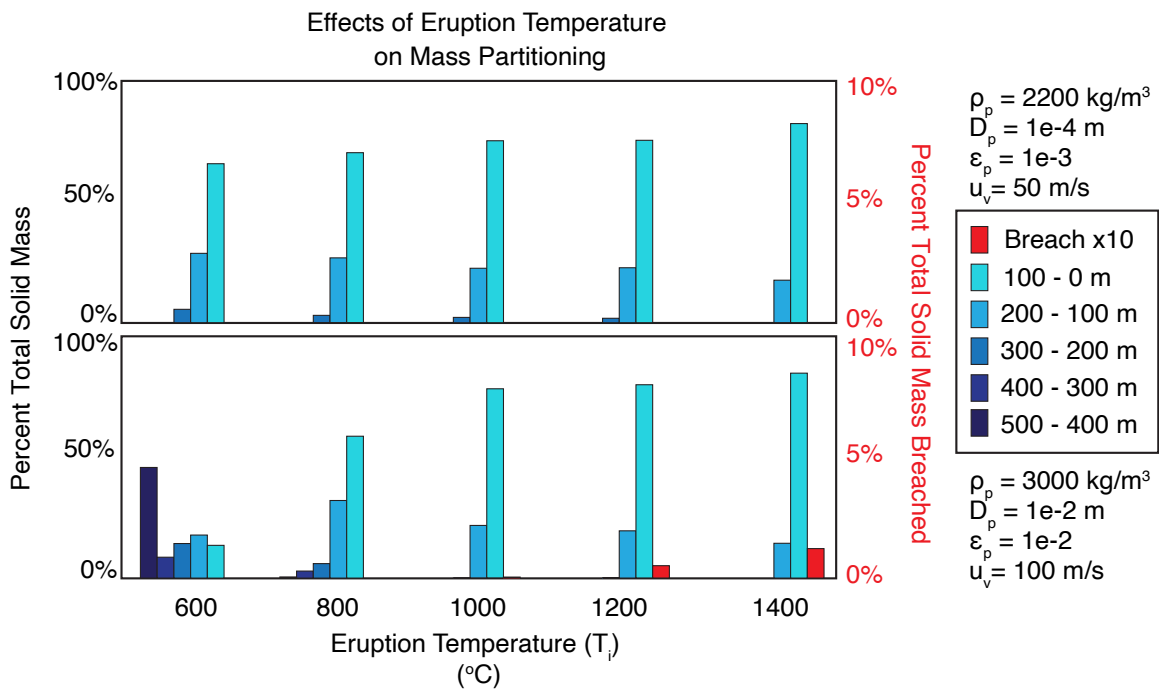


Figure 19. Effects of Eruption Temperature on Mass Partitioning. Bar graph depicting the percentage of the total erupted mass (y-axis) that arrives into each zone in the water column (colored bars) for a given eruption temperature (x-axis). The upper graph corresponds to particle parameter set #1, listed upper right, and the lower graph to particle parameter set #2, listed lower right. Note: breach mass percentage is show at 10x for clarity.

The 800 °C case shows a different collapse event and is the only simulation to show both partial collapse and surface breach in the same simulation. The nature of this

collapse is similar to the case that arrives to the surface, begins to spread, loses momentum, and begins settling in waves.

Particle Diameter

The particle diameter is an important component of particle transport, evidenced by its inclusion in the calculation of the particle Stokes number (Equation 15). The diameter influences fluid-particle drag and, along with solid density, contributes to how the particle behaves in a given flow. We present two sets of simulations each comprising runs with particle diameters of $1e-6$, $1e-5$, $1e-4$, $1e-3$, and $1e-2$ m. Figure 20 shows the relationship between particle diameter and mass partitioning for each simulation.

The effects of particle diameter in these simulations is fairly small with the exception of the largest particle diameter simulation. In simulation set #1, there is a trend of shifting mass emplacement from the 300-200 m and 200-100 m zones to the surface zone as particle diameter increase. Though, the $1e-2$ m simulation shows a substantial decrease in surface zone mass and a substantial increase in the concentration at 200-100 m. Simulation set #2 however, shows the opposite trend, with generally waning surface concentrations and reductions in breach mass with increasing particle diameter. Similarly to set #1, the transition from $1e-3$ to $1e-2$ m displays a sharper drop in surface concentration and breach mass.

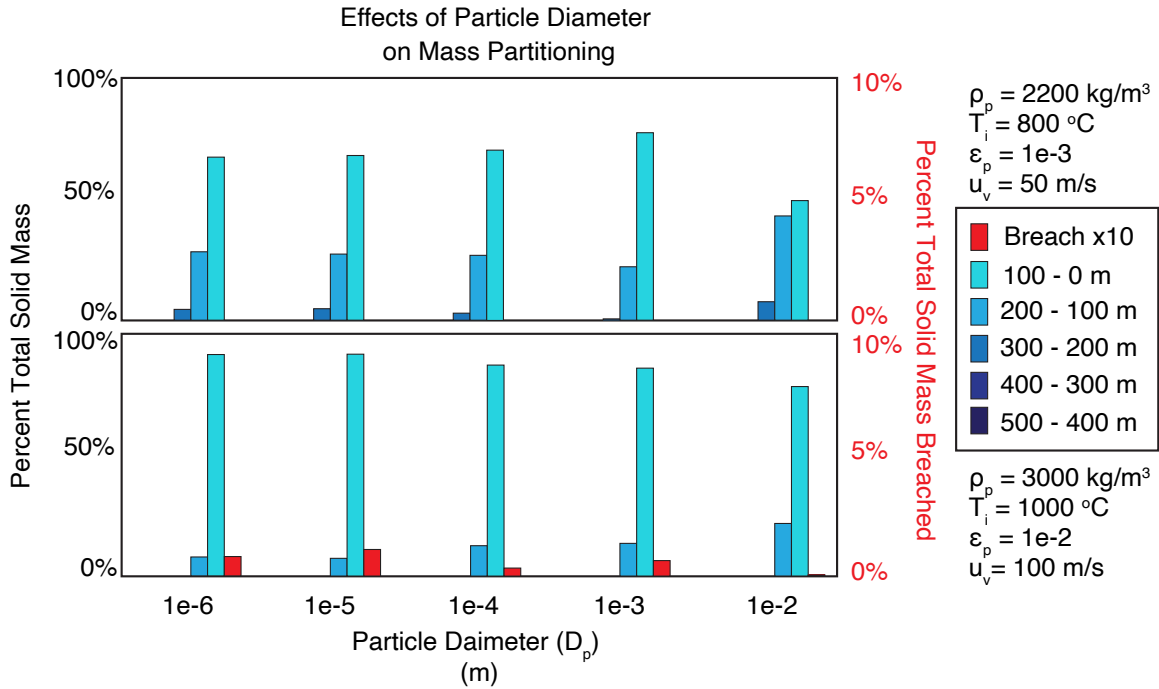


Figure 20. Effects of Particle Diameter on Mass Partitioning. Bar graph depicting the percentage of the total erupted mass (y-axis) that arrives into each zone in the water column (colored bars) for a given particle diameter (x-axis). The upper graph corresponds to particle parameter set #1, listed upper right, and the lower graph to particle parameter set #2, listed lower right. Note: breach mass percentage is show at 10x for clarity.

Solid Density

The solid density of the particles is another important criterion for particle transport and is also involved in the calculation of particle Stokes number. The density of a particle contributes to its ability to couple with a fluid and ultimately controls whether a particle will rise (lower density than fluid) or sink (higher density than fluid) in a steady fluid. We present two sets of simulations each comprising runs with solid densities of 600, 1040, 1200, 2200, and 3000 kg/m³. Figure 21 shows the relationship between solid density and mass partitioning for each simulation. Surprisingly, neither set #1 nor set #2 were significantly influenced by changes in solid density. For set #2, increasing density produced a small shift from the surface zone to the 100-200m zone, most pronounced at

the transition from positive buoyancy ($<1030\text{kg/m}^3$) to negative buoyancy ($>1030\text{kg/m}^3$).

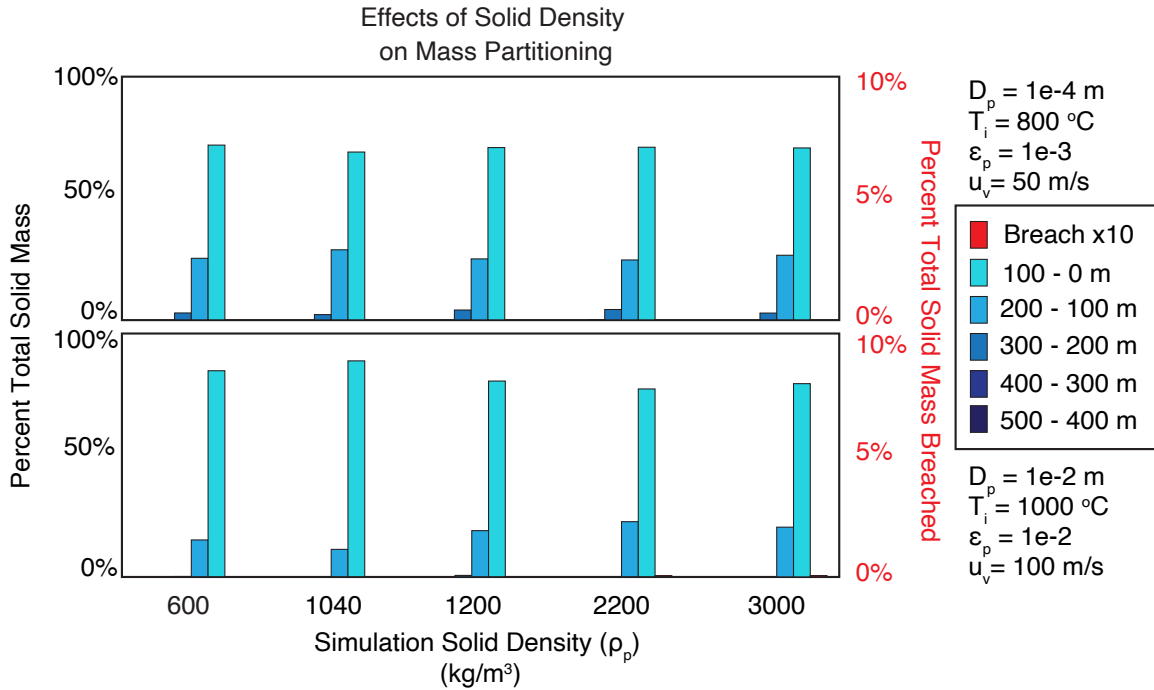


Figure 21. Effects of Solid Density on Mass Partitioning. Bar graph depicting the percentage of the total erupted mass (y-axis) that arrives into each zone in the water column (colored bars) for a given solid density (x-axis). The upper graph corresponds to particle parameter set #1, listed upper right, and the lower graph to particle parameter set #2, listed lower right. Note: breach mass percentage is show at 10x for clarity.

Comparing Partitioning in Explosive Jet Eruptions and Heat-Flux Equivalent Plumes

In an attempt to find characteristic patterns to distinguish explosive jet deposits from lofted plume deposits, we simulate a series of gas-less eruptions, essentially particle-laden hydrothermal plumes that possess the equivalent thermal flux as one of the jet simulations. For these plumes we assume an initial water temperature and calculate

the necessary eruption velocities to maintain thermal flux equivalence. The main significance in the results is that this process is highly dependent on initial conditions (i.e. the assumed water temperature) and a hydrothermal plume is highly capable of transporting solid particles. Plume transport is limited by the bulk density of the plume relative to the ambient water density. The fate of the plume is largely predetermined by the initial plume water density and particle Stokes number of the solids. If the plumes initial density is lower than that of the ambient water and the particles are well coupled to the flow, the plume will rise and transport the particles. If not, the plume will either rise and stall in the water column or flow outward, resembling a collapse phenomenon. Because of this, a test of the equivalent parameter set for gas-less eruptions does not adequately address plume transport. To better predict plume transport behavior a dedicated study is needed to assess source conditions to further narrow the limitations of water plume particle transport.

Discussion

The simulation results highlight the interplay between buoyancy, inertia, and condensation in regulating mass partitioning between the atmosphere, the sea surface, the water column, and the seafloor. These sections above have tried to isolate individual components to these eruptions, but the overall picture requires an assessment of their combination. The following discussion will highlight aspects of each parameter that warrant further consideration, followed by a general discussion on particle-laden eruption columns where we will utilize dynamic transport regimes to help define mass partitioning mechanisms identified in simulation.

Vent velocity

The 10 m/s example of set 1 is similar to that of a rising hydrothermal plume, where low inertia in the jet and rapid condensation inhibit plume wall shear, mixing, and entrainment of seawater. With no initial velocity fluctuations in the water column, the plumes that develop carry most particles to the surface and spread with little downward mixing. This process is highly dependent on particle stokes number and requires adequate fluid-particle coupling and lower particle concentrations to prevent collapse. In the set #2 10 m/s case the jet immediately collapses at the vent generating a near vent or fountaining phenomenon, where particle loading and lack of inertia and buoyancy limits transport into the upper column. At the set #2 50 m/s, we see a taller collapse phenomenon where higher relative momentum propels the jet above the vent, but the inertia is insufficient to reach the surface and collapses. Additionally, mixing and heating of water is not sufficient to loft collapsing particles in a heated water plume.

Particle concentration

In set #1, the shift from high concentrations in the surface and 100-200 m zones concentrations to a broader dispersal of particles amongst the zones is directly linked to particle loading. The bulk density in the $1e-2$ volume fraction case is too high, so even though the column possesses elevated initial inertia from higher bulk density, once the inertia is expended, the column must either collapse or shed particles, depending on the state of particle-flow coupling and particle clustering. In set #2, the $1e-2$ volume fraction particle does not exhibit similar behavior owing to the increased inertia in the jet from

higher density particles. For both sets #1 and #2, the 1e-1 cases possess substantial momentum from high solids concentration that contributes to full jet breaches and carries >17% and >40% of the erupted particle mass into the atmosphere, respectively (as highlighted in Figure 18). While an eruption with 10% volume fraction of particles is high, it represents the importance of particle concentration on the inertial state of the eruption.

Eruption Temperature

Increases in eruption temperature generally are stabilizing for an eruption jet by reducing the condensation rate in the jet. This stabilization generally enhances upward mobility of solid mass transport in the column. This is highlighted in the transition from fountaining/collapse of eruptions nearer the saturation temperature (i.e. 264 °C at 500 m water depth) to breaching above 1000 °C and evidenced by changes in maximum jet height above the vent from 220 m to 430 m in these simulations. The relatively small changes from 1000-1400 °C exhibit a relationship defined in Chapter 2, where the effect of increasing eruption temperature on jet height is reduced at higher temperatures.

Particle Diameter

The downward mixing trend in set #2 is easily explained by the increasing Stokes particle number with increasing particle diameter, which as the value increases from 1 increasingly favors detrainment from the flow. Conversely, the reduced downward mixing with increasing diameter trend in set #1 is less straightforward.

Solids Density

The lack of signature from substantial density changes is quite interesting. The trend in set #2, and similar trends in other plume forming eruptions, is likely due to decreased flow-coupling with denser particles which detrain from a plume and settling downward from the surface. Set #1, however, shows fairly steady behavior across all runs. This signifies that the solids density is less significant to the flow dynamics in these simulations than other parameters. For another parameter set closer to some dynamic threshold, a signature from particle density would undoubtedly be stronger. This does however show that substantial changes in solids density can be dynamically “overwhelmed” in subaqueous eruption conditions. It is important to note that though mass partitioning in these cases does not appear to depend on density, density is critical to the ensuing particle transport and settling.

Dynamic Regimes Control Mass Partitioning

From assessment of the simulation results it is clear that five regimes arise that primarily define particle transport and mass partitioning. These regimes from least to most inertia-dominated are fountaining, mid-column collapse, rise and settle partial collapse, roll-sheet partial collapse, and surface plume, shown in Figure 22. A brief description and key features of each regime follows.

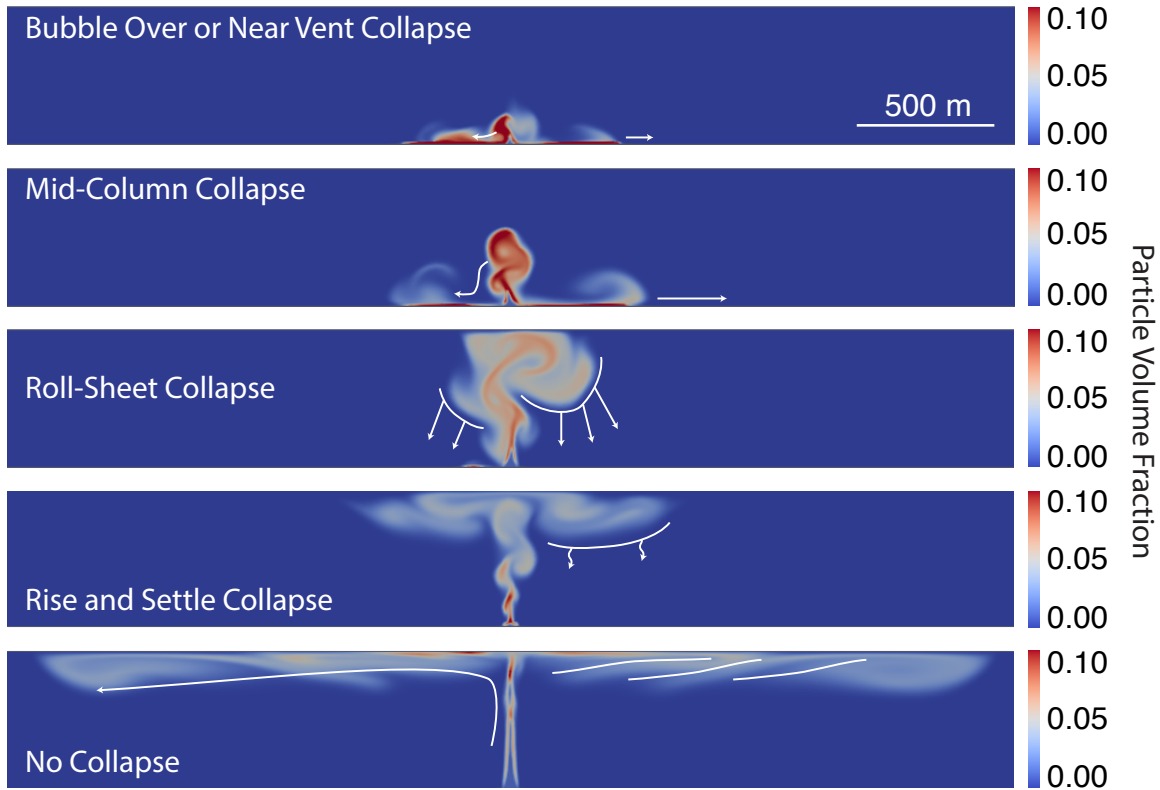


Figure 22. Eruption Column Transport Regimes. Five panels show simulations representing the five eruption column transport regimes outlined in the discussion. Each panel depicts the entire vertical extent but only a portion of the horizontal domain, cropped for space and clarity. Each still above represents a different simulation, after varying simulation times, as some features develop more rapidly than others. White arrows are included to highlight key dynamic features in each regime.

Collapse: Fountaining

Fountaining is the lowest inertia regime that occurs when eruption velocity and temperature is sufficiently low which limits mixing with seawater to prevent buoyant plume development. Additionally, fountaining requires particles with sufficiently high Stokes numbers to prevent buoyant lofting if/when a plume is initiated. Fountaining has a minimal to no eruption jet which contributes to the majority of the erupted mass staying near the vent. Here we define a threshold to differentiate fountaining, where the column collapse height must be below 100 m, changing to a mid-column collapse above this.

While the 100 m threshold is suited for comparison of our simulations, this height may need to be more precisely determined in future studies. Small, low energy density currents frequently develop as the collapsing jet transfers downward momentum into outwardly spreading currents. If it is possible for a subaqueous pyroclastic density current to be gas-supported, it would occur in this regime as the near vent collapse may trap and insulate gas to prevent rapid condensation. Additionally, high particle concentration in these flows could potentially boil small amounts of water in shallow enough water. Detailed analysis either via experiments or a dedicated numerical model need to be undertaken to address the possibility of gas-supported subaqueous pyroclastic density currents.

Collapse: Mid-column

The mid-column collapse regime is similar to fountaining, though here the inertial state of the eruption jet is great enough to transport the bulk of the erupted mass well above the vent (>100 m) before collapse. While this may seem an unnecessary split, eruptions that reach these heights before collapsing will partition greater masses of volcanic material to the mid-column zones. Mid-column collapses will therefore have substantially different deposits than those in the fountaining regime, as seafloor currents and mid-column currents are often different. Mid-column collapsing eruptions also tend to generate larger and faster density currents than fountaining eruptions since the collapse occurs higher than fountaining and yet has undergone fairly minimal mixing and entrainment.

Partial Collapse: Unroll-Sheet

The unroll-sheet partial collapse (US) regime is characterized by a jet or plume that possesses enough upward momentum to arrive to or near the surface, though instead of developing into a radial plume, the particles concentrate at the edge of the large eddies developing at the top of the jet and, as they overturn (or unroll), they collapse down through the water column in high-concentration sheets. This migration and collection of particles near the bottom of the eddy is similar to the stability factor-dependent process described in Burgisser & Bergantz, (2002). The depositional rate of this collapse process is significantly faster than the settling rate of individual particles. US regime eruptions have a signature larger concentration of particles at the seafloor zone, as well as significant mass partitioning in the mid-column and upper column zones, due to the rapid downward transport of the falling sheets. Collapse associated with this regime can also generate density currents though they tend to be much more dilute and slower than density currents generated by other regimes.

Partial Collapse: Rise and Settle

The rise and settle partial collapse (RS) regime describes eruption columns that rise to the surface and begin to spread out as surface plumes. As these flows begin to spread, they rapidly lose momentum and begin to settle down through the water column in waves. The depositional rate of these waves is much slower than in US. RS occurs when a buoyancy-driven particle-laden plume has little inertia as it arrives at the surface. Individual pulses from jet oscillations or particle clusters form individual radial currents. As a current loses its inertia, it begins to stagnate and slowly settle. This initiates a

settling wave. As subsequent flows spread outward, they push the earlier waves further downward. Thus, deposition is not as fast as US, but faster than individual particle settling as the waves are pushed downward and warrants individual regime consideration. Density currents are not generated by this type of collapse.

No Collapse: Surface Plume and Breach

The last regime is the surface plume where a sufficiently energetic jet or plume arrives to the surface and spreads radially with enough momentum to clearly define itself from the rising plume. The rate and extent of transport is highly variable and dependent on the conditions of the plume or jet supplying it. This regime can be accompanied by surface breaches of both gas and particles which can potentially feed atmospheric plumes and base surges. The depth of a surface plume is dictated by the energy of the flow, the bulk density of the flow, as well as the degree of flow-particle coupling. Plumes will mix with seawater and extend downward as they travel further. Instabilities and particle clustering can generate accelerated particle detrainment and travel as falling high particle concentration plumes. Generally, surface plumes are responsible for the furthest transport of mass from the eruption source, including ash-laden plumes and pumice rafts.

Regime Diagram

By plotting the simulations by regime in mass eruption rate (MER) and stability factor (S_T/F_R^2) space we can identify regime boundaries with only minor overlap (Figure 23). This overlap can also be justified in the appearance of transitional simulations we have identified, such as partial collapses that also breach, and no-collapse events that

possess vertically stacking radial surface plumes similar to rise and settle regime behavior. We do not include the fountaining regime simulations in this diagram as they significantly overlap the partial collapse and no collapse regimes and are strongly influenced by additional factors not accounted for in this regime space. We have separated jet breach phenomena from smaller breaches as they represent significantly larger and more violent breaches and, though few in simulation examples, cluster tightly.

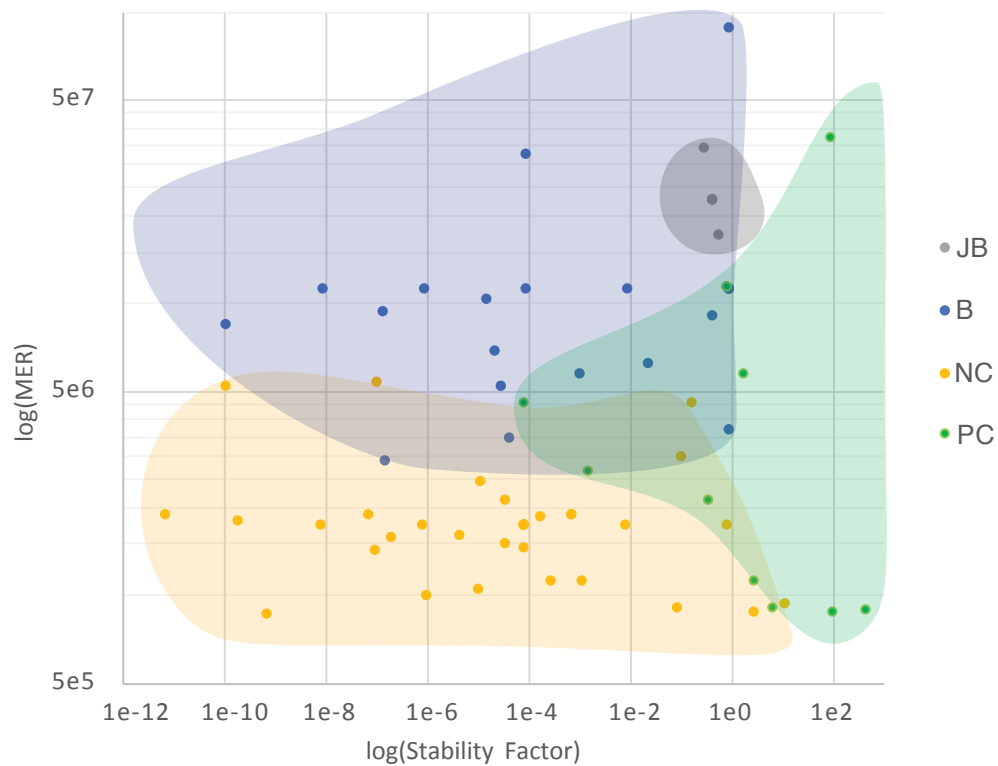


Figure 23. Regime diagram show simulation results as non-collapse (NC), partial collapse (PC), breach (B), and Jet Breach (JB) regimes in mass eruption rate (MER)-stability factor space. Each dot represents one individual simulation. An envelope is drawn around the regime populations to show extent and coverage. Overlapping regime space highlights the nature of transitional conditions.

This diagram illustrates that the transition from no collapse to partial collapse is driven by increases in the stability factor, denoting the migration of particles toward outer edges of circulating eddies. This edge-clustering favors sheet and wave development and decoupling from the flow. Additionally, increases in MER drive the growth in breaching potential, while there may also be a correlation with increasing stability factor, as evidenced by the clustering of jet breach cases. Further investigations are needed to precisely define the boundaries of the (steam) breach (blue) and jet breach (grey) regions.

Conclusions

We present a new look at subaqueous explosive eruptions with an emphasis on mass partitioning in the water column. Mass partitioning is tracked for a set of multiphase simulations to assess the contribution of vent velocity, eruption temperature, particle concentration, particle size, and solid density to transport dynamics. We highlight significant contributions from each of these parameters to the emplacement of two different particle populations. Finally, we identify five distinct subaqueous eruption column transport regimes in the model results that can be applied to the characterization of past and future eruption deposits.

These model results represent one of the first opportunities to assess particle transport mechanisms from a range of eruption conditions, especially those that are not either small eruptions or initiated at shallow water depths, which constitute most of our eruption observations. Further work is needed to constrain the influence of background currents, or even an unsteady background initial condition, on eruption jet and plume dynamics. While the effects of wind on subaerial plumes has been studied (Aubry et al.,

2017; Degruyter & Bonadonna, 2013), subaqueous conditions likely produce significantly different results, as we have seen in many aspects of subaqueous volcanology. Additionally, this work would benefit from expansion to shallower water depths to capture eruption through crater lakes and other sublacustrine environments. Our current utilization of a fixed upper boundary condition needs to be modified for accurate consideration of water surface effects, which are more significant in shallower water depths. Many aspects of underwater explosive eruptions involve a pulsating, oscillating, or generally unsteady eruption jet. Further evaluation of unsteady eruption conditions is necessary to capture these phenomena, especially in shallow water eruptions. All of these extensions are possible with the model utilized in this study.

CHAPTER IV

CONCLUSION AND FUTURE DIRECTIONS

Subaqueous eruption jets have a strong influence on the volcanic hazards and deposits produced during an eruption. While subaerial eruption jets and columns are fairly well studied, the impact of hydrous phase change in subaqueous eruptions prevents the direct comparison of the two. The dearth of direct observations and measurements of subaqueous eruptions deeper than 10s of meters has limited our ability to connect eruption processes to eruption deposits. With the limits of experimentation and the difficulty in modeling multiphase immiscible fluid systems like a subaqueous eruption, most advances have come from the direct study of deposits and pyroclasts. Numerical modeling is needed to help define the processes and limits that may not be captured within samples and deposits, like the role of hydrous phase change in jet dynamics and particle dispersal. In this dissertation, we have presented a new numerical model capable of identifying and quantifying subaqueous eruption processes. Because our observations of underwater eruptions are so few, these models deliver a first look at many of these eruption processes in action.

The numerical models developed in this study seek to capture the dynamics of subaqueous eruption dynamics, from large scale turbulent eddies and eruption jets, to sub-grid hydrous phase change. In Chapter 2 we present a model for subaqueous explosive eruptions and use it to constrain the eruption conditions that primarily influence

eruption jet behavior and the possibility of a surface breach. An abbreviated summary of the results of Chapter 2 are below:

- Mass flux, eruption temperature, and water depth are the dominant eruption parameters that govern eruption jet height. Mass flux is the primary control, but eruption temperature is also significant, with increasing influence as the eruption temperature approaches the water saturation temperature.
- Subaqueous eruptions can breach the surface, ranging from small bubbles at the surface to full jet breach, in water depths as great as 500 m, but cannot in depths of 1000 m, for the collection of conditions tested. Though, full jet breach at 500 m is unlikely when compared to shallower depths.
- Explosive eruptions can generate evidence of subsurface eruptions, even when breaches are not possible, including sea surface temperature anomalies and ocean surface displacements.

The determination of mass flux, water depth, and eruption temperature as the key influences of steam jet dynamics helps us to anticipate eruption behavior for specific volcanic edifices using information from geothermometry, bathymetry, and past eruption deposits. The limits established for eruption breaches and eruption jet heights allows us to better assess potential hazards in submarine eruptions. With the development of this model, and a better understanding of the relationship between condensation and steam jet dynamics, we endeavor to explore the impact gas jets have on tephra emplacement in the water column during subaqueous eruptions. The goal of chapter 3 is to establish a

relationship between eruption conditions and mass partitioning. The key results are recapped below:

- The influence of eruption velocity, particle concentration, eruption temperature, particle size, and solid density on mass partitioning is determined for two different parameter sets.
- We compare mass partitioning results for explosive jets with equivalent gas-less eruptions to evaluate endmember transport scenarios and the mass partitioning.
- Five eruption column transport regimes are identified with unique mass partitioning signatures.
- Surface breaching particle mass is quantified for different eruption parameters.

In conclusion, this study has emphasized through multiphase models with subgrid hydrous phase change that jet dynamics and condensation are critical to understanding explosive subaqueous eruptions, that surface breaching eruptions can be quantified for specific eruptions, and mass partitioning in the water column is highly dependent on the eruption conditions and the transport regime.

While we are confident in our models and the results, they are limited by a few assumptions and simplifications. First, the eruptions occur into a steady water domain. Initial fluctuations may decrease the stability of the jets. Second, turbulence models that account for subgrid effects of turbulence production and dissipation associated with a dispersed phase have not been explored in this implementation. Further validation and

analysis of mixing may reveal other subgrid turbulence models (e.g. dynamic LES) that better capture aspects of this problem. However, the validation we have conducted indicates that mixing is reasonably reproduced for moderate Reynolds number conditions. Lastly, the fixed upper boundary condition used in all models does not account for the actual deflection and deformation of the water surface and the production of breaking waves, which has effects on mixing, plume transport, and energy dissipation at the surface.

While we have addressed some of the fundamentals of subaqueous explosive eruptions, more have been uncovered that can be addressed utilizing the model developed in the study:

- *How do cross currents affect jet stability and particle transport? How can we integrate the results from chapter 3 with current velocity data to anticipate long-range tephra dispersal?*
- *How do shallow eruptions differ from the 500m water depth eruptions assessed in chapter 3? How are shallow eruptions in sub-lacustrine conditions affected by jet mixing and hydrous phase change? What is the impact for potential eruptions through the crater lake at a volcano like Kilauea or Taal?*
- *We evaluated relatively fine particles utilizing eulerian-eulerian methods? Can we implement Lagrangian phases to investigate jet and plumes influences on pumice raft development?*

- *Can we utilize pressure probes in the model to compare to hydroacoustic data of subaqueous eruptions? Can we use the model to help interpret hydroacoustic data?*

The future direction of this work is to explore some of these ideas above. But first, I aim to address some of the current limitations of the model, including those listed above (dynamic upper BC, updated turbulence model, and noisy initial conditions). I plan to expand this model to work in 3D to better capture mixing and turbulence, as precisely as possible. Additionally, the entrainment of water in the jet needs to be better validated against experimental results. A USGS post-doc proposal has recently been funded to address all of these model tests and augmentations with the goal of assessing the hazards and processes associated with eruption in/through the crater lake that has recently appeared in the Halema'uma'u Crater on Kilauea, Hawaii.

While this model represents an exciting new look into eruption processes, a concerted effort needs to be undertaken to increase the accessibility of subaqueous volcano eruptions. The science will forever be limited until we have a larger number of observations to compare to deposits and samples. For this, we need to develop a robust eruption indication and location system and a rapid response system to investigate, deploy sensors, and take surface and subsurface samples and measurements.

REFERENCES CITED

- Adcroft, A., Dutkiewicz, S., Ferreira, D., Heimbach, P., Jahn, O., & Maze, G. (2011). MITgcm User Manual. *Internal Document*.
- Allen, S. R., Fiske, R. S., & Cashman, K. V. (2008). Quenching of steam-charged pumice: Implications for submarine pyroclastic volcanism. *Earth and Planetary Science Letters*, 274(1–2), 40–49. <https://doi.org/10.1016/j.epsl.2008.06.050>
- Allen, S. R., & McPhie, J. (2000). Water-settling and resedimentation of submarine rhyolitic pumice at Yali, eastern Aegean, Greece. *Journal of Volcanology and Geothermal Research*, 95(1–4), 285–307. [https://doi.org/10.1016/S0377-0273\(99\)00127-4](https://doi.org/10.1016/S0377-0273(99)00127-4)
- Allen, Sharon R., Fiske, R. S., & Tamura, Y. (2010). Effects of water depth on pumice formation in submarine domes at Sumisu, Izu-Bonin arc, western Pacific. *Geology*, 38(5), 391–394. <https://doi.org/10.1130/G30500.1>
- Allen, Sharon R., & Freundt, A. (2006). Resedimentation of cold pumiceous ignimbrite into water: Facies transformations simulated in flume experiments. *Sedimentology*, 53(4), 717–734. <https://doi.org/10.1111/j.1365-3091.2006.00790.x>
- Allen, Sharon R., & McPhie, J. (2009). Products of neptunian eruptions. *Geology*, 37(7), 639–642. <https://doi.org/10.1130/G30007A.1>
- Andrews, B. J., & Gardner, J. E. (2009). Turbulent dynamics of the 18 May 1980 Mount St. Helens eruption column. *Geology*, 37(10), 895–898. <https://doi.org/10.1130/G30168A.1>
- Aubry, T. J., Jellinek, A. M., Carazzo, G., Gallo, R., Hatcher, K., & Dunning, J. (2017). A new analytical scaling for turbulent wind-bent plumes: Comparison of scaling laws with analog experiments and a new database of eruptive conditions for predicting the height of volcanic plumes. *Journal of Volcanology and Geothermal Research*. <https://doi.org/10.1016/j.jvolgeores.2017.07.006>
- Aya, I., & Nariai, H. (1991). Evaluation of heat-transfer coefficient at direct-contact condensation of cold water and steam. *Nuclear Engineering and Design*, 131(1), 17–24. [https://doi.org/10.1016/0029-5493\(91\)90314-8](https://doi.org/10.1016/0029-5493(91)90314-8)
- Baker, E. T., Massoth, G. J., de Ronde, C. E. J., Lupton, J. E., & McInnes, B. I. A. (2002). Observations and sampling of an ongoing subsurface eruption of Kavachi volcano, Solomon Islands, May 2000. *Geology*. [https://doi.org/10.1130/0091-7613\(2002\)030<0975:OASOAO>2.0.CO;2](https://doi.org/10.1130/0091-7613(2002)030<0975:OASOAO>2.0.CO;2)

- Barreyre, T., Soule, S. A., & Sohn, R. A. (2011). Dispersal of volcaniclasts during deep-sea eruptions: Settling velocities and entrainment in buoyant seawater plumes. *Journal of Volcanology and Geothermal Research*, 205(3–4), 84–93. <https://doi.org/10.1016/j.jvolgeores.2011.05.006>
- Batiza, R., Fornari, D. J., Vanko, D. A., & Lonsdale, P. (1984). Craters, calderas, and hyaloclastites on young Pacific seamounts. *Journal of Geophysical Research*. <https://doi.org/10.1029/JB089iB10p08371>
- Benage, M. C., Dufek, J., Degruyter, W., Geist, D., Harpp, K., & Rader, E. (2014). Tying textures of breadcrust bombs to their transport regime and cooling history. *Journal of Volcanology and Geothermal Research*, 274, 92–107. <https://doi.org/10.1016/j.jvolgeores.2014.02.005>
- Bercovici, D., & Michaut, C. (2010). Two-phase dynamics of volcanic eruptions: Compaction, compression and the conditions for choking. *Geophysical Journal International*, 182(2), 843–864. <https://doi.org/10.1111/j.1365-246X.2010.04674.x>
- Breard, E. C. P., Dufek, J., & Lube, G. (2018). Enhanced Mobility in Concentrated Pyroclastic Density Currents: An Examination of a Self-Fluidization Mechanism. *Geophysical Research Letters*. <https://doi.org/10.1002/2017GL075759>
- Bryan, S. E., Cook, A., Evans, J. P., Colls, P. W., Wells, M. G., Lawrence, M. G., Jell, J. S., Greig, A., & Leslie, R. (2004). Pumice rafting and faunal dispersion during 2001-2002 in the Southwest Pacific: Record of a dacitic submarine explosive eruption from Tonga. *Earth and Planetary Science Letters*. <https://doi.org/10.1016/j.epsl.2004.08.009>
- Bryan, S. E., Cook, A. G., Evans, J. P., Hebden, K., Hurrey, L., Colls, P., Jell, J. S., Weatherley, D., & Fern, J. (2012). Rapid, long-distance dispersal by pumice rafting. *PLoS ONE*. <https://doi.org/10.1371/journal.pone.0040583>
- Burgisser, A., & Bergantz, G. W. (2002). Reconciling pyroclastic flow and surge: The multiphase physics of pyroclastic density currents. *Earth and Planetary Science Letters*, 202(2), 405–418. [https://doi.org/10.1016/S0012-821X\(02\)00789-6](https://doi.org/10.1016/S0012-821X(02)00789-6)
- Busby, C. (2005). Possible distinguishing characteristics of very deepwater explosive and effusive silicic volcanism. *Geology*, 33(11), 845–848. <https://doi.org/10.1130/G21216.1>
- Carazzo, G., Kaminski, E., & Tait, S. (2008). On the rise of turbulent plumes: Quantitative effects of variable entrainment for submarine hydrothermal vents, terrestrial and extra terrestrial explosive volcanism. *Journal of Geophysical Research: Solid Earth*, 113(9), 1–19. <https://doi.org/10.1029/2007JB005458>

- Carey, R., Adam Soule, S., Manga, M., White, J. D. L., McPhie, J., Wysoczanski, R., Jutzeler, M., Tani, K., Yoerger, D., Fornari, D., Caratori-Tontini, F., Houghton, B., Mitchell, S., Ikegami, F., Conway, C., Murch, A., Fauria, K., Jones, M., Cahalan, R., & McKenzie, W. (2018a). The largest deep-ocean silicic volcanic eruption of the past century. *Science Advances*, 4(1). <https://doi.org/10.1126/sciadv.1701121>
- Carey, R., Adam Soule, S., Manga, M., White, J. D. L., McPhie, J., Wysoczanski, R., Jutzeler, M., Tani, K., Yoerger, D., Fornari, D., Caratori-Tontini, F., Houghton, B., Mitchell, S., Ikegami, F., Conway, C., Murch, A., Fauria, K., Jones, M., Cahalan, R., & McKenzie, W. (2018b). The largest deep-ocean silicic volcanic eruption of the past century. *Science Advances*. <https://doi.org/10.1126/sciadv.1701121>
- Carey, S. N., Sigurdsson, H., & Sparks, R. S. J. (1988). Experimental studies of particle-laden plumes. *Journal of Geophysical Research*. <https://doi.org/10.1029/jb093ib12p15314>
- Carey, S., & Sparks, R. S. J. (1986). Quantitative models of the fallout and dispersal of tephra from volcanic eruption columns. *Bulletin of Volcanology*, 48(2–3), 109–125. <https://doi.org/10.1007/BF01046546>
- Carracedo, J. C., Torrado, F. P., González, A. R., Soler, V., Turiel, J. L. F., Troll, V. R., & Wiesmaier, S. (2012). The 2011 submarine volcanic eruption in El Hierro (Canary Islands). *Geology Today*, 28(2), 53–58. <https://doi.org/10.1111/j.1365-2451.2012.00827.x>
- Cas, R. A. F., & Giordano, G. (2014). Submarine volcanism: A review of the constraints, processes and products, and relevance to the Cabo de Gata volcanic succession. In *Italian Journal of Geosciences*. <https://doi.org/10.3301/IJG.2014.46>
- Cas, R. A. F., & Simmons, J. M. (2018). Why deep-water eruptions are so different from subaerial eruptions. *Frontiers in Earth Science*. <https://doi.org/10.3389/feart.2018.00198>
- Cas, R. A., & Wright, J. V. (1991). Subaqueous pyroclastic flows and ignimbrites: an assessment. *Bulletin of Volcanology*, 53(5), 357–380. <https://doi.org/10.1007/BF00280227>
- Cas, R. a F., Allen, R. L., Bull, S. W., Clifford, B. a, & Wright, J. V. (1990). Subaqueous, rhyolitic dome-top tuff cones: a model based on the Devonian Bunga Beds, southeastern Australia and a modern analogue. *Geology*, 52(3), 159–174.
- Casas, D., Pimentel, A., Pacheco, J., Martorelli, E., Sposato, A., Ercilla, G., Alonso, B., & Chiocci, F. (2018). Serreta 1998–2001 submarine volcanic eruption, offshore Terceira (Azores): Characterization of the vent and inferences about the eruptive dynamics. *Journal of Volcanology and Geothermal Research*, 356, 127–140. <https://doi.org/10.1016/j.jvolgeores.2018.02.017>

- Cashman, K. V., & Fiske, R. S. (1991). Fallout of pyroclastic debris from submarine volcanic eruptions. *Science*. <https://doi.org/10.1126/science.253.5017.275>
- Chadwick, W. W., Cashman, K. V., Embley, R. W., Matsumoto, H., Dziak, R. P., de Ronde, C. E. J., Lau, T. K., Deardorff, N. D., & Merle, S. G. (2008). Direct video and hydrophone observations of submarine explosive eruptions at NW Rota-1 volcano, Mariana arc. *Journal of Geophysical Research: Solid Earth*, *113*(8), 1–23. <https://doi.org/10.1029/2007JB005215>
- Chen, C., Beardsley, R. C., & Cowles, G. (2006). An unstructured-grid, finite-volume coastal ocean model (FVCOM) system. *Oceanography*. <https://doi.org/10.5670/oceanog.2006.92>
- Chojnicki, K. N., Clarke, A. B., Phillips, J. C., & Adrian, R. J. (2015). Rise dynamics of unsteady laboratory jets with implications for volcanic plumes. *Earth and Planetary Science Letters*, *412*, 186–196. <https://doi.org/10.1016/j.epsl.2014.11.046>
- Chun, M. H., Kim, Y. S., & Park, J. W. (1996). An investigation of direct condensation of steam jet in subcooled water. *International Communications in Heat and Mass Transfer*. [https://doi.org/10.1016/0735-1933\(96\)00077-2](https://doi.org/10.1016/0735-1933(96)00077-2)
- Clarke, A. B., Neri, A., Voight, B., Macedonio, G., & Druitt, T. H. (2002). Computational modelling of the transient dynamics of the August 1997 Vulcanian explosions at Soufrière Hills Volcano, Montserrat: influence of initial conduit conditions on near-vent pyroclastic dispersal. *Geological Society Memoir*, *21*(1), 319–348. <https://doi.org/10.1144/GSL.MEM.2002.021.01.15>
- Colombier, M., Scheu, B., Wadsworth, F. B., Cronin, S., Vasseur, J., Dobson, K. J., Hess, K. U., Tost, M., Yilmaz, T. I., Cimarelli, C., Brenna, M., Ruthensteiner, B., & Dingwell, D. B. (2018). Vesiculation and Quenching During Surtseyan Eruptions at Hunga Tonga-Hunga Ha’apai Volcano, Tonga. *Journal of Geophysical Research: Solid Earth*, *123*(5), 3762–3779. <https://doi.org/10.1029/2017JB015357>
- Coombs, M., Wallace, K., Cameron, C., Lyons, J., Wech, A., Angeli, K., & Cervelli, P. (2019). Overview, chronology, and impacts of the 2016–2017 eruption of Bogoslof volcano, Alaska. *Bulletin of Volcanology*, *81*(11). <https://doi.org/10.1007/s00445-019-1322-9>
- Costa, A., Suzuki, Y. J., & Koyaguchi, T. (2018). Understanding the plume dynamics of explosive super-eruptions. *Nature Communications*, *9*(1). <https://doi.org/10.1038/s41467-018-02901-0>

- Dartevelle, S., Rose, W. I., Stix, J., Kelfoun, K., & Vallance, J. W. (2004). Numerical modeling of geophysical granular flows: 2. Computer simulations of plinian clouds and pyroclastic flows and surges. *Geochemistry, Geophysics, Geosystems*, 5(8). <https://doi.org/10.1029/2003GC000637>
- Deardorff, N. D., Cashman, K. V., & Chadwick, W. W. (2011a). Observations of eruptive plume dynamics and pyroclastic deposits from submarine explosive eruptions at NW Rota-1, Mariana arc. *Journal of Volcanology and Geothermal Research*, 202(1–2), 47–59. <https://doi.org/10.1016/j.jvolgeores.2011.01.003>
- Deardorff, N. D., Cashman, K. V., & Chadwick, W. W. (2011b). Observations of eruptive plume dynamics and pyroclastic deposits from submarine explosive eruptions at NW Rota-1, Mariana arc. *Journal of Volcanology and Geothermal Research*, 202(1–2), 47–59. <https://doi.org/10.1016/j.jvolgeores.2011.01.003>
- Degruyter, W., & Bonadonna, C. (2013). Impact of wind on the condition for column collapse of volcanic plumes. *Earth and Planetary Science Letters*. <https://doi.org/10.1016/j.epsl.2013.06.041>
- Di Muro, A., Rosi, M., Aguilera, E., Barbieri, R., Massa, G., Mundula, F., & Pieri, F. (2008). Transport and sedimentation dynamics of transitional explosive eruption columns: The example of the 800 BP Quilotoa plinian eruption (Ecuador). *Journal of Volcanology and Geothermal Research*, 174(4), 307–324. <https://doi.org/10.1016/j.jvolgeores.2008.03.002>
- Dobran, F. (1992). Nonequilibrium flow in volcanic conduits and application to the eruptions of Mt. St. Helens on May 18, 1980, and Vesuvius in AD 79. *Journal of Volcanology and Geothermal Research*. [https://doi.org/10.1016/0377-0273\(92\)90019-A](https://doi.org/10.1016/0377-0273(92)90019-A)
- Dondin, F., Lebrun, J. F., Kelfoun, K., Fournier, N., & Randrianasolo, A. (2012). Sector collapse at Kick 'em Jenny submarine volcano (Lesser Antilles): Numerical simulation and landslide behaviour. *Bulletin of Volcanology*, 74(2), 595–607. <https://doi.org/10.1007/s00445-011-0554-0>
- Dufek, J., & Bergantz, G. W. (2007). Suspended load and bed-load transport of particle-laden gravity currents: The role of particle-bed interaction. *Theoretical and Computational Fluid Dynamics*. <https://doi.org/10.1007/s00162-007-0041-6>
- Dufek, J., Manga, M., & Staedter, M. (2007). Littoral blasts: Pumice-water heat transfer and the conditions for steam explosions when pyroclastic flows enter the ocean. *Journal of Geophysical Research: Solid Earth*, 112(11), 1–16. <https://doi.org/10.1029/2006JB004910>

- Dufek, Josef, & Bergantz, G. W. (2007). Dynamics and deposits generated by the Kos Plateau Tuff eruption: Controls of basal particle loss on pyroclastic flow transport. *Geochemistry, Geophysics, Geosystems*, 8(12).
<https://doi.org/10.1029/2007GC001741>
- Dufek, Josef, Wexler, J., & Manga, M. (2009). Transport capacity of pyroclastic density currents: Experiments and models of substrate-flow interaction. *Journal of Geophysical Research: Solid Earth*, 114(11), 1–13.
<https://doi.org/10.1029/2008JB006216>
- Dürig, T., White, J. D. L., Murch, A. P., Zimanowski, B., Büttner, R., Mele, D., Dellino, P., Carey, R. J., Schmidt, L. S., & Spitznagel, N. (2020). Deep-sea eruptions boosted by induced fuel–coolant explosions. *Nature Geoscience*.
<https://doi.org/10.1038/s41561-020-0603-4>
- Embley, R. W., Merle, S. G., Baker, E. T., Rubin, K. H., Lupton, J. E., Resing, J. A., Dziak, R. P., Lilley, M. D., Chadwick, W. W., Shank, T., Greene, R., Walker, S. L., Haxel, J., Olson, E., & Baumberger, T. (2014). Eruptive modes and hiatus of volcanism at West Mata seamount, NE Lau basin: 1996–2012. *Geochemistry, Geophysics, Geosystems*. <https://doi.org/10.1002/2014GC005387>
- Embley, R. W., & Rubin, K. H. (2018). Extensive young silicic volcanism produces large deep submarine lava flows in the NE Lau Basin. *Bulletin of Volcanology*.
<https://doi.org/10.1007/s00445-018-1211-7>
- Embley, R. W., Tamura, Y., Merle, S. G., Sato, T., Shizuka, O. I., Chadwick, W. W., Wiens, D. A., Shore, P., & Stern, R. J. (2014). Eruption of south Sarigan seamount, Northern Mariana Islands: Insights into hazards from submarine volcanic Eruptions. *Oceanography*, 27(2), 24–31. <https://doi.org/10.5670/oceanog.2014.37>
- Fauria, K. E., & Manga, M. (2018). Pyroclast cooling and saturation in water. *Journal of Volcanology and Geothermal Research*.
<https://doi.org/10.1016/j.jvolgeores.2018.07.002>
- Fauria, K. E., Manga, M., & Wei, Z. (2017). Trapped bubbles keep pumice afloat and gas diffusion makes pumice sink. *Earth and Planetary Science Letters*.
<https://doi.org/10.1016/j.epsl.2016.11.055>
- Fink, J. H., & Anderson, S. W. (2000). Lava Domes and Coulees. In *Encyclopedia of volcanoes*.
- Fiske, R. S., Cashman, K. V., Shibata, A., & Watanabe, K. (1998). Tephra dispersal from Myojinsho, Japan, during its shallow submarine eruption of 1952–1953. *Bulletin of Volcanology*, 59(4), 262–275. <https://doi.org/10.1007/s004450050190>

- Fiske, R. S., & Matsuda, T. (1964). Submarine equivalents of ash flows in the Tokiwa Formation, Japan. In *American Journal of Science* (Vol. 262, Issue 1, pp. 76–106). <https://doi.org/10.2475/ajs.262.1.76>
- Fiske, R. S., Naka, J., Iizasa, K., Yuasa, M., & Klaus, A. (2001). Submarine silicic caldera at the front of the Izu-Bonin arc, Japan: Voluminous seafloor eruptions of rhyolite pumice. *Bulletin of the Geological Society of America*, 113(7), 813–824. [https://doi.org/10.1130/0016-7606\(2001\)113<0813:SSCATF>2.0.CO;2](https://doi.org/10.1130/0016-7606(2001)113<0813:SSCATF>2.0.CO;2)
- Fiske, Richard S. (1963). Subaqueous pyroclastic flows in the ohanapecosh formation, Washington. *Bulletin of the Geological Society of America*. [https://doi.org/10.1130/0016-7606\(1963\)74\[391:SPFITO\]2.0.CO;2](https://doi.org/10.1130/0016-7606(1963)74[391:SPFITO]2.0.CO;2)
- Fornari, D. J. (1986). Submarine lava tubes and channels. *Bulletin of Volcanology*. <https://doi.org/10.1007/BF01081757>
- Friedman, P. D., Meyer, W. J., & Carey, S. (2006). Experimental simulation of phase mingling in a subaqueous lava fountain. *Journal of Geophysical Research*, 111(B7), 1–14. <https://doi.org/10.1029/2005jb004162>
- Garvine, R. W. (1984). Radial spreading of buoyant, surface plumes in coastal waters (model). *Journal of Geophysical Research*. <https://doi.org/10.1029/JC089iC02p01989>
- Gilbert, J. S., & Sparks, R. S. J. (1998). The physics of explosive volcanic eruptions. *Geological Society Special Publication*, 145.
- Girault, F., Carazzo, G., Tait, S., Ferrucci, F., & Kaminski, É. (2014). The effect of total grain-size distribution on the dynamics of turbulent volcanic plumes. *Earth and Planetary Science Letters*, 394, 124–134. <https://doi.org/10.1016/j.epsl.2014.03.021>
- Green, D. N., Evers, L. G., Fee, D., Matoza, R. S., Snellen, M., Smets, P., & Simons, D. (2013). Hydroacoustic, infrasonic and seismic monitoring of the submarine eruptive activity and sub-aerial plume generation at South Sarigan, May 2010. *Journal of Volcanology and Geothermal Research*, 257, 31–43. <https://doi.org/10.1016/j.jvolgeores.2013.03.006>
- Guieu, C., Bonnet, S., Petrenko, A., Menkes, C., Chavagnac, V., Desboeufs, K., Maes, C., & Moutin, T. (2018). Iron from a submarine source impacts the productive layer of the Western Tropical South Pacific (WTSP). *Scientific Reports*. <https://doi.org/10.1038/s41598-018-27407-z>

- Hamme, R. C., Webley, P. W., Crawford, W. R., Whitney, F. A., Degrandpre, M. D., Emerson, S. R., Eriksen, C. C., Giesbrecht, K. E., Gower, J. F. R., Kavanaugh, M. T., Pea, M. A., Sabine, C. L., Batten, S. D., Coogan, L. A., Grundle, D. S., & Lockwood, D. (2010). Volcanic ash fuels anomalous plankton bloom in subarctic northeast Pacific. *Geophysical Research Letters*.
<https://doi.org/10.1029/2010GL044629>
- Head, J. W., & Wilson, L. (2003). Deep submarine pyroclastic eruptions: Theory and predicted landforms and deposits. *Journal of Volcanology and Geothermal Research*, 121(3–4), 155–193. [https://doi.org/10.1016/S0377-0273\(02\)00425-0](https://doi.org/10.1016/S0377-0273(02)00425-0)
- Hong, S. J., Park, G. C., Cho, S., & Song, C. H. (2012). Condensation dynamics of submerged steam jet in subcooled water. *International Journal of Multiphase Flow*, 39, 66–77. <https://doi.org/10.1016/j.ijmultiphaseflow.2011.10.007>
- Iezzi, G., Lanzafame, G., Mancini, L., Behrens, H., Tamburrino, S., Vallefucio, M., Passaro, S., Signanini, P., & Ventura, G. (2020). Deep sea explosive eruptions may be not so different from subaerial eruptions. *Scientific Reports*, 10(1).
<https://doi.org/10.1038/s41598-020-63737-7>
- Joseph, A. (2014). Vertical Profiling of Horizontal Currents Using Freely Sinking and Rising Probes. In *Measuring Ocean Currents*. <https://doi.org/10.1016/b978-0-12-415990-7.00010-7>
- Jutzeler, M., Marsh, R., Carey, R. J., White, J. D. L., Talling, P. J., & Karlstrom, L. (2014a). On the fate of pumice rafts formed during the 2012 Havre submarine eruption. *Nature Communications*, 5, 1–10. <https://doi.org/10.1038/ncomms4660>
- Jutzeler, M., Marsh, R., Carey, R. J., White, J. D. L., Talling, P. J., & Karlstrom, L. (2014b). On the fate of pumice rafts formed during the 2012 Havre submarine eruption. *Nature Communications*. <https://doi.org/10.1038/ncomms4660>
- Jutzeler, M., Marsh, R., van Sebille, E., Mittal, T., Carey, R. J., Fauria, K. E., Manga, M., & McPhie, J. (2020). Ongoing Dispersal of the 7 August 2019 Pumice Raft From the Tonga Arc in the Southwestern Pacific Ocean. *Geophysical Research Letters*, 47(5). <https://doi.org/10.1029/2019GL086768>
- Jutzeler, M., McPhie, J., & Allen, S. R. (2014). Submarine eruption-fed and resedimented pumice-rich facies: the Dogashima Formation (Izu Peninsula, Japan). *Bulletin of Volcanology*, 76(10). <https://doi.org/10.1007/s00445-014-0867-x>
- Kano, K., Yamamoto, T., & Ono, K. (1996). Subaqueous eruption and emplacement of the Shinjima Pumice, Shinjima (Moeshima) Island, Kagoshima Bay, SW Japan. *Journal of Volcanology and Geothermal Research*, 71(2–4), 187–206.
[https://doi.org/10.1016/0377-0273\(95\)00077-1](https://doi.org/10.1016/0377-0273(95)00077-1)

- Kelley, D. S., Baross, J. A., & Delaney, J. R. (2002). Volcanoes, fluids, and life at mid-ocean ridge spreading centers. *Annual Review of Earth and Planetary Sciences*.
<https://doi.org/10.1146/annurev.earth.30.091201.141331>
- Khan, A., Haq, N. U., Chughtai, I. R., Shah, A., & Sanauallah, K. (2014). Experimental investigations of the interface between steam and water two phase flows. *International Journal of Heat and Mass Transfer*.
<https://doi.org/10.1016/j.ijheatmasstransfer.2014.02.035>
- Kieffer, S. W., & Sturtevant, B. (1984). Laboratory studies of volcanic jets. *Journal of Geophysical Research*. <https://doi.org/10.1029/JB089iB10p08253>
- Kokelaar, B. P., & Durant, G. P. (1983). The submarine eruption and erosion of Surtla (Surtsey), Iceland. *Journal of Volcanology and Geothermal Research*, 19(3–4), 239–246. [https://doi.org/10.1016/0377-0273\(83\)90112-9](https://doi.org/10.1016/0377-0273(83)90112-9)
- Koyaguchi, T., & Woods, A. W. (1996). On the formation of eruption columns following explosive mixing of magma and surface-water. *Journal of Geophysical Research: Solid Earth*, 101(B3), 5561–5574. <https://doi.org/10.1029/95jb01687>
- Kueppers, U., Nichols, A. R. L., Zanon, V., Potuzak, M., & Pacheco, J. M. R. (2012). Lava balloons-peculiar products of basaltic submarine eruptions. *Bulletin of Volcanology*, 74(6), 1379–1393. <https://doi.org/10.1007/s00445-012-0597-x>
- List, E. J. (1982). TURBULENT JETS AND PLUMES. *Annual Review of Fluid Mechanics*. <https://doi.org/10.1146/annurev.fl.14.010182.001201>
- Liu, Y., Zhang, Y., & Behrens, H. (2005). Solubility of H₂O in rhyolitic melts at low pressures and a new empirical model for mixed H₂O-CO₂ solubility in rhyolitic melts. *Journal of Volcanology and Geothermal Research*, 143(1–3), 219–235.
<https://doi.org/10.1016/j.jvolgeores.2004.09.019>
- Lube, G., Huppert, H. E., Sparks, R. S. J., & Hallworth, M. A. (2004). Axisymmetric collapses of granular columns. *Journal of Fluid Mechanics*, 508, 175–199.
<https://doi.org/10.1017/S0022112004009036>
- Luettich, R. A., Westerink, J. J., & Scheffner, N. W. (1992). ADCIRC: An Advanced Three-Dimensional Circulation Model for Shelves Coasts and Estuaries, Report 1: Theory and Methodology of ADCIRC-2DDI and ADCIRC-3DL, Dredging Research Program Technical Report DRP-92-6. In *Dredging Research Program Technical Report DRP-92-6, U.S. Army Engineers Waterways Experiment Station, Vicksburg, MS*.

- Lun, C. K. K., Savage, S. B., Jeffrey, D. J., & Chepurny, N. (1984). Kinetic theories for granular flow: Inelastic particles in Couette flow and slightly inelastic particles in a general flowfield. *Journal of Fluid Mechanics*.
<https://doi.org/10.1017/S0022112084000586>
- Lyons, J. J., Haney, M. M., Fee, D., Wech, A. G., & Waythomas, C. F. (2019). Infrasound from giant bubbles during explosive submarine eruptions. *Nature Geoscience*, *12*(11), 952–958. <https://doi.org/10.1038/s41561-019-0461-0>
- Manga, M., Fauria, K. E., Lin, C., Mitchell, S. J., Jones, M., Conway, C. E., Degruyter, W., Hosseini, B., Carey, R., Cahalan, R., Houghton, B. F., White, J. D. L., Jutzeler, M., Soule, S. A., & Tani, K. (2018). The pumice raft-forming 2012 Havre submarine eruption was effusive. *Earth and Planetary Science Letters*.
<https://doi.org/10.1016/j.epsl.2018.02.025>
- Manga, M., Mitchell, S. J., Degruyter, W., & Carey, R. J. (2018). Transition of eruptive style: Pumice raft to dome-forming eruption at the Havre submarine volcano, southwest Pacific Ocean. *Geology*, *46*(12), 1075–1078.
<https://doi.org/10.1130/G45436.1>
- Mangan, M., Mastin, L., & Sisson, T. (2004). Gas evolution in eruptive conduits: Combining insights from high temperature and pressure decompression experiments with steady-state flow modeling. *Journal of Volcanology and Geothermal Research*.
[https://doi.org/10.1016/S0377-0273\(03\)00230-0](https://doi.org/10.1016/S0377-0273(03)00230-0)
- Manville, V., White, J. D. L., Houghton, B. F., & Wilson, C. J. N. (1998). The saturation behaviour of pumice and some sedimentological implications. *Sedimentary Geology*.
[https://doi.org/10.1016/S0037-0738\(98\)00057-8](https://doi.org/10.1016/S0037-0738(98)00057-8)
- Martí, J., Pinel, V., López, C., Geyer, A., Abella, R., Tárraga, M., Blanco, M. J., Castro, A., & Rodríguez, C. (2013). Causes and mechanisms of the 2011-2012 El Hierro (Canary Islands) submarine eruption. *Journal of Geophysical Research: Solid Earth*, *118*(3), 823–839. <https://doi.org/10.1002/jgrb.50087>
- Martin, J. E., & Meiburg, E. (1994). The accumulation and dispersion of heavy particles in forced two-dimensional mixing layers. I. The fundamental and subharmonic cases. *Physics of Fluids*, *6*(3), 1116–1132. <https://doi.org/10.1063/1.868283>
- Mastin, L. G., & Witter, J. B. (2000). The hazards of eruptions through lakes and seawater. *Journal of Volcanology and Geothermal Research*, *97*(1–4), 195–214.
[https://doi.org/10.1016/S0377-0273\(99\)00174-2](https://doi.org/10.1016/S0377-0273(99)00174-2)
- Mastin, L. G. (1995). Explosive summit eruptions at Kilauea: Do they occur when the caldera floor drops below the water table? *Eos, Transactions, American Geophysical Union Supp.*

- Mastin, Larry G. (2002). Insights into volcanic conduit flow from an open-source numerical model. *Geochemistry, Geophysics, Geosystems*.
<https://doi.org/10.1029/2001gc000192>
- Mazed, D., Lo Frano, R., Aquaro, D., Del Serra, D., Sekachev, I., & Olcese, M. (2018). Experimental investigation of steam condensation in water tank at sub-atmospheric pressure. *Nuclear Engineering and Design*, 335(May), 241–254.
<https://doi.org/10.1016/j.nucengdes.2018.05.025>
- McBirney, A. R. (1963). Factors governing the nature of submarine volcanism. *Bulletin Volcanologique*. <https://doi.org/10.1007/BF02597304>
- McPhie, J., Walker, G. P. L., & Christiansen, R. L. (1990). Phreatomagmatic and phreatic fall and surge deposits from explosions at Kilauea volcano, Hawaii, 1790 a.d.: Keanakakoi Ash Member. *Bulletin of Volcanology*.
<https://doi.org/10.1007/BF00302047>
- Mélançon, J., Levasseur, M., Lizotte, M., Delmelle, P., Cullen, J., Hamme, R. C., Peña, A., Simpson, K. G., Scarratt, M., Tremblay, J. É., Zhou, J., Johnson, K., Sutherland, N., Arychuk, M., Nemcek, N., & Robert, M. (2014). Early response of the northeast subarctic Pacific plankton assemblage to volcanic ash fertilization. *Limnology and Oceanography*. <https://doi.org/10.4319/lo.2014.59.1.0055>
- Meng, Z., Zhang, W., Liu, J., Yan, R., & Shen, G. (2019). Experimental study on the condensation of sonic steam in the underwater environment. *Nuclear Engineering and Technology*, 51(4), 987–995. <https://doi.org/10.1016/j.net.2019.02.003>
- Mitchell, S. J., Houghton, B. F., Carey, R. J., Manga, M., Fauria, K. E., Jones, M. R., Soule, S. A., Conway, C. E., Wei, Z., & Giachetti, T. (2019). Submarine giant pumice: a window into the shallow conduit dynamics of a recent silicic eruption. *Bulletin of Volcanology*, 81(7). <https://doi.org/10.1007/s00445-019-1298-5>
- Mitchell, S. J., McIntosh, I. M., Houghton, B. F., Carey, R. J., & Shea, T. (2018). Dynamics of a powerful deep submarine eruption recorded in H₂O contents and speciation in rhyolitic glass: The 2012 Havre eruption. *Earth and Planetary Science Letters*, 494, 135–147. <https://doi.org/10.1016/j.epsl.2018.04.053>
- Moitra, P., Sonder, I., & Valentine, G. A. (2020). The role of external water on rapid cooling and fragmentation of magma. *Earth and Planetary Science Letters*, 537. <https://doi.org/10.1016/j.epsl.2020.116194>
- Murch, A. P., White, J. D. L., & Carey, R. J. (2019). Unusual fluidal behavior of a silicic magma during fragmentation in a deep subaqueous eruption, Havre volcano, southwestern Pacific Ocean. *Geology*, 47(5), 487–490.
<https://doi.org/10.1130/G45657.1>

- Murch, Arran P., White, J. D. L., & Carey, R. J. (2019). Characteristics and deposit stratigraphy of submarine-erupted silicic ash, havre volcano, kermadec arc, New Zealand. *Frontiers in Earth Science*, 7. <https://doi.org/10.3389/feart.2019.00001>
- Namiki, A., & Manga, M. (2008). Transition between fragmentation and permeable outgassing of low viscosity magmas. *Journal of Volcanology and Geothermal Research*. <https://doi.org/10.1016/j.jvolgeores.2007.07.020>
- Nayar, K. G., Sharqawy, M. H., Banchik, L. D., & Lienhard, J. H. (2016). Thermophysical properties of seawater: A review and new correlations that include pressure dependence. *Desalination*. <https://doi.org/10.1016/j.desal.2016.02.024>
- Neri, A., Esposti Ongaro, T., Macedonio, G., & Gidaspow, D. (2003). Multiparticle simulation of collapsing volcanic columns and pyroclastic flow. *Journal of Geophysical Research: Solid Earth*, 108(B4). <https://doi.org/10.1029/2001jb000508>
- Osborne, N. S., & Meyers, C. H. (1934). A formula and tables for the pressure of saturated water vapor in the range 0 to 374 C. *Journal of Research of the National Bureau of Standards*, 13(1), 1. <https://doi.org/10.6028/jres.013.003>
- Papale, P. (1999). Strain-induced magma fragmentation in explosive eruptions. *Nature*. <https://doi.org/10.1038/17109>
- Papale, P. (2001). Dynamics of magma flow in volcanic conduits with variable fragmentation efficiency and nonequilibrium pumice degassing. *Journal of Geophysical Research: Solid Earth*. <https://doi.org/10.1029/2000jb900428>
- Pérez-Torrado, F. J., Paris, R., Cabrera, M. C., Schneider, J. L., Wassmer, P., Carracedo, J. C., Rodríguez-Santana, Á., & Santana, F. (2006). Tsunami deposits related to flank collapse in oceanic volcanoes: The Agaete Valley evidence, Gran Canaria, Canary Islands. *Marine Geology*, 227(1–2), 135–149. <https://doi.org/10.1016/j.margeo.2005.11.008>
- Pham, A. L. D., & Ito, T. (2018). Formation and Maintenance of the GEOTRACES Subsurface-Dissolved Iron Maxima in an Ocean Biogeochemistry Model. *Global Biogeochemical Cycles*. <https://doi.org/10.1029/2017GB005852>
- Pontbriand, C. W., Soule, S. A., Sohn, R. A., Humphris, S. E., Kunz, C., Singh, H., Nakamura, K. I., Jakobsson, M., & Shank, T. (2012). Effusive and explosive volcanism on the ultraslow-spreading Gakkel Ridge, 85°E. *Geochemistry, Geophysics, Geosystems*, 13(10), 1–22. <https://doi.org/10.1029/2012GC004187>

- Resing, J. A., Rubin, K. H., Embley, R. W., Lupton, J. E., Baker, E. T., Dziak, R. P., Baumberger, T., Lilley, M. D., Huber, J. A., Shank, T. M., Butterfield, D. A., Clague, D. A., Keller, N. S., Merle, S. G., Buck, N. J., Michael, P. J., Soule, A., Caress, D. W., Walker, S. L., ... Thomas, H. (2011). Active submarine eruption of boninite in the northeastern Lau Basin. *Nature Geoscience*, 4(11), 799–806. <https://doi.org/10.1038/ngeo1275>
- Rotella, M. D., Wilson, C. J. N., Barker, S. J., Ian Schipper, C., Wright, I. C., & Wysoczanski, R. J. (2015). Dynamics of deep submarine silicic explosive eruptions in the Kermadec arc, as reflected in pumice vesicularity textures. *Journal of Volcanology and Geothermal Research*, 301, 314–332. <https://doi.org/10.1016/j.jvolgeores.2015.05.021>
- Rudnicki, M. D., & Elderfield, H. (1992). Theory applied to the Mid-Atlantic ridge hydrothermal plumes: the finite-difference approach. *Journal of Volcanology and Geothermal Research*, 50(1–2), 161–172. [https://doi.org/10.1016/0377-0273\(92\)90043-D](https://doi.org/10.1016/0377-0273(92)90043-D)
- Santana-Casiano, J. M., González-Dávila, M., Fraile-Nuez, E., De Armas, D., González, A. G., Domínguez-Yanes, J. F., & Escáñez, J. (2013). The natural ocean acidification and fertilization event caused by the submarine eruption of El Hierro. *Scientific Reports*. <https://doi.org/10.1038/srep01140>
- Savage, S. B. (1998). Analyses of slow high-concentration flows of granular materials. *Journal of Fluid Mechanics*. <https://doi.org/10.1017/S0022112098002936>
- Scase, M. M. (2009). Evolution of volcanic eruption columns. *Journal of Geophysical Research: Earth Surface*, 114(4). <https://doi.org/10.1029/2009JF001300>
- Schipper, C. I., Sonder, I., Schmid, A., White, J. D. L., Dürig, T., Zimanowski, B., & Büttner, R. (2013). Vapour dynamics during magma-water interaction experiments: Hydromagmatic origins of submarine volcanoclastic particles (limu o Pele). *Geophysical Journal International*, 192(3), 1109–1115. <https://doi.org/10.1093/gji/ggs099>
- Schipper, C. I., White, J. D. L., Houghton, B. F., Shimizu, N., & Stewart, R. B. (2010). “Poseidic” explosive eruptions at Loihi Seamount, Hawaii. *Geology*, 38(4), 291–294. <https://doi.org/10.1130/G30351.1>
- Schmidt, R., & Schminche, H.-U. (2000). Seamounts and island building. In *Encyclopedia of Volcanoes*.
- Sharqawy, M. H., Lienhard V, J. H., & Zubair, S. M. (2010). Thermophysical properties of seawater: A review of existing correlations and data. *Desalination and Water Treatment*. <https://doi.org/10.5004/dwt.2010.1079>

- Silver, E., Day, S., Ward, S., Hoffmann, G., Llanes, P., Driscoll, N., Appelgate, B., & Saunders, S. (2009). Volcano collapse and tsunami generation in the Bismarck Volcanic Arc, Papua New Guinea. *Journal of Volcanology and Geothermal Research*, 186(3–4), 210–222. <https://doi.org/10.1016/j.jvolgeores.2009.06.013>
- Sonder, I., Schmid, A., Seegelken, R., Zimanowski, B., & Büttner, R. (2011). Heat source or heat sink: What dominates behavior of non-explosive magma-water interaction? *Journal of Geophysical Research: Solid Earth*, 116(9), 1–8. <https://doi.org/10.1029/2011JB008280>
- Sparks, R. S.J. (1986). The dimensions and dynamics of volcanic eruption columns. *Bulletin of Volcanology*, 48(1), 3–15. <https://doi.org/10.1007/BF01073509>
- Sparks, R. Stephen J., Bonnetcaze, R. T., Huppert, H. E., Lister, J. R., Hallworth, M. A., Mader, H., & Phillips, J. (1993). Sediment-laden gravity currents with reversing buoyancy. *Earth and Planetary Science Letters*. [https://doi.org/10.1016/0012-821X\(93\)90028-8](https://doi.org/10.1016/0012-821X(93)90028-8)
- Steam tables. (1934). In *Nature*. <https://doi.org/10.1038/134491a0>
- Stewart, A. L., & McPhie, J. (2004). An Upper Pliocene coarse pumice breccia generated by a shallow submarine explosive eruption, Milos, Greece. *Bulletin of Volcanology*, 66(1), 15–28. <https://doi.org/10.1007/s00445-003-0292-z>
- Suzuki, Y. J., & Koyaguchi, T. (2010). Numerical determination of the efficiency of entrainment in volcanic eruption columns. *Geophysical Research Letters*, 37(5). <https://doi.org/10.1029/2009GL042159>
- Syamlal, M., Rogers, W., & O'Brien, T. J. (1993). *MFIX documentation theory guide*. <https://doi.org/10.2172/10145548>
- Thorarinsson, S. (1965). The Surtsey Eruption: Course of events and the development of the new island. *Surtsey Research Progress Report, I*, 51–55.
- Thorarinsson, S. (1968). The Surtsey Eruption - Course of events during the year 1967. *Surtsey Research Progress Report, IV*, 143–149.
- Troise, M., Cerminara, M., Esposti Ongaro, T., & Giordano, G. (2019). The footprint of column collapse regimes on pyroclastic flow temperatures and plume heights. *Nature Communications*, 10(1). <https://doi.org/10.1038/s41467-019-10337-3>
- Turner, J. S. (1966). Jets and plumes with negative or reversing buoyancy. *Journal of Fluid Mechanics*. <https://doi.org/10.1017/S0022112066001526>
- VALENTINE, G. (1998). Chapter 4 Eruption column physics. *Developments in Volcanology*, 4, 91–138. [https://doi.org/10.1016/s1871-644x\(01\)80005-x](https://doi.org/10.1016/s1871-644x(01)80005-x)

- Valentine, G. A., & Wohletz, K. H. (1989). Numerical models of Plinian eruption columns and pyroclastic flows. *Journal of Geophysical Research*, 94(B2), 1867–1887. <https://doi.org/10.1029/JB094iB02p01867>
- Valentine, Greg A. (1998). Chapter 4 Eruption column physics. *Developments in Volcanology*. [https://doi.org/10.1016/s1871-644x\(01\)80005-x](https://doi.org/10.1016/s1871-644x(01)80005-x)
- Vaughan, R. G., & Webley, P. W. (2010). Satellite observations of a surtseyan eruption: Hunga Ha’apai, Tonga. *Journal of Volcanology and Geothermal Research*, 198(1–2), 177–186. <https://doi.org/10.1016/j.jvolgeores.2010.08.017>
- Velasquez, E., Bryan, S. E., Ekins, M., Cook, A. G., Hurrey, L., & Firn, J. (2018). Age and area predict patterns of species richness in pumice rafts contingent on oceanic climatic zone encountered. *Ecology and Evolution*. <https://doi.org/10.1002/ece3.3980>
- Verolino, A., White, J. D. L., & Zimanowski, B. (2018). Particle transport in subaqueous eruptions: An experimental investigation. *Journal of Volcanology and Geothermal Research*, 349, 298–310. <https://doi.org/10.1016/j.jvolgeores.2017.11.013>
- Walker, S. L., Baker, E. T., Resing, J. A., Chadwick, W. W., Lebon, G. T., Lupton, J. E., & Merle, S. G. (2008). Eruption-fed particle plumes and volcanoclastic deposits at a submarine volcano: NW Rota-1, Mariana Arc. *Journal of Geophysical Research: Solid Earth*. <https://doi.org/10.1029/2007JB005441>
- Wallace, P. J., Plank, T., Edmonds, M., & Hauri, E. H. (2015). Chapter 7 – Volatiles in Magmas. In *The Encyclopedia of Volcanoes*. <https://doi.org/10.1016/B978-0-12-385938-9.00007-9>
- White, J. D. L. (2000). Subaqueous eruption-fed density currents and their deposits. *Precambrian Research*, 101(2–4), 87–109. [https://doi.org/10.1016/S0301-9268\(99\)00096-0](https://doi.org/10.1016/S0301-9268(99)00096-0)
- White, J. D. L., McPhie, J., & Soule, S. A. (2015). Submarine Lavas and Hyaloclastite. In *The Encyclopedia of Volcanoes*. <https://doi.org/10.1016/b978-0-12-385938-9.00019-5>
- White, J. D. L., Schipper, C. I., & Kano, K. (2015). Submarine Explosive Eruptions. In *The Encyclopedia of Volcanoes* (Second Edi). Elsevier Inc. <https://doi.org/10.1016/b978-0-12-385938-9.00031-6>
- White, J. D. L., Smellie, J. L., & Clague, D. A. (2003). Introduction: A deductive outline and topical overview of subaqueous explosive volcanism. In *Geophysical Monograph Series*. <https://doi.org/10.1029/140GM01>

- Whitham, A. G., & Sparks, R. S. J. (1986). Pumice. *Bulletin of Volcanology*, 48(4), 209–223. <https://doi.org/10.1007/BF01087675>
- Wilson, L and Walker, G. P. . (1987). Plinian Eruptions : the Control of Eruption Conditions and. *Geophysical Journal International*, 89(2), 657–679.
- Wilson, L. (1976). Explosive Volcanic Eruptions—III. Plinian Eruption Columns. *Geophysical Journal of the Royal Astronomical Society*, 45(3), 543–556. <https://doi.org/10.1111/j.1365-246X.1976.tb06909.x>
- Wohletz, K. H. (2003). Water/magma interaction: Physical considerations for the deep submarine environment. *Geophysical Monograph Series*, 140, 25–49. <https://doi.org/10.1029/140GM02>
- Wohletz, K., Zimanowski, B., & Büttner, R. (2009). Magma–water interactions. In *Modeling Volcanic Processes: The Physics and Mathematics of Volcanism*. <https://doi.org/10.1017/CBO9781139021562.011>
- Woods, A. W. (1988). The fluid dynamics and thermodynamics of eruption columns. *Bulletin of Volcanology*. <https://doi.org/10.1007/BF01079681>
- Woods, A. W. (1993). Moist convection and the injection of volcanic ash into the atmosphere. *Journal of Geophysical Research*. <https://doi.org/10.1029/93jb00718>
- Woods, Andrew W. (1995). The dynamics of explosive volcanic eruptions. In *Reviews of Geophysics* (Vol. 33, Issue 4, pp. 495–530). <https://doi.org/10.1029/95RG02096>
- Xu, Q., Ye, S., Chen, Y., Chen, Q., & Guo, L. (2018). Condensation regime diagram for supersonic and subsonic steam jet condensation in water flow in a vertical pipe. *Applied Thermal Engineering*, 130, 62–73. <https://doi.org/10.1016/j.applthermaleng.2017.10.135>
- Yamamoto, T., Soya, T., Suto, S., Uto, K., Takada, A., Sakaguchi, K., & Ono, K. (1991). The 1989 submarine eruption off eastern Izu Peninsula, Japan: ejecta and eruption mechanisms. *Bulletin of Volcanology*, 53(4), 301–308. <https://doi.org/10.1007/BF00414526>
- Zhang, Y. (1999). A criterion for the fragmentation of bubbly magma based on brittle failure theory. *Nature*. <https://doi.org/10.1038/45210>
- Zhao, Q., & Hibiki, T. (2018). Review: Condensation regime maps of steam submerged jet condensation. *Progress in Nuclear Energy*, 107(November), 31–47. <https://doi.org/10.1016/j.pnucene.2017.12.014>

Zimanowski, B., & Buttner, R. (2003). Phreatomagmatic explosions in subaqueous volcanism. *Geophysical Monograph Series*, 140, 51–60.
<https://doi.org/10.1029/140GM03>